Development and calibration of NuLat, A new type of neutrino detector

Xinjian Ding

Dissertation submitted to the Faculty of the
Virginia Polytechnic Institute and State University
in partial fulfillment of the requirements for the degree of

Doctor of Philosophy
in
Physics

R.Bruce Vogelaar, Chair
Mark Pitt
Jean Joseph Heremans
Chenggang Tao

Nov 19, 2017
Blacksburg, Virginia

Development and calibration of NuLat, A new type of neutrino detector

Xinjian Ding

(ABSTRACT)

Over the past 20 years, the detection of neutrino oscillation has reported a lot of important results. The oscillation phenomenon itself has been well proved by various experiments. Some oscillation parameters has been measured and now in the area of precise determination. On the other hand, some new questions like the possibility of the existence of light sterile neutrinos and unexpected 5 MeV bump were raised during the measurement. The Neutrino Lattice Experiment (NuLat) is a detector based on the Raghavan Optical Lattice (ROL). It should be able to offer a compact design of an effective detector with good mobility. It can be extremely useful in the short baseline reactor neutrino oscillation detection community to resolve several confusing issues. In this thesis, we present the calibration results we got from the first active NuLat detector and show what kind of improvements we need for the next version of the NuLat detector based on these results.

Development and calibration of NuLat, A new type of neutrino detector

Xinjian Ding

(GENERAL AUDIENCE ABSTRACT)

During the last century, physicists have developed a nice framework to describe the physics world we live. The model which we called Standard Model has been constructed to describe the behavior of elementary particles and nicely explain the phenomenon we found from various experiments. However there are still a lot mysteries which cannot be explained by this model and more precise measurements on different fields of particle physics are need to help us improve our understanding about this. Neutrino oscillation is one of the most important field related to this kind of concern.

The Neutrino Lattice Experiment (NuLat) is a new type of neutrino detector. It has a good geometry reconstruction ability based on the the Raghavan Optical Lattice (ROL). Since we cannot directly see the elementary particles, we always rely on the signals generated by the reaction between particles and our detector. How to interpret the signals becomes crucial at this point to have high quality experimental data. NuLat is such kind of neutrino detector which offer good ability for us to interpret the signal right. It has a compact design compared to most of other detectors in this field. This is really useful because it can be implemented with limited space where other detectors might have difficulties. Simultaneously the ROL design can help offer nice background rejection ability and high energy resolution.

In this thesis, we discuss the progress about develop and assembly of the first active NuLat detector with the preliminary calibration data which give us basic understanding about the performance of this first version.

Acknowledgements

It has been a long journal towards the finish of my PHD degree. There are so many people help me during the past seven years and I do owe a tremendous debt of gratitude to all of them.

First and foremost I would like to thank my advisor, Bruce Vogelaar. We had an unexpected talk about research after I proctored an exam with you. This talk finally made me became a member of your nice group. In the past 7 years, all the discussion between us helped me to grow up not just as a researcher, but as a matural man. Your huge support and tolerance of all the mistakes I made during this period means a lot to me.

I also want to thank Mark Makela and Albert Young for all the guidence when I worked with UCN group. Thanks to the hugh effort did by Mark Makela and Russell Mammei, a good foundation for the coating working development was already there when I was involved into this project. It was also a lot of fun to work with Brittney VornDick and David Bravo. I cherished all the interesting talks we had when we worked on the guide coating. Also I want to thank Matt Hil, Marc Pomeroy, Chris Wollbrink for all the help you guys offered when we dealt with the guide coating. Some of the works were exhausting but you guys finished that perfectly.

I joined the group of NuLat a little bit later. I do appreciate a lot to the work already done by Derek, Zach and Tristan. Thanks to all the work you have done, this version of the NuLat detector can become real. Also I owe a tremendous thank you to Tristan and Ryan for being there all the time when I needed help or just needed to find a person to talk with.

I also want to thank Jesse Barber, Matt Lynch and William Clark for all the help you guys offered during the past year. You guys helped to handle a lot issues to make this version of the NuLat detector real. It would have been impossible without all that help. It is really a good experience and memory to work with you guys.

I would also like to thank the machine shop, Scott, Ron, and John. You guys are so helpful when I have problems or some stuff need to be made within a short time scale.

I also want to thank Chris for taking care of me when I just arrived here. I will never forget the touching talk you and I have the first day I came to the department. You made me calm down and feel warm as a foreigner just coming to a strange place.

There are a great number of people offer their help to make this dissertation happen. I cannot list them all here, but I owe them all a great debt of gratitude.

Finally I would thank my family for being really supportive of my decision to leave home for such a long period and do whatever I want.

Contents

List of Figures

List of Tables

Chapter 1

Introduction

Neutrino oscillation is one of the most important phenomena to verify the correctness of the Standard Model of particle physics. A lot of experiments have measured this phenomenon with different neutrino sources like solar neutrinos, atmospheric neutrinos, neutrinos from accelerators and reactors. The results from these experiments have shown some hints about the physics beyond Standard Model.

This dissertation is mainly about the research and development (R&D) for the Neutrino Lattice experiment (NuLat). The detector uses a Raghavan Optical Lattice (ROL) which provides a unique means to detect neutrino and reject the background using inherent segmentation of scintillator cubes to recreate the neutrino event geometry. The advantage of this detector is its compact size compared to other neutrino detectors. The inherent geometry reconstruction ability helps it to reach a good signal to background ratio. Also it should have better mobility compared to other experiments. This mobility can help it to detect short baseline reactor neutrinos from different baselines which is extremely useful to reduce errors like spectral uncertainty and also verify the neutrino oscillation with a short baseline. The work present in this thesis is mainly about the assembly and testing of the first active NuLat detector. We briefly review the background of neutrino oscillation and the physics idea behind the NuLat detector in chapter 2 and 3. The actual R&D work towards this first active NuLat detector are introduced in chapter 4-6. In chapter 7 and 8, we summarize all the results we got from the different calibration tests and discuss the improvement we need for the next version of the NuLat detector. The brief introduction of content in each chapter is as follows:

- Chapter 2 introduces the basic idea of neutrino physics. Various neutrino experiments and a short history about these experiments are summarized. Then we introduce the initial motivation for the NuLat detector and the potential it has to help the neutrino community to understand the result of reactor neutrino oscillation experiments.

- Chapter 3 introduces the physics idea behind NuLat experiment. It has two different sections. The first mainly focuses on the design of the NuLat detector itself. It contains an introduction to the specific structure of a Raghavan Optical Lattice (ROL) based detector and also a brief introduction about related design of the current NuLat detector. The simulation work to estimate the sensitivity of NuLat to the active to sterile neutrino oscillation parameters is also introduced in this section. The second section discusses the data acquisition electronic system inherited from the mTC detector. It introduces the function of this kind of electronics and how it help us with data acquisition.

- Chapter 4 presents details about how the current version of the NuLat detector is assembled. It introduces how spacers maintain air gaps between cubes, and then shows how we put all the cubes together and seal them into an acrylic box. Another topic is the alignment and assembly of PMTs into the detector with a quality control system.

- Chapter 5 introduces some preliminary hardware tests we did and some modifications during the experience of running the whole system. There are two sections in this chapter. The first focuses on the test we did to understand the light transmission property of Li loaded and unloaded cubes. The cross talk of signals with different configurations was also tested. This is followed by a section about the electronics. Since the data acquisition system was not designed for the NuLat project, we did several tests and some modifications to make it more suitable for our purpose.

- Chapter 6 introduces how we use radon as source to do calibration on the NuLat detector. It introduces the system used to fill radon into the detector and how we checked the existence of it in the detector. Then we present results from different calibration processes to show how radon can help us calibrate.

- Chapter 7 summarizes all the calibration results related to the light yield of scintillator and light loss through scintillator. These discussions reveal what improvements we should search for the next version of the NuLat detector

- Chapter 8 is the conclusion chapter. It summarizes all the information we obtained from the current calibration process. In addition, it discusses what kind of work might help the next version of the NuLat detector.

Chapter 2

Neutrino Oscillation

In this chapter, we first introduce the theory of neutrino oscillation and what kind of parameters should be controlled or measured by related experiments. It also shows how neutrino oscillations can help give hints about possible extension of the current Standard Model for particle physics. After the theory part, we introduce various neutrino experiments and some results they reported in the past 20 years until now. It includes important results obtained and shows how the NuLat detector can help in this field with its unique properties.

2.1 Neutrino oscillation

Neutrinos are elementary particles produced in the weak interaction. Currently three different flavour eigenstates of neutrinos exist in the Standard Model. The neutrino that is generated with the charged electron is named as the electron neutrino, and so on.

However it is possible that the flavour eigenstates are not identical to the mass eigenstates (states which have definite mass) as with the quarks and the CKM matrix. This implies that when a definite flavour eigenstate is generated at a source, this state actually is a linear combination of states of definite mass. During the travel of this particle with definite flavour eigenstate, the phase of the mass eigenstates will change. When we try to detect it, the mass states will have different relative phases to the original states at the source. So it is possible that we may detect a flavour state which was not present in the beam to begin with. If this phenomenon shows up during the detection of neutrinos, we call it neutrino oscillation. In the current Standard Model, neutrinos are not allowed

to acquire mass through the Higgs mechanism because they exist only in the left-handed state (right-handed for antineutrino). So the phenomenon of neutrino oscillation itself is evidence requiring some extension of the current Standard Model because it implies that neutrino must be a massive particle.

To derive a mathematical expression of neutrino oscillation, we start with a two-flavour neutrino oscillations model. We first define two flavour states as ν_α and ν_β with two mass states as ν_1 and ν_2. Then we can write the mixing between flavour and mass states with a 2×2 matrix as:

$$\begin{pmatrix} \nu_\alpha \\ \nu_\beta \end{pmatrix} = \begin{pmatrix} cos\theta & sin\theta \\ -sin\theta & cos\theta \end{pmatrix} \begin{pmatrix} \nu_1 \\ \nu_2 \end{pmatrix} , \tag{2.1}$$

where θ is unspecified parameter known as the mixing angle. We can then write the mass states as:

$$\begin{pmatrix} \nu_1 \\ \nu_2 \end{pmatrix} = \begin{pmatrix} cos\theta & -sin\theta \\ sin\theta & cos\theta \end{pmatrix} \begin{pmatrix} \nu_\alpha \\ \nu_\beta \end{pmatrix} . \tag{2.2}$$

If we apply the time-dependent Schrdinger equation with no potentials to the mass states, we should get the equation like this:

$$i\frac{\partial}{\partial t} |\nu_i(x,t)\rangle = E |\nu_i(x,t)\rangle = -\frac{1}{2m_i}\frac{\partial^2}{\partial x^2} |\nu_i(x,t)\rangle \quad i = 1, 2 . \tag{2.3}$$

The solution to this equation is a plane-wave:

$$|\nu_i(x,t)\rangle = e^{-i(E_i t - p_i x)} |\nu_i(0,0)\rangle = e^{-i\phi_i} |\nu_i(0,0)\rangle , \tag{2.4}$$

where phase $\phi_i = E_i t - p_i x$, $p_i = (t, \mathbf{p})$ is the 4-momentum of the neutrino mass state $|\nu_i\rangle$ and $x_i = (t, \mathbf{x})$ is the 4-space vector.

So when we apply this to expression (2.2) with combination of (2.1), we should get:

$$\begin{aligned} \begin{pmatrix} |\nu_1(x,t)\rangle \\ |\nu_2(x,t)\rangle \end{pmatrix} &= \begin{pmatrix} e^{-i\phi_1} & 0 \\ 0 & e^{-i\phi_2} \end{pmatrix} \begin{pmatrix} |\nu_1(0,0)\rangle \\ |\nu_2(0,0)\rangle \end{pmatrix} \\ &= \begin{pmatrix} e^{-i\phi_1} & 0 \\ 0 & e^{-i\phi_2} \end{pmatrix} \begin{pmatrix} cos\theta & -sin\theta \\ sin\theta & cos\theta \end{pmatrix} \begin{pmatrix} |\nu_\alpha(0,0)\rangle \\ |\nu_\beta(0,0)\rangle \end{pmatrix} . \end{aligned} \tag{2.5}$$

Detection of the neutrino oscillation just means that we have a different mixed state at (x, t), based on equation (2.1), we can write the mixed state at (x, t) as:

$$\begin{pmatrix} |\nu_\alpha(x,t)\rangle \\ |\nu_\beta(x,t)\rangle \end{pmatrix} = \begin{pmatrix} cos\theta & sin\theta \\ -sin\theta & cos\theta \end{pmatrix} \begin{pmatrix} |\nu_1(x,t)\rangle \\ |\nu_2(x,t)\rangle \end{pmatrix} , \tag{2.6}$$

plugging this into equation (2.5), we can get

$$\begin{aligned} \begin{pmatrix} |\nu_\alpha(x,t)\rangle \\ |\nu_\beta(x,t)\rangle \end{pmatrix} &= \begin{pmatrix} e^{-i\phi_1} & 0 \\ 0 & e^{-i\phi_2} \end{pmatrix} \begin{pmatrix} |\nu_1(0,0)\rangle \\ |\nu_2(0,0)\rangle \end{pmatrix} \\ &= \begin{pmatrix} cos\theta & sin\theta \\ -sin\theta & cos\theta \end{pmatrix} \begin{pmatrix} e^{-i\phi_1} & 0 \\ 0 & e^{-i\phi_2} \end{pmatrix} \begin{pmatrix} cos\theta & -sin\theta \\ sin\theta & cos\theta \end{pmatrix} \begin{pmatrix} |\nu_\alpha(0,0)\rangle \\ |\nu_\beta(0,0)\rangle \end{pmatrix} . \end{aligned} \tag{2.7}$$

This equation can be rewritten to a more compact version as

$$U = \begin{pmatrix} cos^2\theta e^{-i\phi_1} + sin^2\theta e^{-i\phi_2} & -cos\theta sin\theta e^{-i\phi_1} + sin\theta cos\theta e^{-i\phi_2} \\ -cos\theta sin\theta e^{-i\phi_1} + sin\theta cos\theta e^{-i\phi_2} & sin^2\theta e^{-i\phi_1} + cos^2\theta e^{-i\phi_2} \end{pmatrix} , \tag{2.8}$$

$$\begin{pmatrix} |\nu_\alpha(x,t)\rangle \\ |\nu_\beta(x,t)\rangle \end{pmatrix} = U \begin{pmatrix} |\nu_\alpha(0,0)\rangle \\ |\nu_\beta(0,0)\rangle \end{pmatrix} . \tag{2.9}$$

Here, we define U as the mixing matrix. With equation (2.9), we can get the probability for finding a $|\nu_\beta\rangle$ state in the beam at the detector given that we generated a $|\nu_\alpha\rangle$ neutrino at the source. The amplitude can be calculated as:

$$\begin{aligned} \langle\nu_\beta(x,t)|\nu_\alpha(0,0)\rangle &= (cos\theta sin\theta(e^{i\phi_2} - e^{i\phi_1})) \langle\nu_\alpha(0,0)|\nu_\alpha(0,0)\rangle \\ &+ (sin^2\theta e^{-i\phi_1} + cos^2\theta e^{-i\phi_2}) \langle\nu_\beta(0,0)|\nu_\alpha(0,0)\rangle , \end{aligned} \tag{2.10}$$

since the beam is pure $|\nu_\alpha\rangle$ at source, so $\langle\nu_\alpha(0,0)|\nu_\alpha(0,0)\rangle = 1$ and $\langle\nu_\beta(0,0)|\nu_\alpha(0,0)\rangle = 0$. Equation (2.10) becomes

$$\langle\nu_\beta(x,t)|\nu_\alpha(0,0)\rangle = cos\theta sin\theta(e^{i\phi_2} - e^{i\phi_1}) , \tag{2.11}$$

and the probability of finding $|\nu_\beta\rangle$ in the detection area should be:

$$P(\nu_\alpha \rightarrow \nu_\beta) = |\langle \nu_\beta(x,t)|\nu_\alpha(0,0)\rangle|^2$$
$$= cos^2\theta sin^2\theta|(e^{i\phi_2} - e^{i\phi_1})|^2 \ , \tag{2.12}$$

we can expand exponential term of equation (2.12) as

$$|(e^{i\phi_2} - e^{i\phi_1})|^2 = (e^{i\phi_2} - e^{i\phi_1})(e^{-i\phi_2} - e^{-i\phi_1})$$
$$= 2 - (e^{i(\phi_2-\phi_1)} + e^{-i(\phi_2-\phi_1)}) \tag{2.13}$$
$$= 2(1 - cos(\phi_2 - \phi_1)) \ ,$$

with the trigonometric identities $cos\theta sin\theta = \frac{1}{2}sin(2\theta)$ and $2sin^2(\theta) = 1 - cos(2\theta)$, we can rewrite the probability as:

$$P(\nu_\alpha \rightarrow \nu_\beta) = sin^2(2\theta)sin^2(\frac{\phi_2 - \phi_1}{2}) \ . \tag{2.14}$$

Recall that in the Schrdinger equation, the expression for ϕ_i is

$$\phi_i = E_i t - p_i x \ . \tag{2.15}$$

So the phase difference is, then,

$$\phi_2 - \phi_1 = (E_2 - E_1)t - (p_2 - p_1)x \ . \tag{2.16}$$

If we assume that the neutrinos are relativistic, let $c = \hbar = 1$, then t=x=L (where L is the conventional measure of the distance between source and detector) and

$$\phi_i = \sqrt{E_i^2 - m_i^2} \approx E_i(1 - \frac{m_i^2}{E_i^2}) \ , \tag{2.17}$$

then, the phase difference becomes

$$\phi_2 - \phi_1 = (\frac{m_1^2}{2E_1} - \frac{m_2^2}{2E_2})L \ . \tag{2.18}$$

We assume here that the mass eigenstates are created with the same energy. This approximate assumption is not necessary, but it can help us get the right expression easily. Actually if we deal with the mass states as wave packets instead of the plane wave we currently have, the result will be the same. So with this assumption, we would have

$$\phi_1 - \phi_2 = (\frac{m_1^2}{2E_1} - \frac{m_2^2}{2E_2})L = \frac{\Delta m^2 L}{2E} \ , \tag{2.19}$$

where $\Delta m^2 = m_1^2 - m_2^2$ and $E_1 = E_2 = E_\nu$. Substituting this phase difference expression back into the probability equation and replacing α and β with ν_e and ν_μ to make the equation as an example to express the probability of neutrino oscillation we actually can measure from electron neutrino to muon neutrino, we get

$$P(\nu_e \to \nu_\mu) = sin^2 2\theta sin^2(\frac{\Delta m^2 L}{4E_\nu}) \ . \tag{2.20}$$

If we carefully deal with the units of measurable quantities, like using kilometers for L and GeV for E, and pay attention to put $\hbar$ and c back to where left out, we would get

$$P(\nu_e \to \nu_\mu) = sin^2 2\theta sin^2(1.27\Delta m^2 [eV^2]\frac{L[km]}{E_\nu[GeV]}) \ . \tag{2.21}$$

This is the probability that one generates a ν_e but detects ν_μ and is called the oscillation probability. On the other hand, we can also get the corresponding survival probability which is the probability of generating a ν_e and detecting a ν_e :

$$P(\nu_e \to \nu_e) = 1 - sin^2 2\theta sin^2(1.27\Delta m^2 \frac{L}{E_\nu}) \ . \tag{2.22}$$

Figure 2.1 shows how the survival probability looks with a reasonable scale in an actual experiment.

We now have introduced how to compute the oscillation probability with two flavour eigenstates and mass states by a 2×2 mixing matrix. In the current Standard Model as introduced before, we have three different flavour eigenstates of neutrinos, so the mixing matrix we need to explain this neutrino oscillation phenomenon is actually a 3×3 mixing matrix called PMNS matrix and this is defined as
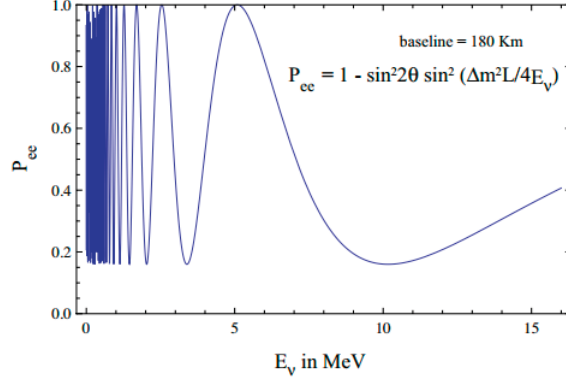
FIGURE 2.1: The ν_e survival probability as a function of the neutrino energy for L=180 km, $\Delta m^2 = 7.0 \times 10^{-5} eV^2$ and $sin^2\theta = 0.84$[1]

$$U_{PMNS} = \begin{pmatrix} c_{12}c_{13} & s_{12}c_{13} & s_{13}e^{-i\delta} \\ -s_{12}c_{23} - c_{12}s_{23}e^{i\delta} & c_{12}c_{23} - s_{12}s_{23}s_{13}e^{i\delta} & s_{23}c_{13} \\ s_{12}s_{23} - c_{12}s_{23}s_{13}e^{i\delta} & -c_{12}s_{23} - s_{12}c_{23}s_{13}e^{i\delta} & c_{23}c_{13} \end{pmatrix} . \tag{2.23}$$

The relation between flavour eigenstates and mass eigenstates is:

$$\begin{pmatrix} \nu_e \\ \nu_\mu \\ \nu_\tau \end{pmatrix} = U_{PMNS} \begin{pmatrix} \nu_1 \\ \nu_2 \\ \nu_3 \end{pmatrix} , \tag{2.24}$$

where $c_{ij} = cos\theta_{ij}$ and $s_{ij} = sin\theta_{ij}$. The angles θ_{12} θ_{13} and θ_{23} represent the mixing angles and δ is a CP violation phase. The derivation of this matrix is omitted here, details can be found in Ref[26]

As the probability equation explained before, neutrino oscillation depends also on the squared mass differences between the mass states, namely Δm_{21}^2, Δm_{32}^2 and Δm_{31}^2. Only two of these three are independent since there is a relation

$$\Delta m_{31}^2 = \Delta m_{32}^2 + \Delta m_{21}^2 . \tag{2.25}$$

Combining these, we get that neutrino oscillation depends on six free parameters: three mixing angles, two mass squared difference and one complex CP violation phase. For practical reasons, the mixing matrix is usually factorized in terms of three matrices $M_{2,3} \times M_{1,3} \times M_{1,2}$ as

$$U = \begin{pmatrix} 1 & 0 & 0 \\ 0 & c_{23} & s_{23} \\ 0 & -s_{23} & c_{23} \end{pmatrix} \begin{pmatrix} c_{13} & 0 & s_{13}e^{-i\delta} \\ 0 & 1 & 0 \\ -s_{13}e^{i\delta} & 0 & c_{13} \end{pmatrix} \begin{pmatrix} c_{12} & s_{12} & 0 \\ -s_{12} & c_{12} & 0 \\ 0 & 0 & 1 \end{pmatrix} . \qquad (2.26)$$

With this reorganization, different mixing angles are involved in different matrices. In the next section, we will introduce many neutrino oscillation experiments based on different neutrino source and E/L range. The introduction will show that certain mixing angle dominating specific flavour transition which give us ability to measure these parameters independently with a proper design.

We just briefly introduced the theory of neutrino oscillation here, but most of the important information and related parameters are already included. In the next section, we will introduce different experiments which have run for last 20 years. The introduction of these experiment should offer important background knowledge about the related technologies being used and the difficulty of detecting the oscillation phenomenon and parameters in real world.

2.2 Neutrino Oscillation Experiments

Before the introduction of various neutrino oscillation experiments, we first discuss some useful hints we got from the theory we introduced in the previous section. With the PMNS Matrix, we can get the expression of the probability of neutrino oscillation within this three-flavor framework as we did for the two-flavor model. Here we assume the CP violation term to be zero. Recall that the phase term has the form $sin^2(1.27\Delta m_{ij}^2 \frac{L}{E})$. From the solar and atmospheric neutrino oscillation experiments which will be discussed soon, we have the basic understanding that the mass splitting $\Delta m_{23}^2 \approx 3 \times 10^{-3}eV^2$ and $\Delta m_{12}^2 \approx 8 \times 10^{-5}eV^2$. So we can actually separate the expression of neutrino oscillation probability for various experiments into two cases. The first is for experiments where L/E is small enough to make

$$sin^2(1.27\Delta m_{12}^2 \frac{L}{E}) \to 0 . \qquad (2.27)$$

In this case, if we reasonably assume that $\Delta m_{23}^2 \approx \Delta m_{13}^2$ we can have the expression for the short L/E case as

$$P(\nu_\mu \to \nu_\tau) = cos^2(\theta_{13})sin^2(2\theta_{23})sin^2(1.27\Delta m_{23}^2 \frac{L}{E}) \ ,$$
$$P(\nu_e \to \nu_\mu) = sin^2(\theta_{13})sin^2(2\theta_{23})sin^2(1.27\Delta m_{23}^2 \frac{L}{E}) \ , \quad (2.28)$$
$$P(\nu_e \to \nu_\tau) = sin^2(\theta_{13})cos^2(2\theta_{23})sin^2(1.27\Delta m_{23}^2 \frac{L}{E}) \ .$$

On the other hand, when L/E is large, then the terms involving Δm_{23}^2 and Δm_{13}^2 are rapidly oscillating and the average of these two terms becomes 0.5.

$$sin^2(1.27\Delta m_{23}^2 \frac{L}{E}) \to \langle sin^2(1.27\Delta m_{23}^2 \frac{L}{E})\rangle = \tfrac{1}{2} \ ,$$
$$sin^2(1.27\Delta m_{13}^2 \frac{L}{E}) \to \langle sin^2(1.27\Delta m_{13}^2 \frac{L}{E})\rangle = \tfrac{1}{2} \ , \quad (2.29)$$

then, we can have the relation:

$$P(\nu_e \to \nu_{\mu,\tau}) = cos^2(\theta_{13})sin^2(2\theta_{12})sin^2(1.27\Delta m_{12}^2 \frac{L}{E}) + \frac{1}{2}sin^2(2\theta_{13}) \ . \quad (2.30)$$

If we go further to assume $\theta_{13} = 0$, this relation then reduces to

$$P(\nu_e \to \nu_{\mu,\tau}) = sin^2(2\theta_{12})sin^2(1.27\Delta m_{12}^2 \frac{L}{E}) \ . \quad (2.31)$$

These equations tell us what kind of oscillations we can detect with certain range of energy and baseline. Actually, these are the equations being used to design actual neutrino oscillation experiments.

We have already introduced what kind of parameters we can measure by certain limitation of L/E, then we will show a simple way to define what kind of sensitivity a specific neutrino oscillation experiment can have in a realistic condition. We still adopt a simple two flavor model at this point as an example. Suppose the flavor of neutrinos from the source is α. The detector is at distance L from the source and the flavour β of neutrino can be detected. The relation between number of signal events N_α and N_β can be expressed as

$$N_\beta = N_\alpha sin^2(2\theta)sin^2(1.27\Delta m^2 \frac{L}{E}) \ . \quad (2.32)$$

If we define the number of events we can detect at the source of flavor α neutrino to be N_α^0, then we can get

$$N_\alpha = N_\alpha^0 \frac{1}{L^2} \ . \tag{2.33}$$

We can define the sensitivity of our experiment as

$$\delta = \frac{N_\beta}{\sqrt{N_\alpha}} \ , \tag{2.34}$$

where $\sqrt{N_\alpha}$ is the standard deviation of a Poisson distribution with mean N_α. At low limit where $\Delta m^2 \frac{L}{E}$ is small, we can estimate that

$$N_\beta \approx N_\alpha sin^2(2\theta)(1.27\Delta m^2 \frac{L}{E})^2 \propto N_\alpha^0 (1.27\Delta m^2 \frac{L}{E})^2 \ , \tag{2.35}$$

so

$$\delta \propto \sqrt{N_\alpha^0}(\frac{\Delta m^2}{E})L \ . \tag{2.36}$$

For a given δ, the small Δm^2 we can see is then

$$\Delta m^2 \propto (N_\alpha^0)^{-\frac{1}{4}} \frac{E}{\sqrt{L}} \ . \tag{2.37}$$

This expression shows that the sensitivity of measurement related to Δm^2 actually depends on the number of neutrinos from the source, the energy of the neutrino from the source and the baseline between source and detector. A good understanding of L/E is crucial to get an accurate measurement of Δm^2.

On the other hand, when L/E is large, we reach a limit where we can define the value of $sin^2(1.27\Delta m^2 \frac{L}{E})$ as its average

$$sin^2(1.27\Delta m^2 \frac{L}{E}) = \langle sin^2(1.27\Delta m^2 \frac{L}{E})\rangle = \frac{1}{2} \ , \tag{2.38}$$

then we can have

$$\delta \propto \sqrt{N_\alpha^0} sin^2(2\theta)\frac{1}{L} \ . \tag{2.39}$$

This relation shows that the sensitivity of measurement of $sin^2(2\theta)$ only depends on $\sqrt{N_\alpha^0}$ for a given L, which means it just requires better statistics. So this measurement is not sensitive to the misunderstanding of energy E .
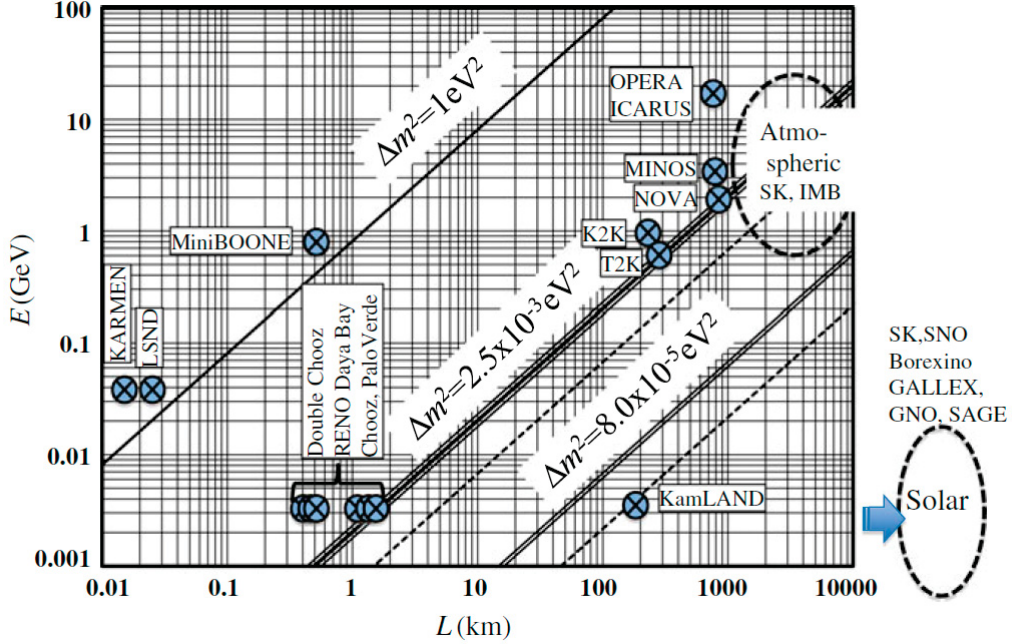
FIGURE 2.2: Relation between baselines and typical energies of various neutrino oscillation experiments. The solid lines show the first oscillation maximum and the dashed lines show the second oscillation maximum for $\Delta m^2 = 1, 8.0 \times 10^{-5}$ and $2.5 \times 10^{-3} [eV^2]$.[2]

This discussion shows what parameters we need to take care of when we design a neutrino oscillation experiment. Figure 2.2 summarizes most of the neutrino oscillation experiments with different baselines. It defines $\phi = 1.27$ and $\Delta m^2 \dfrac{L}{E_\nu} = \dfrac{\pi}{2}$ as the first oscillation maximum condition, the solid lines in figure 2.2 show this relation. Similarly, it defines $\phi = \dfrac{3\pi}{2}$ as the second oscillation maximum and this relation is marked as dashed lines in figure 2.2. In the following subsection, we introduce some of these experiments. These introductions explain the general idea of how an effective experiment is designed, and show what limitations realistically exist in the detector. We introduce these experiments by categorizing them into four subsections based on what kind of neutrino source they rely on.
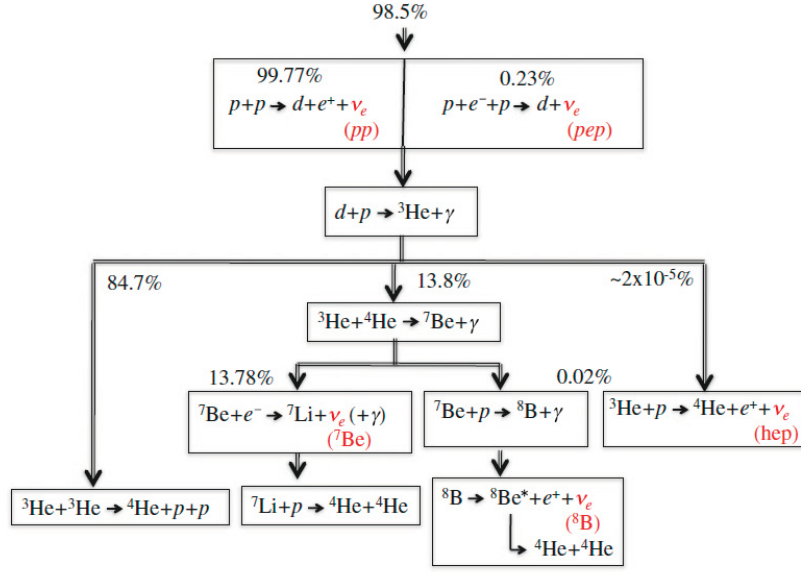
FIGURE 2.3: The proton-proton chain of the fusion process in the sun. Neutrinos are produced in the pp, pep, ^7Be, hep and ^8B processes. 1.5% of fusion takes place through the Carbon-Nitrogen- Oxygen catalytic cycle (CNO cycle), which is not shown here.[2]

2.2.0.1 Solar Neutrino Oscillation Experiments

Solar neutrinos are ν_e produced by the fusion reaction which is responsible for the solar energy production. As figure 2.3 shows, this process actually takes place through different nuclear reactions and the neutrinos produced by different reactions are characterized by different energy spectra as shown in figure 2.4.

As figures 2.3 and 2.4 show, because the final state of these reactions all contain several particles, the spectrum are all continuous. The main ν_e production process is the pp process, so the neutrino from this process is called pp neutrino with the end point energy of 0.42 MeV. The most energetic solar neutrinos can reach around 19 MeV through the hep process.

Homestake is the first experiment designed to measure the solar neutrino oscillation. It started in the 1960s. After that, many experiments tried to measure the solar neutrino oscillation including SAGE, GALLEX, GNO, SNO, SK, Borexino and KamLAND.

Homestake used the $^{37}Cl - ^{37}Ar$ method to detect ν_e, the reaction is:

$$\nu_e + {}^{37}Cl \longrightarrow {}^{37}Ar + e^- \; (threshold \quad 814 \; keV) \; . \tag{2.40}$$
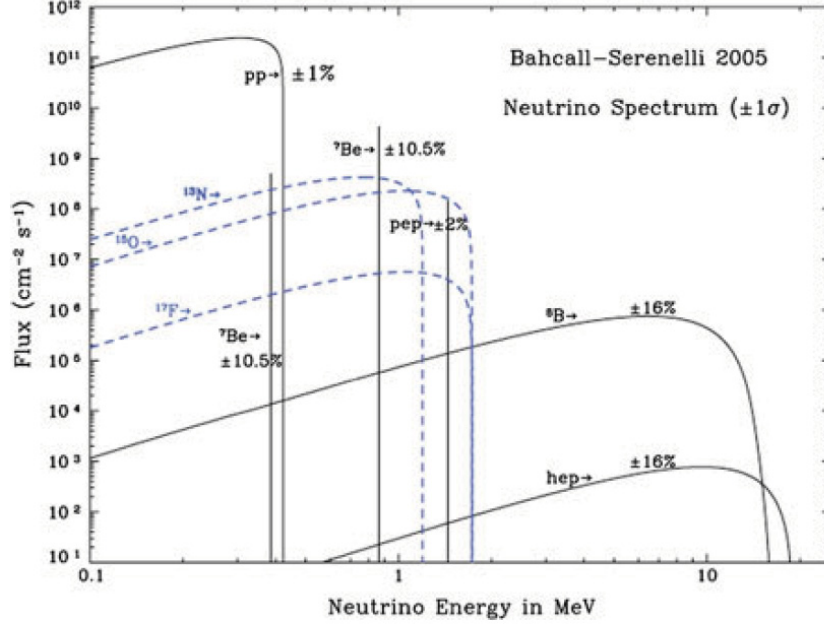
FIGURE 2.4: The solar neutrino spectrum predicted by the BS05(OP) standard solar model. The neutrino fluxes are given in units of $[/cm^2/s/MeV]$ for continuous spectra and $[/cm^2/s]$ for line spectra. The numbers associated with the neutrino sources show theoretical errors of the fluxes. This figure is taken from the late John Bahcalls web site, in a web URL http://www.sns.ias.edu/ jnb/.[3]

The ^{37}Ar atoms produced in the reaction are radioactive with a half life of 34.8 days through the following process:

$$^{37}Ar \rightarrow {}^{37}Cl + \nu_e + Auger\ electron\ . \tag{2.41}$$

The decay rate of ^{37}Ar was measured with a small low-background proportional counter. Figure 2.5 shows a summary of the observed production rate of ^{37}Ar, where the background has been subtracted. The result of Homestake indicates that only 30% of the expected value calculated from the standard solar model (SSM) is detected. This discrepancy is called the solar neutrino anomaly. Actually, over a period of 25 years running, 2,200 atoms of ^{37}Ar were detected. The low statistics make the interpretation of this experiment extremely difficult.

The major reason that Homestake has really low signal rate is that the energy threshold of a ^{37}Cl experiment is higher then the energy of the pp neutrinos. So a new kind of detector based on ^{71}Ga was designed. The reaction used to detector ν_e is similar to ^{37}Cl
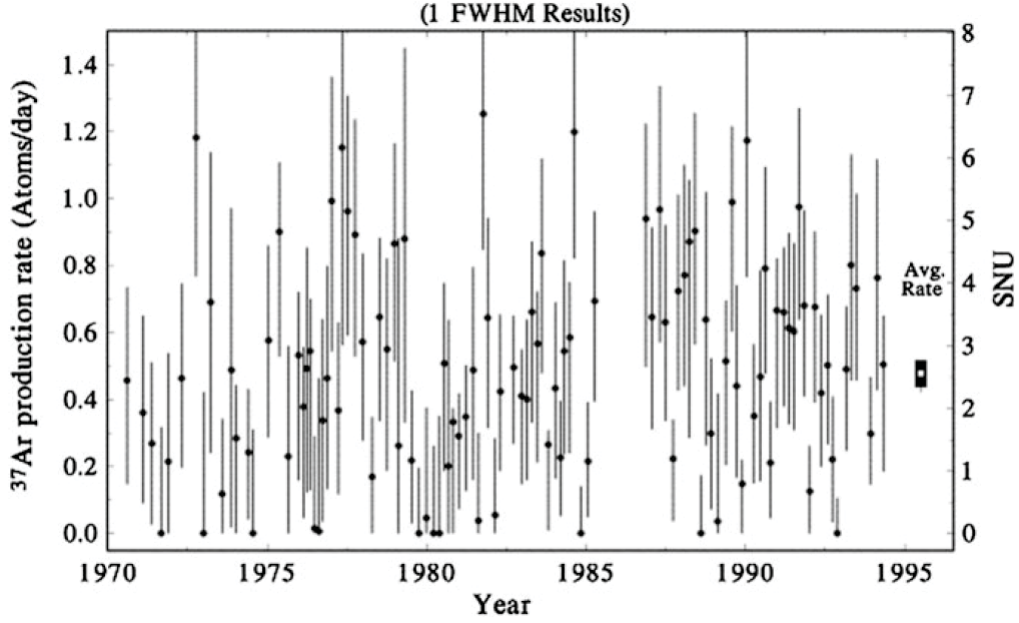
FIGURE 2.5: Results for 108 individual solar neutrino observations made with the Homestake detector. The production rate of ^{37}Ar shown has already had all known sources of nonsolar ^{37}Ar production subtracted from it. [4]

but with a much lower energy threshold.

$$\nu_e +^{71} Ga \rightarrow e^- +^{71} Ge \quad (threshold \quad 233 \, keV)$$
$$^{71}Ge \rightarrow^{71} Ga + \nu_e + Auger \, electron \, . \tag{2.42}$$
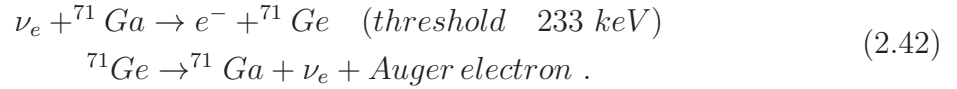
There were three ^{71}Ga experiments, GALLEX (GALLium EXperiment), GNO (Gallium Neutrino Observatory) and SAGE (Soviet American Gallium Experiment). With better signal rates, these experiments all reported the detection of half of the solar neutrino flux predicted by the SSM. The apparent deficit of the solar neutrino flux compared to theory shows that there must be some underlying physics we didn't understand.

This solar neutrino anomaly was finally solved later by the Sudbury Neutrino Observatory (SNO) experiment. One good way to verify that neutrino oscillations are the reason for this anomaly is to measure the total neutrino flux:

$$\phi_\nu = \phi_{\nu_e} + \phi_{\nu_\mu} + \phi_{\nu_\tau} \, , \tag{2.43}$$

using the neutral current interactions. The cross section of neutral current interactions does not depend on the neutrino flavour. Therefore, even if the flavour of a neutrino changes due to neutrino oscillation, the total flux can still be measured.

Because of this benefit, SNO used a 1,000 ton heavy water (D_2O) Čerenkov detector (details of Čerenkov detectors will be explained in the next subsection), sensitive to neutrino interactions through three different interaction processes:

$$
\begin{aligned}
Elastic\ scattering\ (ES) &: \ \nu_x + e^- \longrightarrow \nu_x + e^- \ , \\
Charged\ current\ (CC) &: \ D + \nu_e \longrightarrow 2p + e^- \ , \\
Neutral\ current\ (NC) &: \ D + \nu_x \longrightarrow p + n + \nu_x \ .
\end{aligned}
\tag{2.44}
$$

In the CC process, only ν_e are involved in this interaction. In the ES process, the cross section of $\nu_e e^-$ scattering $\sigma_{\nu_e,e}$ is significantly larger than that of $\nu_{\mu/\tau} e^-$ scattering $\sigma_{\mu/\tau,e}$. On the other hand, in the NC process, the cross section does not depend on the neutrino flavor. In the end, we can determine the flux as

$$
\begin{aligned}
\phi_{ES} &= \phi_{\nu_e} + 0.155(\phi_{\nu_\mu} + \phi_{\nu_\tau}) \ , \\
\phi_{CC} &= \phi_{\nu_e} \ , \\
\phi_{NC} &= \phi_{\nu_e} + \phi_{\nu_\mu} + \phi_{\nu_\tau} \ .
\end{aligned}
\tag{2.45}
$$

Figure 2.6 summarizes the result from the SNO experiment. The measured fluxes are[27]

$$
\begin{aligned}
\phi_{ES} &= 2.35 \pm 0.22(stat.) \pm 0.15(sys) \times 10^6 \ cm^{-2}s^{-1} \ , \\
\phi_{CC} &= 1.68 \pm 0.06(stat.)^{+0.08}_{-0.09}(sys) \times 10^6 \ cm^{-2}s^{-1} \ , \\
\phi_{NC} &= 4.94 \pm 0.21(stat.)^{+0.38}_{-0.34}(sys) \times 10^6 \ cm^{-2}s^{-1} \ .
\end{aligned}
\tag{2.46}
$$

Since ν_μ and ν_τ cannot be generated in SSM, the result of non-zero $\nu_\mu + \nu_\tau$ is strong evidence of neutrino oscillation. It also shows that only a third of the total ν_e produced arrived as such at earth. The measured oscillation parameters based on a two-flavour model are[27]

$$
tan^2\theta_{12} = 0.427^{+0.033}_{-0.029}, \quad \Delta m^2_{21} = 5.6^{+1.9}_{-1.4} \times 10^{-5} \ eV^2 \ .
\tag{2.47}
$$
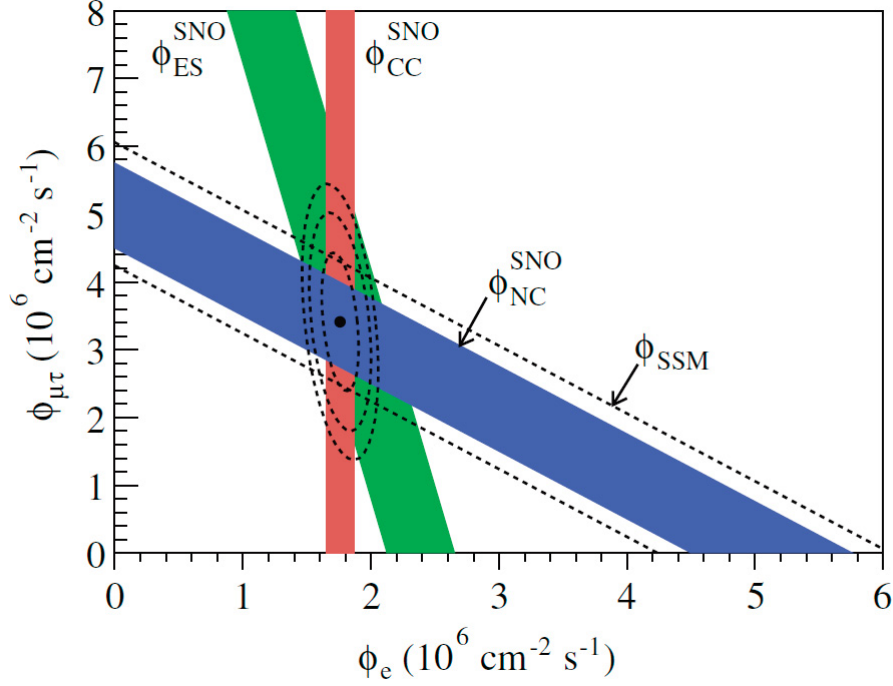
FIGURE 2.6: Flux of ^{8}B solar neutrinos that are μ or τ flavour vs. flux of electron neutrinos deduced from the three neutrino reactions, ES, NC and CC, in SNO ($1 \pm \sigma$ allowed region). The bands intersect at the fit values for ϕ_e and $\phi_{\mu\tau}$ indicating that the combined flux results are consistent with neutrino-flavour transformation.[5] Copyright 2006 by American Physical Society

2.2.0.2 Atmospheric Neutrino Oscillation Experiments

The atmospheric neutrinos are generated by interactions between cosmic-rays and oxygen or nitrogen nuclei in the atmosphere. Charged pions are produced first from the interactions. These then decay to muons (and ν_μ neutrinos) which finally decay to electrons (and neutrinos). The production process of atmospheric neutrinos can be briefly expressed as:

$$
\begin{aligned}
\pi^\pm &\to \mu^\pm + \nu_\mu/\bar{\nu}_\mu \ , \\
\mu^\pm &\to e^\pm + \nu_e/\bar{\nu}_e + +\nu_\mu/\bar{\nu}_\mu \ .
\end{aligned}
\tag{2.48}
$$

Figure 2.7 shows the basic technique to estimate the baseline between the source of neutrinos and the detector. It can be estimated by the reasonable assumption that the distance between the original generation position in the atmosphere to the closest surface of earth can be ignored. Since the neutrinos can penetrate the earth and be detected at the opposite side, the distance between the position of the source to the detector can be estimated by the direction of the neutrino being detected. We just need to track back

along this direction to the other side of the earth, then the distance between detector and the point on the surface of earth at the opposite side is the L value we need.
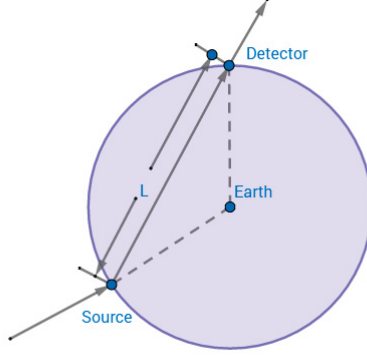
FIGURE 2.7: Demonstration about how to estimate baseline in atmospheric neutrino oscillation experiments.

Based on interactions listed in Eq. (2.48), we can reach a simple prediction that the ratio of the number of the muon-type neutrinos to electron-type neutrinos should be 2.

$$\frac{N(\nu_\mu) + N(\bar{\nu}_\mu)}{N(\nu_e) + N(\bar{\nu}_e)} = 2 \ . \tag{2.49}$$

However, early observations made by the IMB and Kamiokande experiments showed that the ratio is roughly one. Similar to the solar neutrino anomaly, this was called the atmospheric neutrino anomaly. This anomaly was finally solved by the Super-Kamiokande (SK) detector. Actually, the verification of the atmospheric neutrino oscillation from experiment is the first definite evidence of the existence of neutrino oscillation.

The SK detector is located 1,000m below the Ikenoyama mountain in the Gifu prefecture, Japan. It uses 50,000 tons of ultra-pure water as the neutrino target. From the charged current interactions in water, electrons and muons are produced by the processes Eq. (2.50)

$$\begin{aligned} \nu_\mu + A &\to \mu + X \ , \\ \nu_e + A &\to e + X \ . \end{aligned} \tag{2.50}$$

Charged particles with velocity $\beta > 0.75$ in water emit $\check{C}$erenkov light. 11,200 20-inch photo-multipliers (PMT) are mounted at the inner wall of the detector to detect the $\check{C}$erenkov light. Because muons will produce a clear $\check{C}$erenkov ring in water, but electrons will generate an electromagnetic shower in the water, and electrons and positrons in the shower will generate a blurred $\check{C}$erenkov ring. So distinguishing between ν_μ and ν_e signals is based on the different pattern of the $\check{C}$erenkov ring detected. Figure 2.8 briefly shows the difference between these two patterns.
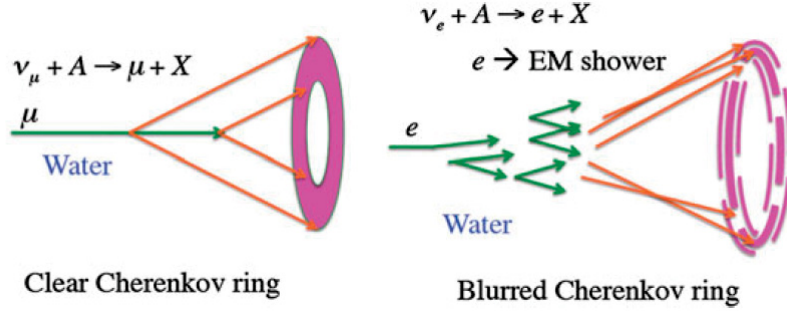
FIGURE 2.8: Particle identification in a water $\check{C}$erenkov detector.[2]

The direction of the muon can also be measured from the direction of the $\check{C}$erenkov ring, since the charged leptons created from charged current interactions go forward with respect to the original direction of the incoming neutrinos. With this direction information, the distance between the source where it is generated and the detector can be estimated, as explained before. If the muon is produced and stops within the detector, which is called the fully contained event, then the muon energy can be measured by the total $\check{C}$erenkov light yield and the original neutrino energy can be deduced from it.

Figure 2.9 shows the SK experiment result. Figure 2.9 (a) shows a clear decrease of the ratio of detected ν_μ to the expected result with increasing of the L/E ratio. This is a good explanation for the atmospheric neutrino anomaly detected before. The relatively stable ν_e rate shows that the oscillation is mainly due to $\nu_\mu \to \nu_\tau$. Also since not only the signal rate, but also energy of the neutrino and its baseline are being detected, Δm^2 and $sin^2 2\theta$ can be deduced from it and are shown in figure 2.9 (b).

Figure 2.10 shows the recent results of L/E dependence of the ν_μ events from SK. There is a dip at around $L/E \sim 6 \times 10^2$ km/GeV indicating that the oscillation with $\Delta m^2 \sim 2 \times 10^{-3}$ eV^2. The up-to-date oscillation parameters measured by the SK group at 90% confidence level (CL)[28] are

$$0.407 < sin^2\theta < 0.583, \quad 1.7 \times 10^{-3} < \Delta m^2 < 2.7 \times 10^{-3}\ eV^2\ . \tag{2.51}$$
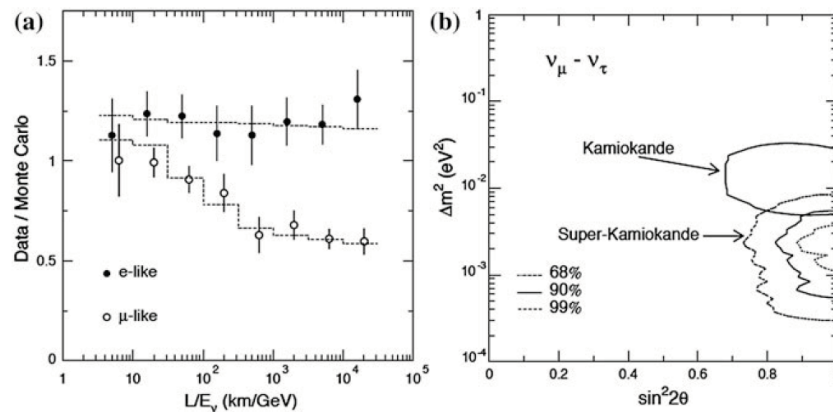
FIGURE 2.9: The historical SK data show the first evidence of neutrino oscillations. (a) The ration of the fully contained Data to Monte Carlo prediction as a fuction of L/E. The dashed line shows the expected oscillation between muon-type neutrino and tau-type neutrino at $\Delta m^2 = 2.2 \times 10^{-3}$ eV^2 and $\sin^2 2\theta = 1$. It clearly shows the rate of muon-type neutrinos decreases while electron-type neutrinos stays constant. (b) Confidence intervals for $\sin^2 2\theta$ and Δm^2 for $\nu_\mu \longleftrightarrow \nu_\tau$ two-neutrino oscillations.[6] Copyright 1998 by the American Physical Society
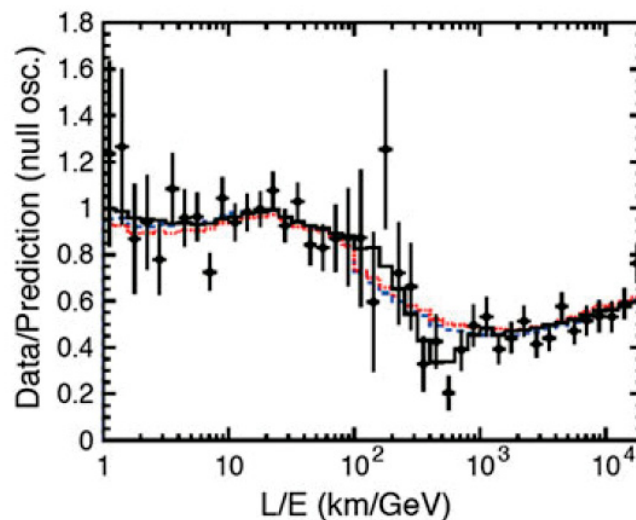
FIGURE 2.10: Result of the L/E analysis from SK experiment. The horizontal axis is the reconstructed L/E. The points shows the ratio of the data to the simulation prediction without oscillation. The error bars are statistical only. The solid line shows the best fit with 2-flavour oscillation.[7] Copyright 2004 by American Physical Society

2.2.0.3 Accelerator Neutrino Oscillation Experiments

In accelerator neutrino oscillation experiments, almost 100% of the neutrinos are produced from charged pion decays which are introduced in the atmospheric neutrino section.

$$\pi^{\pm} \rightarrow \mu^{\pm} + \nu_{\mu}/\bar{\nu}_{\mu} \ . \tag{2.52}$$

This makes it suitable for studying the oscillation of the muon-type neutrinos. Since the typical energy of accelerator neutrino is of the order of GeV, a baseline of several hundred kilometers is necessary to study with the information of Δm^2 gotten from atmospheric neutrino oscillation experiments. Figure 2.11 shows the actual scale of the distance between K2K, T2K experiments and accelerators.

FIGURE 2.11: Locations of accelerators and detectors for K2K and T2K experiments. [Google map][2]

K2K is the accelerator experiment that measures a clear neutrino signal. The neutrino beam was produced by the newly constructed neutrino beam line at the KEK proton synchrotron as shown in figure 2.12. A 12 GeV proton beam was fired into the target to produce secondary particles. A pair of toroidal horn magnets downstream focused π^+'s to direct the beam at the SK detector, located 250 km away.[2] The ν_{μ} beam was produced from the pion decay in the decay pipe. The front detector was used to measure the neutrino spectra to normalize the events by the far detector. The measurement is based on the detection of $\check{C}$erenkov light introduced before.

Figure 2.13 (a) shows the energy distribution of the detected ν_{μ}. There is a dip at $E \sim 0.7$ GeV indicating that $\Delta m^2 \sim 3 \times 10^{-3}$ eV². Figure 2.13 (b) shows the fitting results for Δm^2
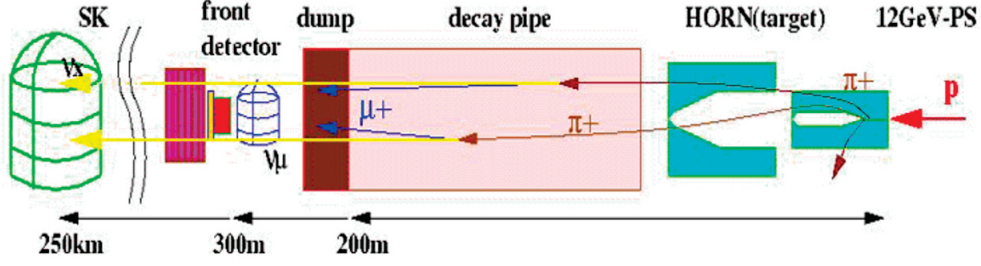
FIGURE 2.12: K2K neutrino beam production and detection.[8]

and $\sin^2 2\theta$. These results agree with the atmospheric neutrino measurements, indicating that both of the experiments are observing the same oscillation.
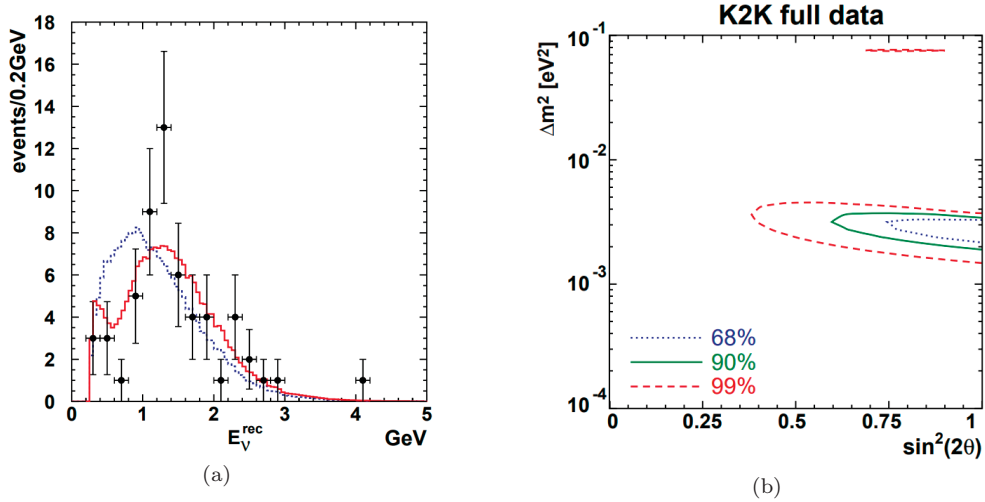
FIGURE 2.13: (a) The reconstructed E_ν distribution for the 1-ring μ-like sample. Points with error bars are data. The solid line (red) is the best fit spectrum with neutrino oscillation and the dashed line (blue) is the expectation without oscillation. These histograms are normalized by the number of events observed[9]. (b) Allowed regions of oscillation parameters. Three contours correspond to the 68% (dotted line), 90% (solid line) and 99% (dashed line) CL. allowed regions, respectively.[10] Copyright by 2006 American Physical Society

The T2K experiment is the successor to the K2K experiment. Muon neutrinos are produced by the decay of pions, which are produced by a 30 GeV proton beam from the J-PARC proton synchrotron. The neutrinos are sent to the SK detector, located 295 km away. The neutrino beam T2K uses is an off-axis beam[29], which provides neutrinos with a narrower energy distribution.

As discussed previously, atmospheric neutrino oscillation shows that the $\nu_\mu \to \nu_e$ oscillation probability is small. With high ν_μ statistics, T2K is able to observe the $\nu_\mu \to \nu_e$

appearance signals. As of the year 2013, the T2K group has identified 28 $\nu_\mu \to \nu_e$ candidate events while the expected background is 4.9 events. With the knowledge of the $\nu_\mu \to \nu_e$ oscillation, the updated oscillation parameters measured by T2K are[30]

$$sin^2\theta_{32} = 0.514, \quad |\Delta m^2_{32}| = 2.51 \times 10^{-3} \ eV^2 \ . \tag{2.53}$$

2.2.0.4 Reactor Neutrino Oscillation Experiments

In reactor neutrino oscillation experiments, the neutrinos are produced in the fission reactions of elements like uranium and plutonium. An example of such a fission reaction process is shown in figure (2.14). As this example shows, with this kind of process, a lot of electron antineutrinos ($\bar{\nu}_e$) are created by β decay. So reactor neutrino oscillation experiments are mainly designed to measure the survival probability of antineutrinos ($P_{\bar{\nu}_e \to \bar{\nu}_e}$).
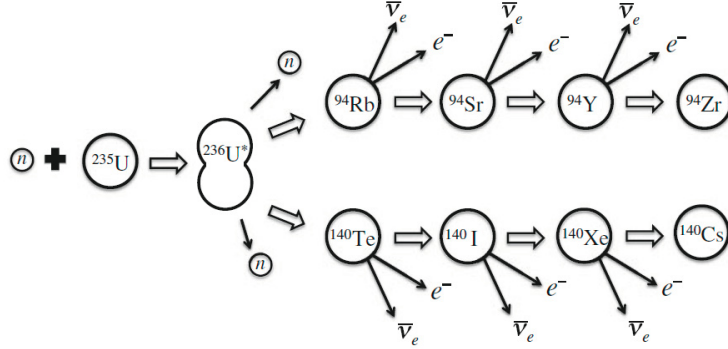
FIGURE 2.14: An example of the fission reaction. $\bar{\nu}_e$s are generated in decays of fission products.On average about six $\bar{\nu}_e$s are generated per fission. About 6×10^{20} ν_es/sec are generated in a reactor operating at $3GW_{th}$. The energy of the neutrinos is a typical decay energy of a few MeV[2]

The common way to detect the electron antineutrinos created during the fission process is the Inverse Beta Decay (IBD) process. It is a nuclear reaction involving electron antineutrino and proton, the interaction between them creating a positron and a neutron. The process can be expressed as :

$$\bar{\nu}_e + p \to e^+ + n \ . \tag{2.54}$$

Since this is also the major reaction NuLat uses to detect the anti-electron neutrinos created by reactor, the detail of this reaction will be explained in the next section.
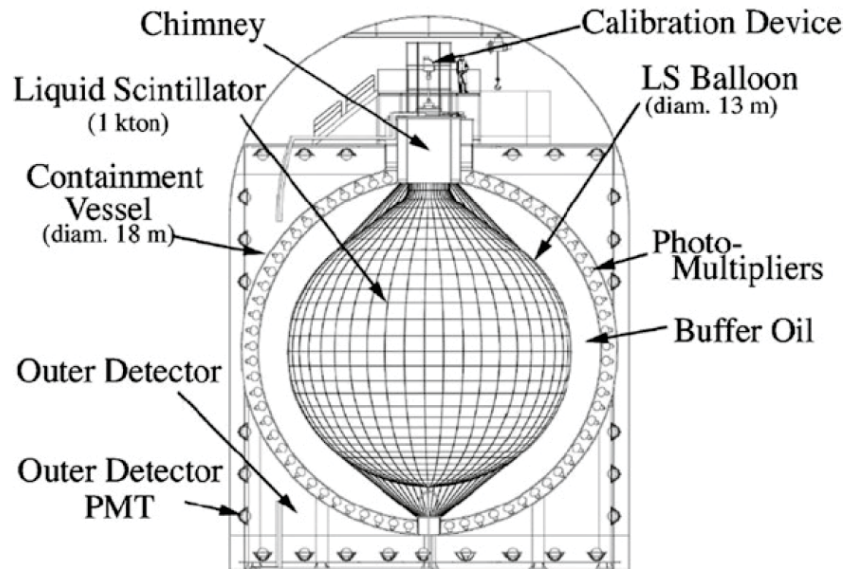
FIGURE 2.15: Schematic diagram of the KamLAND detector.[11]

The KamLAND experiment uses 1,000 tons of liquid scintillator to detect reactor neutrinos coming from reactors hundreds of kilometers away. Around 70 reactors are spread throughout Japan and Korea around KamLAND detector providing an average baseline of 180 km.[2] Figure 2.15 shows a sketch of the KamLAND detector. This detector is housed in the cavern where the Kamiokande detector used to be. The location is 1,000m below the top of the IKenoyama mountain, so the cosmic-ray rate is reduced by a factor of 10^{-5} compared with the surface.

Figure 2.16 shows the L_0/E_ν dependence of the survival probability of $\bar{\nu}_e$, where $L_0 = 180\ km$ is the flux-weighted average baseline. The best fit of the three flavour analysis of only the KamLAND data indicates[12]

$$tan^2\theta_{12} = 0.481^{+0.033}_{-0.029}, \quad \Delta m^2_{21} = 7.54^{+1.92}_{-1.36} \times 10^{-5}\ eV^2\ . \tag{2.55}$$

The L/E scale make the measurement by KamLAND a good comparison to the solar neutrino oscillation experiments. Figure 2.17 shows the allowed oscillation parameter region from KamLAND together with the result of the solar neutrino experiments. The results are consistent with each other. Since KamLAND observes $\bar{\nu}_e$ disappearance and solar neutrino experiments measures ν_e disappearance, the agreement shows that CPT invariance holds here.
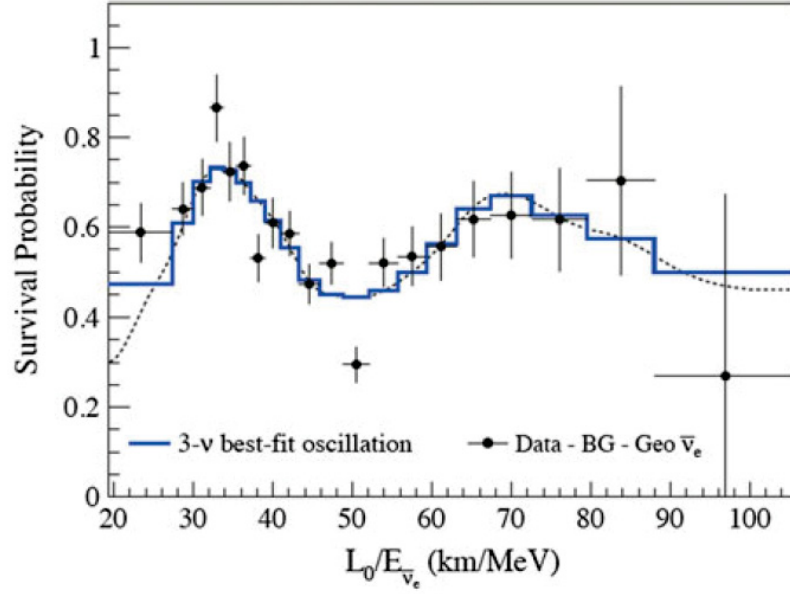
FIGURE 2.16: Ratio of the observed $\bar{\nu}_e$ spectrum to the expectation for non-oscillation versus L_0/E_ν. $L_0 = 180\ km$ is the flux-weighted average reactor baseline. [12]
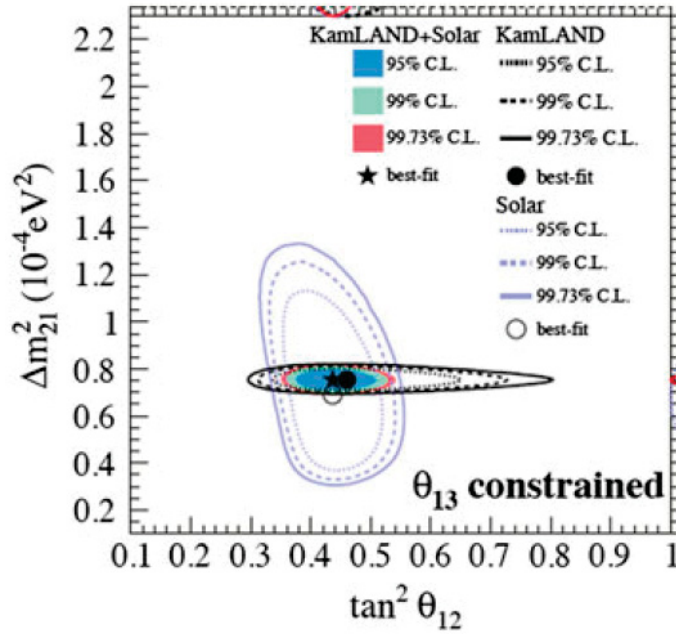
FIGURE 2.17: Allowed $(tan^2\theta - \Delta m^2)$ regions from the KamLAND together with the summary result of solar neutrino experiments. [13]

The Double Chooz (DC), Daya Bay (DB) and RENO experiments are new reactor neutrino experiments, which measure the reactor $\bar{\nu}_e$ oscillation at baselines of $1 \sim 2$ km. They are sensitive to the region $\Delta m^2 \sim 2 \times 10^{-3} \ eV^2$, which corresponds to the parameter observed in ν_μ disappearance by the accelerator and atmospheric neutrino experiments. These three experiments use the near and far detectors with identical structure to significantly improve the accuracy of the neutrino deficit measurement.[2] The baseline of the far detectors are close to the oscillation maximum ($L \sim 1.5 \ km$) and the baselines of the near detectors are where the oscillation is still small ($L \leq 400m$). Since both detector sets have an identical structure, most of the systematic uncertainties are canceled out by comparing the data from the far and near detectors, and the precise measurement of the $\bar{\nu}_e$ disappearance is possible.
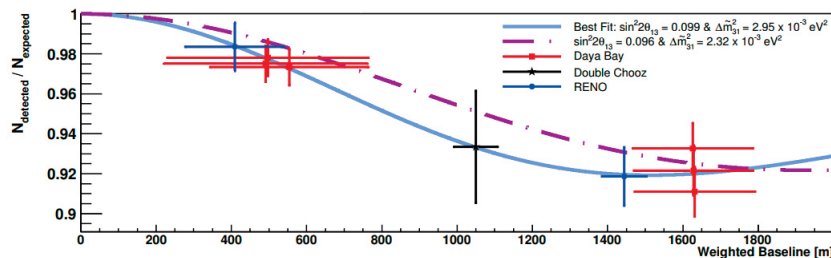
FIGURE 2.18: Baseline dependence of reactor $\bar{\nu}_e$ survival probability from Daya Bay, Double Chooz and RENO. The solid line is the best fit oscillation pattern. Each detector sees several reactors. The horizontal axis is a weighted baseline and the horizontal error bar in each data point shows the standard deviation of the distribution of the baseline.[31]

The measured $\bar{\nu}_e$ survival probabilities are shown in the figure 2.18 for the different baseline of these 3 experiments. The baseline dependence of the neutrino deficits shows that[31]:

$$sin^2\theta_{13} = 0.099^{+0.013}_{-0.012}, \quad \Delta m^2_{31} = 2.95^{+0.42}_{-0.61} \times 10^{-3} \ eV^2 \ . \tag{2.56}$$

2.3 Open Questions NuLat Can Help

In last section, we introduced different neutrino oscillation experiments that have been run in the past. It shows that many questions have been answered by various experiments. The Solar neutrino anomaly has been solved by SNO and the atmospheric neutrino anomaly has been characterized by the SK detector. Some oscillation parameters have

been measured and we are expecting the precision determination phase now. In this section, we discuss some open questions with which NuLat and its unique properties may be able to help.

2.3.1 Light Sterile Neutrino Searches

The results presented in the last section are in the framework of the three flavour model. However, there are some experiments whose results cannot be explained by this framework and might require extra neutrinos into it. We call this kind a sterile neutrino because it should not participate in the weak interaction as a normal active neutrino does.

The first experiment to report results which imply this idea is the LSND experiment. It was an accelerator neutrino experiment designed to measure the $\nu_\mu \to \nu_e$ oscillation. The observation showed an excess of ν_e events which imply a Δm^2 in the range of $0.2 - 10$ eV^2 [32]. This anomaly is being tested by Fermilab's MiniBooNE (Mini Booster Neutrino Experiment) in both neutrino and antineutrino mode. The results obtained in the neutrino mode disfavour most of the parameter space defined by LSND but were not conclusive [33]. On the other hand, the result obtained in the antineutrino mode were consistent with the LSND signal and consistent with a mass splitting of between 0.1 and 1 eV^2 [34].

Further hints of the existence of sterile neutrinos came from the gallium solar neutrino experiments GALLEX [35], SAGE [36] discussed in the last section. Both these experiments used high-activity electron-capture sources to calibrate their detectors. The sources that were employed were ^{51}Cr and ^{37}Ar sources. These sources emit ν_e from the electron capture reactions as:

$$
\begin{aligned}
e^- + {}^{51}Cr &\to {}^{51}V + \nu_e \ , \\
e^- + {}^{37}Ar &\to {}^{37}Cl + \nu_e \ .
\end{aligned}
\tag{2.57}
$$

Averaging the observed production rates in the source measurements and dividing by the expected rate, a deficit of $\sim 14\%$ is observed. This discrepancy could be explained by short baseline oscillations with $\Delta m^2 \sim 1$ eV^2.

Another anomaly implying the same issue is known as the reactor neutrino anomaly. The re-evaluation of the expected antineutrino flus from nuclear fission indicates that the measured flux is about 6% below the prediction with 3σ significance, as shown in figure
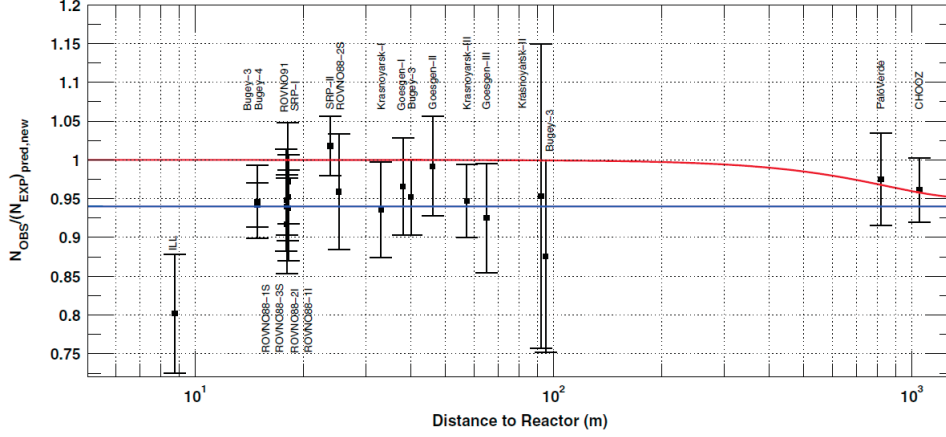
FIGURE 2.19: Illustration of the short baseline reactor antineutrino anomaly. The experimental results are compared to the prediction without oscillation, taking into account the new antineutrino spectra, the corrections of the neutron mean lifetime, and the off-equilibrium effects. Published experimental errors and antineutrino spectra errors are added in quadrature. The mean averaged ratio including possible correlations is 0.943 ± 0.023. The red line shows a possible three-active neutrino mixing solution, with $sin^2 2\theta_{13} = 0.06$. The blue line displays a solution including a new neutrino mass state, such as $|\triangle m^2_{new,R}| \gg 1eV^2$ and $sin^2 2\theta_{new,R} = 0.12$ (for illustration purpose only).[14] Copyright by 2011 American Physical Society

2.19. This can be explained by the sterile neutrino oscillation with a mass split of about 2.4 eV^2.

To explain these anomalies found in experiments, some models including sterile neutrinos have been proposed, the details of which can be found in Ref[21]. The most important models for the mixing between the active neutrinos and light sterile neutrinos are the so-called 3+1, 3+2, and 1+3+1 models[21]. Oscillation physics describe these model with a rectangular mixing matrix $U_{\alpha i}$ with $\alpha = e, \mu, \tau$ and $i = 1, 2, 3, +s$ and $\Sigma_i U^*_{\alpha i} U_{\beta i} = \delta_{\alpha\beta}$ where s denotes how many sterile neutrinos are involved in the theory. To simplify the theory we have to deal with, we briefly discuss the 3+1 model here. In the 3+1 model, the rectangular mixing matrix describing the physics becomes a 3×4 matrix. To simplify the case, an approximation called short baseline limit (SBL), can be employed. In this approximation we set the solar and atmospheric mass splittings to zero[21]. With this approximation, the mixing matrix only depends on the three angles that mix the active mass states with the sterile mass states: θ_{14}, θ_{24} and θ_{34}[21]. Then for our specific motivation to detect the survival probability of reactor neutrinos, the formula should be:

$$P^{SBL}_{ee} = 1 - sin^2 2\theta_{14} sin^2 (\frac{\Delta m^2_{41} L}{4E}) \ . \tag{2.58}$$
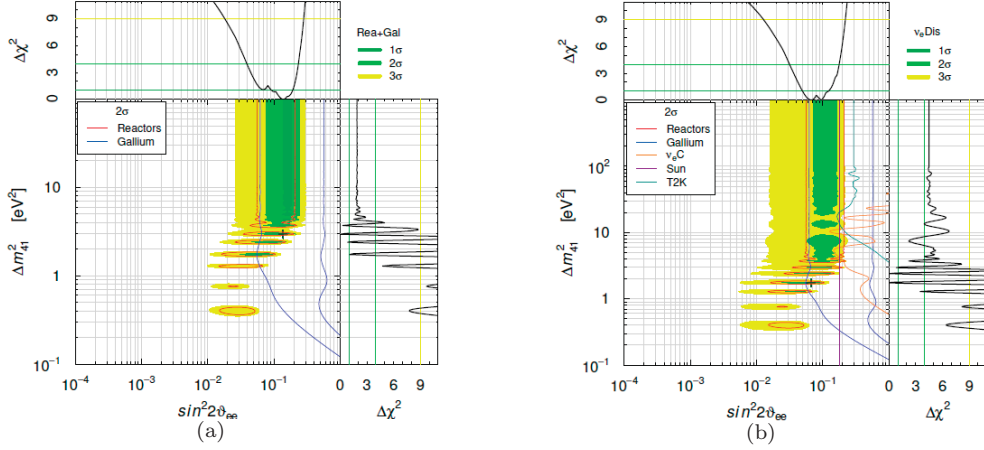
FIGURE 2.20: Allowed regions in the $sin^{2\theta_{ee}} - \Delta m_{41}^2$ plane and marginal $\Delta \chi^2$ for $sin^{2\theta_{ee}}$ and Δm_{41}^2 obtained from (a) the combined fit of the reactor and Gallium data; (b) the combined fit of ν_e and $\bar{\nu}_e$ disappearance data. [15]

Figure 2.20 summarized the updated allowed region in $sin^2\theta_{ee} - \Delta m_{41}^2$. This summary is cited from Ref[15]. Figure 2.20 (a) shows the combined fit of reactor[14] and Gallium data[36–40]. The 3σ allowed regions in the $sin^2\theta_{ee} - \Delta m_{41}^2$ plane are confined to $0.010 \lesssim sin^2\theta_{ee} \lesssim 0.30$ and $\Delta m_{41}^2 \gtrsim 0.35$ eV^2. Besides the reactor and Gallium data, short baseline ν_e disappearance is constrained by solar and KamLand neutrino data. Updated KamLAND constraint[40] and solar data from SK experiment[41] and Borexino[42] with the reactor and Gallium data are combined and shown in figure 2.20 (b). Since the analysis of solar+KamLAND does not show any indication of short baseline ν_e disappearance, the combination with reactor and Gallium data shifts the allowed regions in the $sin^2\theta_{ee} - \Delta m_{41}^2$ plane to smaller value of $sin^2\theta_{ee}$ region around $0.0054 \lesssim sin^{2\theta_{ee}} \lesssim 0.23$. On the other hand, Δm_{41}^2 does not change a lot with these two different fit. Using the updated constraint of allowed $sin^2\theta_{ee} - \Delta m_{41}^2$ value, the Daya Bay group offers another possibility that the reactor anomaly might not from the active to sterile neutrino oscillation, but just from the overestimate of the ^{235}U fission neutrino spectrum[43].

Although there are currently cons and pros to the existence of active-sterile neutrino oscillation, it is still an open question worth more accurate measurement to resolve the confusion. The NuLat detector can be a good candidate to join this community with its good energy resolution, mobility and compact volume.
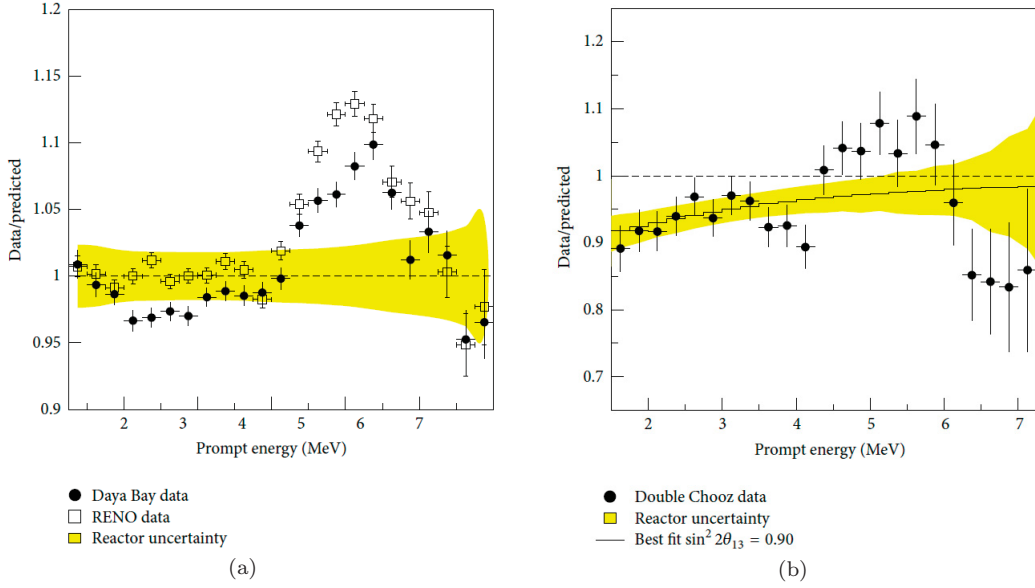
FIGURE 2.21: Ratio of background-subtracted $\bar{\nu}_e$ candidates to non-oscillation prediction, as a function of the IBD prompt energy. (a) Daya Bay and RENO ratios for $\bar{\nu}_e$ candidates observed at the near sites. (b) Double Chooz ratio for $\bar{\nu}_e$ candidates measured at the far detector. The shadowed region represents the typical reactor error derived from the [16,17] reference $\bar{\nu}_e$ spectra, which is dominant for the considered energy region. [18]

2.3.2　5 MeV Bump In The Reactor Antineutrino Spectrum

Another unexpected result from several reactor neutrino experiments which makes people confused is the strange energy structure around 5 MeV. The RENO collaboration first mentioned the observation of an excess in the number of antineutrinos between 4 and 6 MeV of the positron energy spectrum in the Neutrino 2012 conference [44]. In 2014, both RENO and Double Chooz collaborations reported and quantified such an excess [45–47]. Daya Bay also presented a similar energy structure at the ICHEP 2014 and at NuTel 2015 conferences [48]. Figure 2.21 shows this strangeness detected by all three experiments.

Since the NuLat detector is designed as a movable compact short baseline reactor neutrino detector, it should be useful to verify or disprove this spectral feature.

Chapter 3

Introduction to NuLat Detector

As briefly mentioned in chapter 1, the design of the NuLat detector is based on the Raghavan Optical Lattice (ROL) concept to make it an effective short baseline reactor neutrino detector. In this chapter, we first introduce the Inverse Beta Decay reaction (IBD) which is the key detection reaction. Then we move on to introduce the ROL concept and explain how this concept can help improve the detector. After these introductions, we show an estimation we made related to the sensitivity of the NuLat detector to the regime where we may observe active to sterile oscillations explained in the previous chapter.

After this introduction to the physics ideas and predictions, we introduce the current version of the NuLat detector which is the first active one. Also the data acquisition system (DAQ) used by current NuLat detector are introduced.

3.1 Introduction to NuLat

3.1.1 Neutrino Detection With IBD Reaction

The basic neutrino detection idea of NuLat is based on the inverse beta decay (IBD) reaction of electron antineutrino with a proton as introduced earlier. The reaction can be expressed as :

$$\bar{\nu}_e + p \rightarrow e^+ + n \ .$$

$$(3.1)$$

The energy threshold of this reaction is 1.8 MeV arising from the mass difference between original proton and produced electron and neutron, so only the $\bar{\nu}_e$ with energy larger than this value can be detected. The IBD cross section can be estimated as[2]

$$\sigma_{IBD} \sim 1.0 \times 10^{-43} E_{e+} p_{e+} \ cm^2 \ , \tag{3.2}$$

where E_e and p_e are energy and momentum of the generated positron measured in MeV and the neutron lifetime of 880 s is assumed. The antineutrino flux decreases with increasing energy, but the cross section in Eq (3.2) increase with increasing energy. The convolution of these two effect gives us a relatively fixed range where detection with this reaction is effective. Figure 3.1 shows the example from these two effects. The threshold of 1.8 MeV is also contained in this figure.
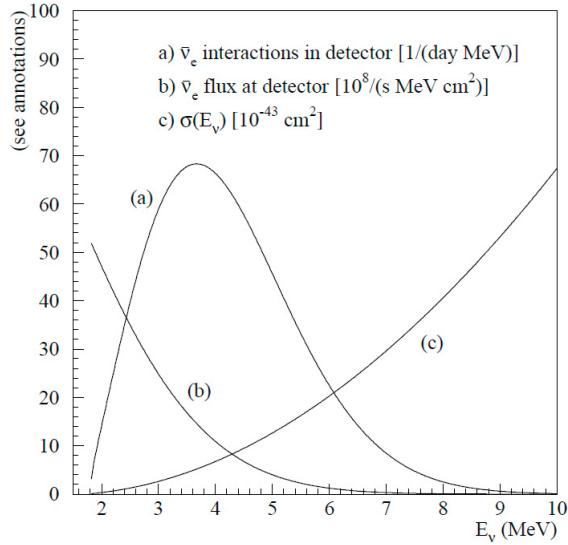
FIGURE 3.1: Assuming a 12-ton fiducial mass detector located 0.8 km from 12-GWth power reactor, $\bar{\nu}_e$ interaction spectrum in the detector (curve (a)) and reactor $\bar{\nu}_e$ flux at the detector (curve (b)) are shown as a function of energy. Inverse -decay cross section (curve (c)) is also shown.[19] .

The e^+ will carry most of the energy from $\bar{\nu}_e$ due to the small mass of it relative to the neutron. The signal and energy of e^+ can be directly measured by the scintillator as a prompt signal. The neutron produced from this process can also be detected by a neutron capture process. For the NuLat detector specifically, we use scintillator from Eljen which is already pre-doped with ^6Li. So the neutron capture process is:

$$^6Li + n \longrightarrow^7 Li^* \longrightarrow \alpha +^3 H + 4.8 \ MeV \ . \tag{3.3}$$

This process is delayed by the capture time of the neutron. How long between prompt and delayed signal depends on the doping level. These two signals with known delay between them offer a unique property for requiring time coincidence events during the detection. This property can help to reduce random background substantially.

3.1.2 Light Transmission Property Of ROL Based Detector

As introduced before, NuLat is based on the ROL concept. In this section, we discuss how this concept can help us make a detector with geometrical reconstruction ability. The key part of the ROL concept is the total internal reflection of light through the interface between mediums with different indices of refraction. The critical angle of total internal reflection can be calculated by Snell's law:

$$\theta_c = arcsin\big(\frac{n_{gap}}{n_{scin}}\big) \ , \tag{3.4}$$

where θ_c is the critical angle, n_{gap} and n_{scin} are refractive index of scintillator and the gap between them. As long as the angle of incident light is greater or equal to the critical angle θ_c, the light will go through this total internal reflection process. If we define a cubic shape as our scintillator cell, the photons created by the energy deposition of different particles will go through this kind of reflection. The cubic shape helps to make sure that the photons reflected by a surface can be guided to go through the other surfaces that are perpendicular to the original surface. Once the photons transmit through a surface, it will go along the same direction through different cubes since every total internal reflection after this will be the same as the first reflection. Figure 3.2 shows what this process looks in 2D and 3D version.

Based on these ideas, a ROL detector has a structure that a series of scintillators having cubic shape are separated by a small gap that has a lower index of refraction than the scintillator. We call each cubic scintillator a cell. Good arrangement of these cells and gaps will make sure that the light can be guided along with three Cartesian axes by total internal reflection as figure 3.2 shows. Since each cell faces one specific PMT, we can easily track back from these PMTs to locate the specific cell where the photos come from. This give us a good ability to reconstruct the geometric information of each event.

To have a good understanding of what kind of critical angles we need for a ROL based detector, we started the calculation from a 2D version first. Figure 3.3 (a) shows how
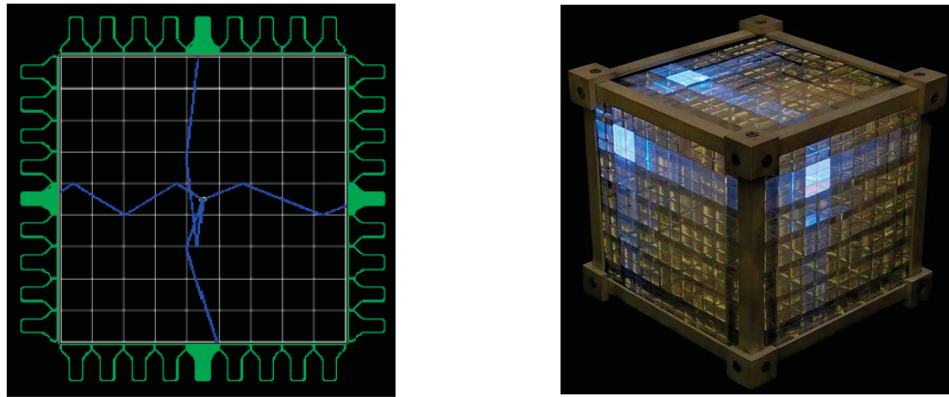
(a) A cartoon drawing of light path in a 2D ROL.

(b) A 3D demostration of ROL light channeling ability.

FIGURE 3.2: 2D and 3D light channeling demonstration of ROL.[20]
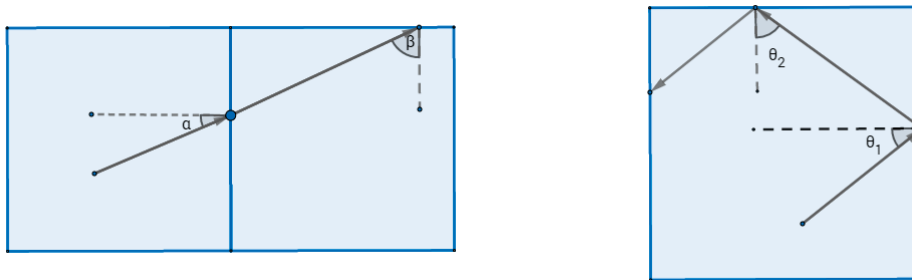
(a) Demonstration of light being transmitted through a fixed Cartesian axes.

(b) Demonstration of light being trapped in one cell.

FIGURE 3.3: Demonstration about light transmission in 2D case.

it looks when light being transmitted through fixed Cartesian axes in a 2D case. Light incident to the left edge with angle of α goes through the interface of the two cell boundary and keeps traveling until it hits the top edge of the second cell with incident angle β. Since each cell is a square on a plane, the angles between top and side edges are 90° and the relation of angle α and β is easily found to be $\beta = 90° - \alpha$. To make sure that all the light should be guided along fixed Cartesian axes as designed, the critical angle θ_c should between angles of α and β such that,

$$\alpha \leq \theta_c \leq \beta \ . \tag{3.5}$$

Since we already know that

$$\beta = 90° - \alpha \ , \tag{3.6}$$

this makes

$$\alpha \leq \theta_c \leq 90° - \alpha \ . \tag{3.7}$$

To get the critical angle which will guide all the light by total internal reflection, it should satisfy relation (3.7) for any angle α. To meet this requirement, the minimum of critical angle can be is $\theta_c = \alpha$. So we can use this extreme condition to get

$$\theta_c \leq 90° - \theta_c \ , \tag{3.8}$$

which gives

$$\theta_c \leq 45° \ . \tag{3.9}$$

It shows directly that when $\theta \leq 45°$, all the light will be guided along the fixed Cartesian axes as designed. Besides this, figure 3.3 (b) also shows another condition which we called light trapping. It means light being reflected once from one edge cannot transmit through the second edge it hits, but is reflected again. After that all the angles of incidence during the travel of light will be the same as the first two, so this condition will happen infinitely until the light is absorbed by the material. The mathematical discussion will be similar to what we just gave. As figure 3.3 (b) shows, as long as both θ_1 and θ_2 are larger than θ_c, the light will be trapped. We know that $\theta_2 = 90° - \theta_1$. With these relation we can easily draw the conclusion that when $\theta_c < 45°$, there will be certain amount of light being trapped in one cell. Specifically say, light which incident angle θ_1 between θ_c and $45°$ will be trapped.

Now that we have discussed a simple 2D version of this ROL concept, we will discuss the 3D version which has slightly different requirements. The requirement that all light being transmitted through fixed Cartesian axes is the same as the 2D version which is $\theta_c \leq 45°$. The reason will be clear after we discuss another issue, which is the condition when light is trapped in one cube.

Figure 3.4 (c) shows an example of light being trapped in one cube. If the light is transmitted without scattering, then as long as it is reflected from one surface, it should be able to be transmitted through the second surface it hits which is perpendicular to the surface it was just reflected from as in the 2D discussion. If not, then the light will be
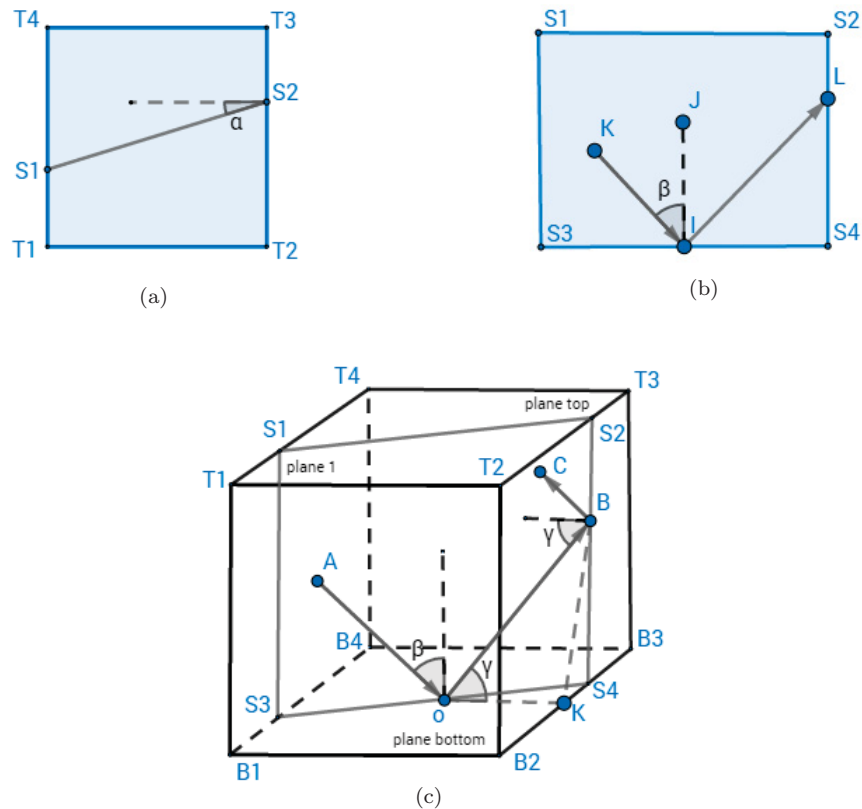
FIGURE 3.4: 3D geometry about light trapping demonstration. Figure (a) is the top view of the cube shown in (c). Angle between the plane which light travel on and the surface of the cube is labeled as α. Figure (b) shows the plane light travels on, the angle of incidence of light to the bottom plane is labeled as β. Figure (c) is a fully demonstration about all the information we need to understand this geometry.

trapped until it is absorbed by the material. In the 2D version, we get a conclusion that light with incident angle θ_1 between θ_c and $45°$ will be trapped. This relation is because the plane in which incident light and reflected light travel is the same as the square cell we defined. However in a 3D version, this relation is no longer valid. As figure 3.4 (c) shows, incident light along AO and reflected light along OB together define a plane noted as plane 1. Figure 3.4 (b) shows that how this plane looks from the top view. There is a angle α between the edge of this plane and the direction of the side plane.

To define the relation between the angle of incidence β , the angle between the plane the light is traveling on and the direction of the side plane α and the angle of incidence of the reflected light on the side plane γ, we add two dashed lines OK and BK to help define the mathematical relation. The point K is picked so that line OK is perpendicular to the line B2-B3. Then the angle between line OK and OB is the same to the angle γ.

First, we express line OK and BK as function of the angles (α and β) we concern and line OB. It can be easily obtained from the triangle relation as:

$$OK = OB \times sin(\beta) * cos(\alpha) \ , \tag{3.10}$$

$$BK = \sqrt{(OB \times cos(\beta))^2 + (OB \times sin(\beta) * sin(\alpha))^2} \ , \tag{3.11}$$

also we know that

$$cos(\gamma) = \frac{OK^2 + OB^2 - BK^2}{2OB * OK} \ , \tag{3.12}$$

combine relation (3.10), (3.11) and equation (3.12), we will get

$$cos(\gamma) = sin(\beta) * cos(\alpha) \ . \tag{3.13}$$

It is easily to tell that when $\alpha = 0°$, this relation comes to exactly the same condition as we discussed in the 2D version. Based on the figure 3.3 (c), we know that $0° \leq \alpha \leq 45°$. It shows that in the 3D condition, because of the angle α, γ can be larger then $90° - \beta$. With a fixed value of angle β, the increasing of angle α will increase the value of angle γ. It will cause the light which can be transmitted through in a 2D case being trapped because the angle γ becomes larger. To get the specific angle where no light will be trapped, we will examine the extreme condition. We assume that $\alpha = 45°$ which is the extreme condition to increase the incident angle of the light reflected once and hits on the second surface mostly. With a fixed angle α, the increasing of the angle β will cause the decreasing of angle γ. The smallest value of angle β which will cause the light being reflected is θ_c, so if the value of angle γ is also θ_c under this condition, then no light trapping will happen. Because the value of angle β can only increase to make the light being reflected once which will decrease the value of angle γ, it will make the angle γ smaller than θ_c and make sure the light will be transmitted during the second hit. So mathematically we will have the extreme condition as :

$$cos(\theta_c) = sin(\theta_c) * cos(45°) \ . \tag{3.14}$$

Material	Refractive Index
Teflon FEP	1.34
PVT Scintillator	1.52
Water	1.33
Air	1.00
Ultima Gold AB	1.56[49]

TABLE 3.1: Different material that have been considered for making ROLs.

It gives us that the extreme condition: $\theta_c = 54.7°$. So when $\theta_c > 54.7°$, there will be no light trapping in general. Although there are always some light trapping happen because of the more complicated geometry relation around corner of each cube which we have to live with. Now that we understood the difference between 2D and 3D case for light trapping, we can go back to check the requirement for all light to be channeled along the right axes. By watching the equation (3.13), we can easily find that the only difference between the 2D and 3D version is the extra term $cos(\alpha)$ in the formula. Because $cos(\alpha) <= 1$, so it either keeps angle γ as the same in the 2D case which is when $\alpha = 45°$, or it increases the value of γ. That's why it causes some extra light trapping which does not exist in the 2D geometry. On the other hand, since it can only increase the value of the γ, it should have no effect on the requirement we got with the 2D version which keeps all the light channeling along the fixed axes because it cannot narrow the angle γ and cause extra transmission.

These computation shows that when we consider the material for ROL in 3D, it is more meaningful to have θ_c be a value between 45° and 54.7°. $\theta_c < 45°$ will just cause more light being trapped and $\theta_c > 54.7°$ will just have more light leakage during the light transportation without any other benefits. Although in reality, we have to live with the proper materials we can find with consideration of other aspects.

When we just consider the light channeling properties, too much light leakage will affect our 3D reconstruction of the event, however too much light being trapped will influence our energy resolution. The Current NuLat detector version has 125 solid scintillator cubes ($n_{scin} = 1.52$) separated by air ($n_{air} = 1$). These two materials make $\theta_c \cong 41°$, so there should be almost no light leakage under this condition. For the future of NuLat, we may also adopt another liquid version. This liquid version will use liquid scintillator (Ultima Gold AB) ($n_{scin} = 1.56$[49]) and use Teflon FEP films to form barrier and create the cells structure we need for ROL. With this condition, $\theta_c = 61°$, so there will be no light trapped under this condition but a lot more light leakage then the current version.
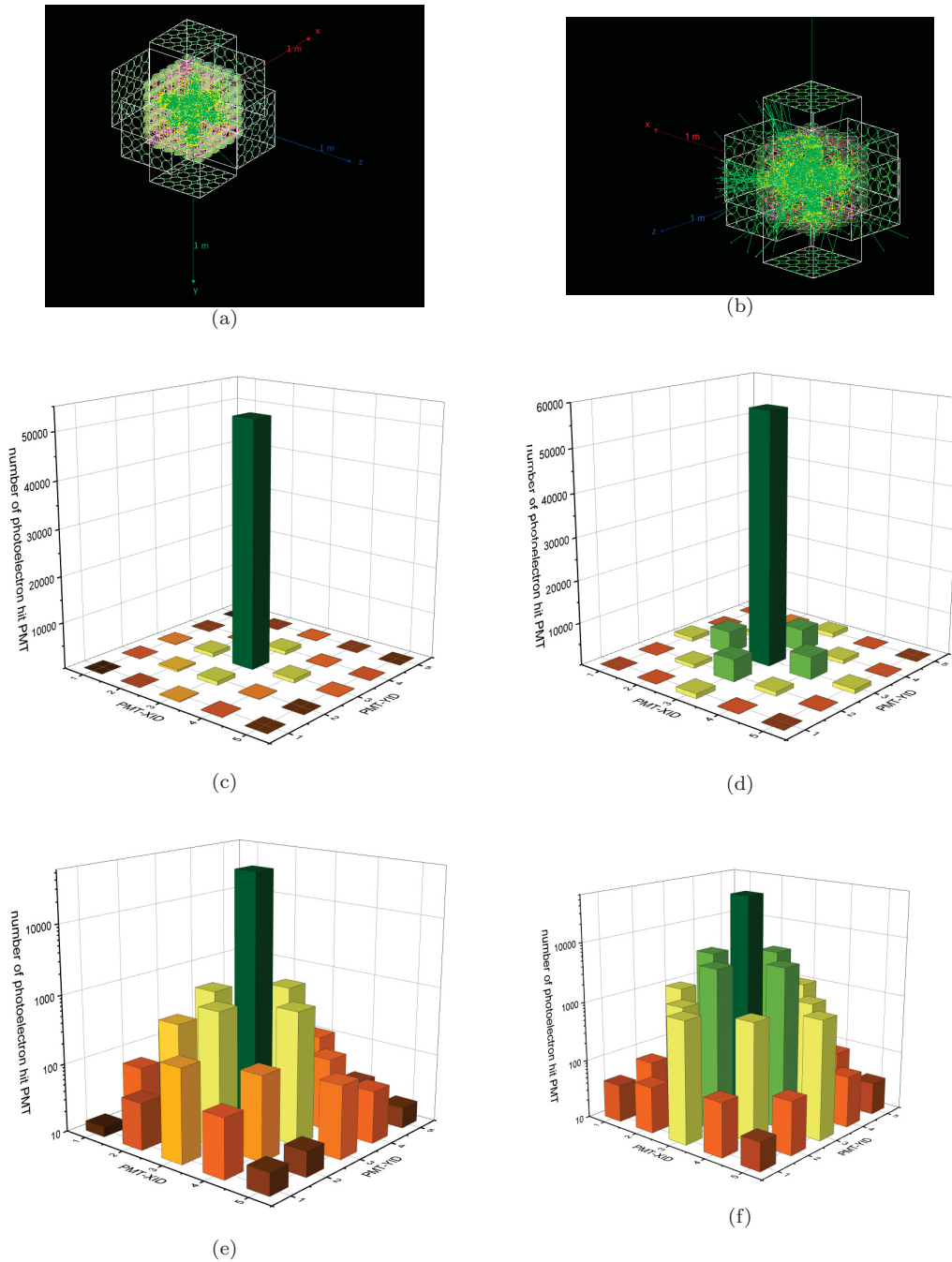
FIGURE 3.5: Demonstration of results from Geant4 simulation related to the light transportation property of current solid version and potential liquid version. Figure (a) and figure (b) are the graphs of Geant4 simulation of 3D light transmission with current solid and potential liquid version. Figure (c)-(f) are the graphs of PMT response to these two version with linear and log scale.

Figure 3.5 shows the Geant4 simulation result of the light transportation under these two conditions. This simulation has the geometry with the current $5 \times 5 \times 5$ version. It simulated the case when a positron deposited its energy at the center cube. The number of photoelectrons collected by 25 PMT on one face are mapped on linear and log scales. It shows clearly the difference in light transportation under these two conditions. Our current solid version shows very good light transmission along the axes as we think it should be. As expected, the liquid version might have 10% more cross talk on the neighboring cubes as this simulation shows. However with this amount of cross talk, our 3D geometrical reconstruction should still be valid.

Another factor we need to consider for the process of the light transportation is Fresnel reflection. Eq (3.15)-(3.17) are the Fresnel equations for polarized light.

$$R_s = \left[\frac{n_1 cos\theta_i - n_2\sqrt{1 - (\frac{n_1}{n_2}sin\theta_i)^2}}{n_1 cos\theta_i + n_2\sqrt{1 - (\frac{n_1}{n_2}sin\theta_i)^2}} \right]^2 \quad , \tag{3.15}$$

$$R_p = \left[\frac{n_1\sqrt{1 - (\frac{n_1}{n_2}sin\theta_i)^2} - n_2 cos\theta_i}{n_1\sqrt{1 - (\frac{n_1}{n_2}sin\theta_i)^2} + n_2 cos\theta_i} \right]^2 \quad , \tag{3.16}$$

$$R = \left[\frac{n_1 - n_2}{n_1 + n_2} \right]^2 \quad . \tag{3.17}$$

These equations Eq (3.15)-(3.16) are the Fresnel reflection coefficient for s-polarized and p-polarized light. Equation (3.17) shows the Fresnel reflection rate for perpendicularly incident light. These equations show that there will be more Fresnel reflection when the index of refraction of the gaps decreases. More Fresnel reflection in the process means more pulse time dispersion and worse timing resolution of the signal. There will be a potential benefit if we can get good timing resolution from signals. For example, if we have good timing resolution, we may be able to define the signal not just by which cell it comes from, but by geometrically which part of the cell it comes from. The simulation result in figure 3.5 shows that although liquid version has more cross talk, the position resolution is still adequate. With consideration of Fresnel reflection, it should also provide better timing information than the solid version.

3.1.3 NuLat Sensitivity to Light Sterile Neutrino Oscillation

In the last section, we introduced what kind of features a ROL based detector has. In this section, we introduce some prediction about the sensitivity of the NuLat detector to search regime for active to sterile neutrino oscillation signals. This summary draws on work by Dr. Zachary W. Yokley with the sensitivity code provided by Professor Patrick Huber and the explanation of the simulation works and results are quoted from Zach's dissertation (Ref[22]: pp 124-131).

Recall that the formula to explain the 3+1 model of active to sterile neutrino oscillation introduced in previous chapter is:

$$P_{ee}^{SBL} = 1 - sin^2 2\theta_{14} sin^2(\frac{\Delta m_{41}^2 L}{4E}) . \tag{3.18}$$

There are two parameters, mixing angle θ_{14} and squared mass splitting Δm^2 needed to well determine this oscillation phenomenon. Recall the discussion we have in chapter 2, where better determination of the mixing angle parameter requires better statistics. This means that any factors can affect the reactor to generate neutrinos, any factors affect the detector's detection efficiency and also the distance between detector and reactor are all the factors important to the sensitivity to this value. In specific, the power and duty cycle of the reactor, the mass of the reactor, the signal-background ration and total live time of the detector are all important.

The squared mass splitting parameter, as we discussed before, requires a good understanding of the E/L parameters. Since the energy spectrum of neutrino is set already by the fuel composition of the reactor, so the E value is already preset and we just take the value as given. Then the major factor we need to take care of is the understanding of the baseline value L. As we just discussed above, larger reactor can offer more neutrinos, in another word, can offer better statistics. Also, larger reactor core size can increase the ranges of baselines being sampled. However, there is also negative side of large core size reactor which is the increasing of the spectral uncertainty. Since it is difficult to determine where the neutrinos are exactly generated in the detector, large core size of the reactor can easily washout the spectral distortions. So we actually want to find a small research reactor for our sterile neutrino oscillation search.

One of the reactors we find appropriate for our purpose is the National Bureau of Standards Reactor (NBSR) at the National Institute of Standard and Technologies (NIST)
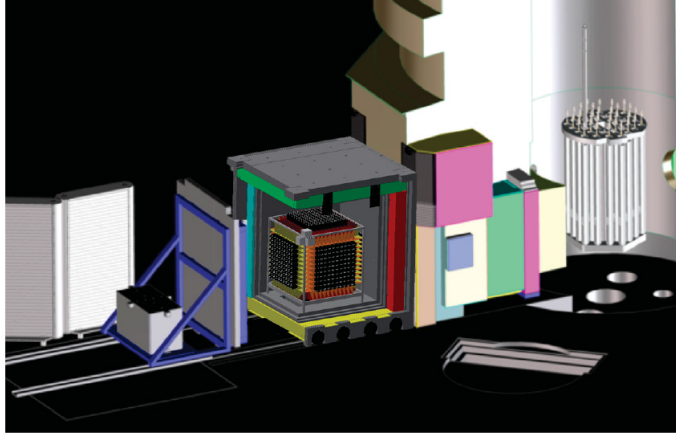
FIGURE 3.6: A CAD drawing of the 10×10 NuLat in the miniTimeCube (mTC) Shielding cave deployed beside the NBSR.

in Gaithersburg, MD. Figure 3.6 shows a CAD drawing of the potential location NuLat might take besides the NBSR. Figure 3.7 is a simulation result of what a $10 \times 10 \times 10$ NuLat detector can get besides NBSR based on the current best fit of $sin^2 2\theta$ and Δm^2. It clear shows that if such oscillations exist, the NuLat detector should have a convincing detection outside NBSR.
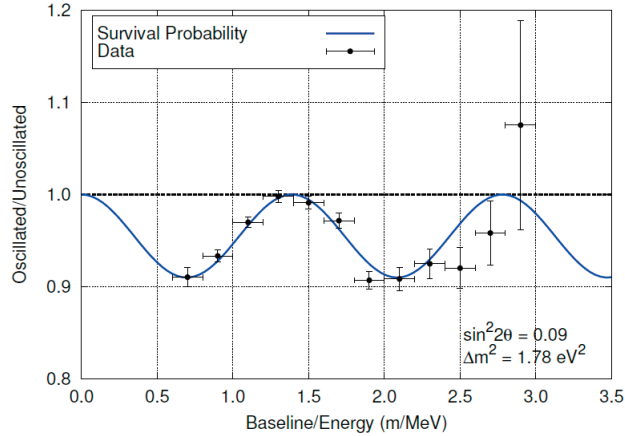
FIGURE 3.7: A possible result of an idealized NuLat detector ($10 \times 10 \times 10$) with the existence of a sterile neutrino with oscillation parameters of $sin^2 2\theta = 0.09$ and $\Delta m^2 = 1.78 \ eV^2$. Blue line is from formula (3.18) with these parameters and dashed black line give the null hypothesis-no oscillation.

To determine the sensitivity of NuLat besides NBSR, we use a likelihood function which in our case is actually a χ^2 statistic analysis with a raster scan process mainly discussed in Ref[50]. The χ^2 is from the comparison of the simulated result in which there are no active-to-sterile oscillations and backgrounds to the expected spectrum given by some

value in the parameter space (also including backgrounds). To be specific, χ^2 is defined as

$$\chi^2 = \sum_{i,j} \frac{((\alpha + \alpha_E^i)N_{ij} + \alpha_b B_{ij} - M_{ij})^2}{N_{ij} + B_{ij}} + (\frac{\alpha_b}{\sigma_b}) + \sum_i (\frac{\alpha_E^i}{\sigma_E^i}) \ , \qquad (3.19)$$

where N_{ij} is the number of neutrino events without oscillation in energy bin i and spatial bin j. B_{ij} is the expected number of background events, and M_{ij} is the expected number of events with oscillations and backgrounds. The nuisance parameters α, α_b and the α_E^i allow the normalization of the signal, background and the spectral bins to fluctuate. For α_b and the α_E^i, the fluctuations are limited by the value of σ_b and σ_E^i respectively. There is no corresponding limit on α, which indicates a free-floating normalization on the expected signal. This definition is similar to the χ^2 used in Ref[51].

With this definition of χ^2, we first find the best fit value of $sin^2 2\theta$ at a set Δm^2. With the value of χ^2_{min} determined, we can calculated the the value of $\Delta\chi^2 = \chi^2(sin^2 2\theta, \Delta m^2) - \chi^2_{min}$ for all values of $sin^2 2\theta$. The value of $\Delta\chi^2$ helps us to define the allowed region and excluded region in the parameter space. It is done with the help of $\Delta\chi^2_c$ which in two degrees of freedom is defined as

$$\Delta\chi^2_c = -2ln(1 - \alpha_{CL}) \ , \qquad (3.20)$$

where α_{CL} is the confidence level. In the parameter space, the region where $\Delta\chi^2 < \Delta\chi^2_c$ is the region accepted in this confidence level. On the other hand, the region where $\Delta\chi^2 > \Delta\chi^2_c$ is the region excluded by this confidence level. In our analysis, we present the result of 3σ exclusion curves. In this case, $\alpha_{CL} = 0.9973$ and $\Delta\chi^2 = 11.829$[52].

> A quote from Zach's thesis[22]: "For the specific calculation, we approximated the fission distribution of the NBSR with a uniform cylinder 1m in height and diameter. We also assumed a detection efficiency of 0.7 and a signal-to-background ratio of 5. The background shape was assumed to have a spectral shape that goes as $1/E^2$ with a relative uncertainty of 1%. The running plan was set that $10 \times 10 \times 10$ detector placed at two distances, 4.7 m and 6.7 m from the NBSR. Data taking should last for 1.5 and 2.0 years of live time at each distance respectively. The neutrino spectrum for ^{235}U was taken from Ref[53]. The IBD cross section was taken from Ref[54]."
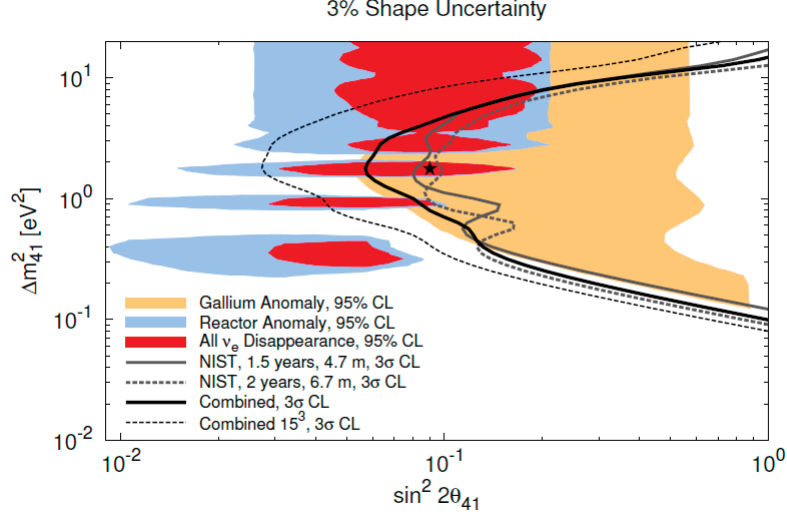
FIGURE 3.8: The sensitivity curves for NuLat's deployment at NIST. The shaded regions are the areas of the parameter space that are allowed at the 95% CL [21]. The best fit oscillation parameters is denoted with the black star. Note that NuLat can exclude this point at $> 3\sigma$ by using the data at the two deployment distances. The upgrade to the $15 \times 15 \times 15$ NuLat detector significantly increases the sensitivity to small mixing angles. [22]

Figure 3.8 shows the expected sensitivity of NuLat assuming a 3% shape uncertainty in the input neutrino spectrum. From this figure, we can see that NuLat has good reach into the allowed regions indicated by the electron antineutrino disappearance measurements and excludes the current best fit (denoted by the black star) at greater then 3σ when the results from 4.7 m and 6.7 m are combined. Result from $15 \times 15 \times 15$ detector is also shown in this figure.

Figure 3.9 shows another calculation with the spectral uncertainty as 7%. This figure shows that although the sensitivity curves at two different distances become worse than the result from 3% uncertainty, the combined sensitivity curve is relatively unaffected. It actually shows the benefit of NuLat detector as a compact movable detector because the ability of taking data at various baseline can help to cancel the effect of the spectral uncertainty from the source.

3.1.4 Current version of NuLat detector

In the previous section, we discussed a potential plan to detect antineutrinos from the NBSR with different baselines. In this section, we introduce the current version of the NuLat detector. This is a smaller version compared to what we just introduced in the
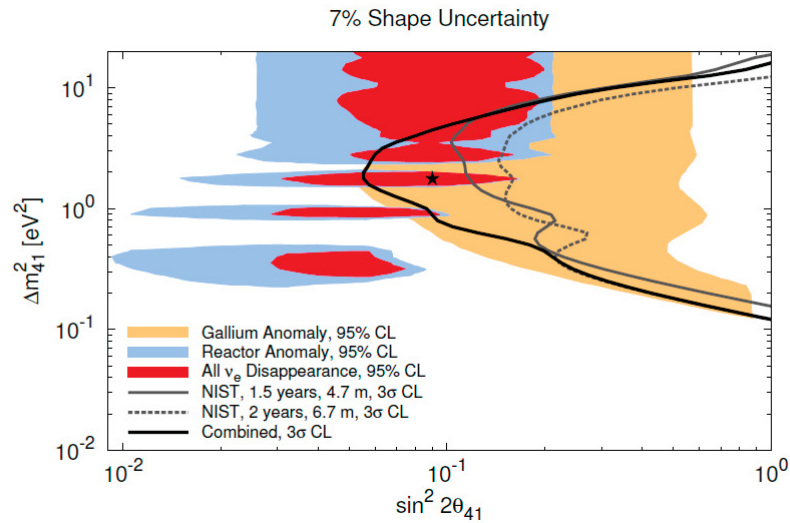
FIGURE 3.9: The sensitivity curves for the $10 \times 10 \times 10$ NuLat detector with a spectral uncertainty of 7%. All other parameters are the same as Fig. 3.8. Note that while the curves for the individual distances are worse than the ones shown in Fig. 3.8, the combined results is largely unaffected by the change.[22] The allowed regions were taken from Ref[21].
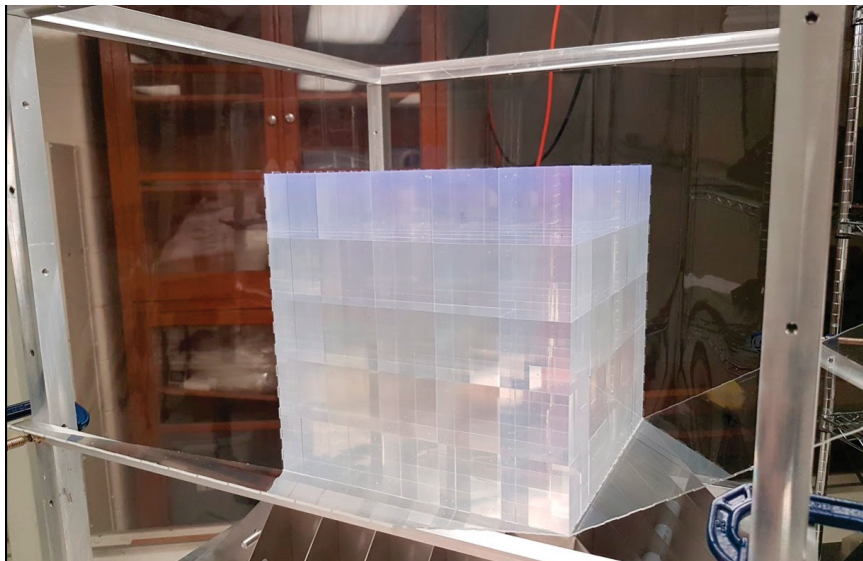
FIGURE 3.10: This picture was taken after all thes cube are assembled properly, sealed in a acrylic box made from six pre-cut acrylic plates. This version of the NuLat detector includes 125 solid cubic scintillators. 27 ^{6}Li loaded cubes are mounted in the center of the detector, surrounded by unloaded cubes to form a $5 \times 5 \times 5$ geometry.

previous section which only has 125 cubes to form a $5 \times 5 \times 5$ structure. This version is mainly for verifying the important design properties of ROL-based detectors. Figure 3.10 shows the major scintillator part of it. All the cubes are 2.5 inch plastic scintillator cubes. Twenty seven ^{6}Li loaded cubes with a $3 \times 3 \times 3$ structure surrounded by unloaded cubes forms a $5 \times 5 \times 5$ geometry. There is a thin air gap between cubes created by a spacer we made deliberately. The details of the spacer will be explained in the next chapter. With this configuration, we have the cubic cells and an air gap we need to make a ROL based detector as explained before.

As mentioned in the previous section, the common way to detect anti-electron neutrinos created during the fission process is the Inverse Beta Decay (IBD) process. Positrons created by IBD reactions carry most of the kinetic energy of the incoming neutrino and neutrons created simultaneously receive most of the momentum. Most of the time, the positron should deposit all of its kinetic energy into one cube. After that, the positron rapidly annihilates with an electron at rest, forming two back-to-back 511 keV gamma rays. In large volume detector such as KamLAND or Borexino, the energy of these two gamma rays will fully deposit to the detector, so it is not difficult to subtract it from the measured energy to accurately deduce the energy of the positron. However for small volume detectors, only a fraction of energy from these gamma rays will be deposited, which will add extra uncertainties to the deduced neutrino energy. At this point, the segmentation ability of NuLat becomes valuable. Since NuLat can reconstruct the geometry information, the energy deposition of these 2 gamma rays into other cubes that are not the cube catching the positron deposition can be rejected directly. This means NuLat can successfully separate the positron and annihilation radiation and avoid this problem.

After a positron deposits energy to the detector, a neutron created by the IBD reaction is detected by capture on ^6Li.

$$^6Li + n \longrightarrow ^7Li^* \longrightarrow \alpha + ^3H + 4.8 \ MeV \ . \tag{3.21}$$
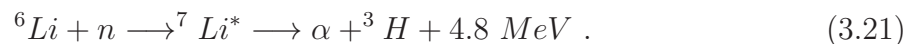
The 4.8 MeV Q-value will end up appearing around 346 KeV (electron equivalent) due to the quenching processes. Current ^6Li loading (0.5% by weight) offers $\sim 7 \ \mu s$ neutron capture time, which give the detector a good ability to reject backgrounds compared to other IBD based detectors. Also, the neutron capture distance based on this loading ratio is $\sim 6 \ cm$, making the neutron capture process happen either in the same cube where IBD

reaction happens or its neighboring cell. It offers another way to reject the background by this geometric structure.
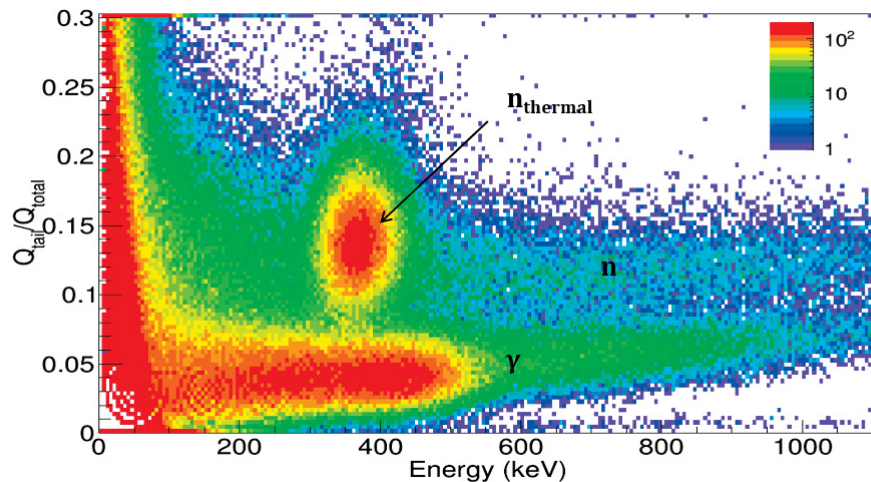
FIGURE 3.11: Test of pulse shape discrimination (PSD) with small scintillator sample, it clearly shows the separation of signals between neutron capture and gammas.

Besides the temporal and spatial coincidence, the scintillator in NuLat also has an inherent pulse shape discrimination (PSD) ability to distinguish signals from heavy particles like neutron to light particles like gamma. Figure 3.11 shows a PSD test we did with a small scintillator sample from the Eljen company. It clearly shows the separation of the neutron capture signal to the gamma signal. So this ability offers another aspect to reject the background.

The PMT the NuLat detector currently is the R10533 by Hamamatsu. The radius of photo cathode of this kind PMTs is 1.811" (4.6 cm)[55]. To maximize the light collection during the detection process, light guides are coupled to the PMTs to collect most of the photons from the square shape of each cell to the circular photo cathode surface. A similar simulation process as explained before was done to understand the relationship between the length of the light guide and the ability of collecting photons. The simulation is set to be under the condition of a $15 \times 15 \times 15$ NuLat detector and 100 MeV is deposited into the center cell. Different lengths of light guides were tested with the same simulation condition. The result is shown in figure 3.12. It shows that when the length of light guide is longer than 5 cm, there is very little increase in light collection.

The design of the light guides is also a balancing act. To keep the detector as compact as possible, it is better if we can have shorter light guides. However better light collecting is
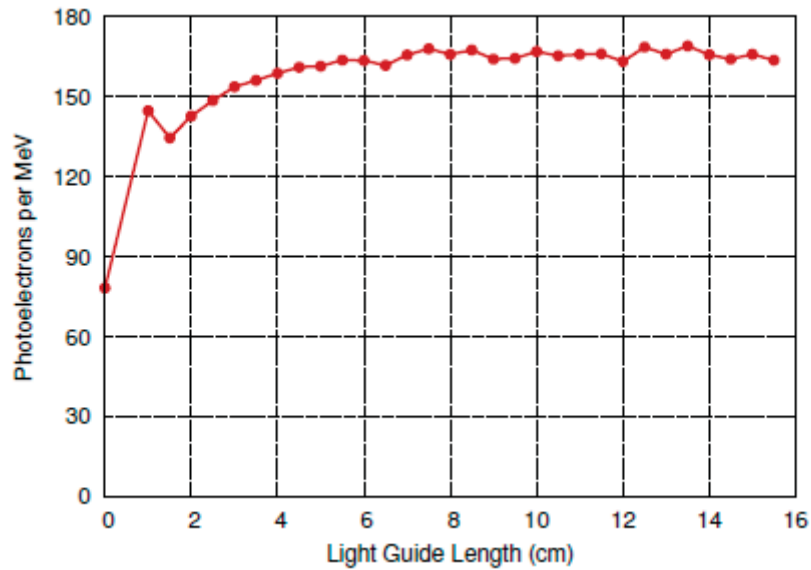
FIGURE 3.12: The guide length simulation results. Note that once a light guide reaches a length of $\sim 5cm$ there is little to no gain in increasing the length.[22]

crucial to better energy resolution. Figure 3.13 and 3.14 show two versions of light guides we designed with these concerns. We are currently using the version of the light guide with longer length to get better light collection.

3.2   mTC DAQ

The DAQ system that the NuLat detector is using currently is inherited from the miniTime-Cube (mTC) detector and some introductory material in this section is quoted from Ref[23].

The mTC detector is also designed as a compact neutrino detector to do measurements of reactor antineutrinos and it is as figure 3.15 shows.

A quote from mTC invited paper[23]: "The core detection volume of the mTC is a $(13 \text{ cm})^3$ cube of plastic scintillator (EJ-254), doped with 1% natural boron[56]. A total of 24 PLANACON MCP-PMTs (PHOTONIS XP85012) are used to detect photons from the scintillator. The anode plane of each MCP is segmented into 64 pixels, leading to a total of 1536 readout channels."

FIGURE 3.13: The CAD drawing for the old light guide design.
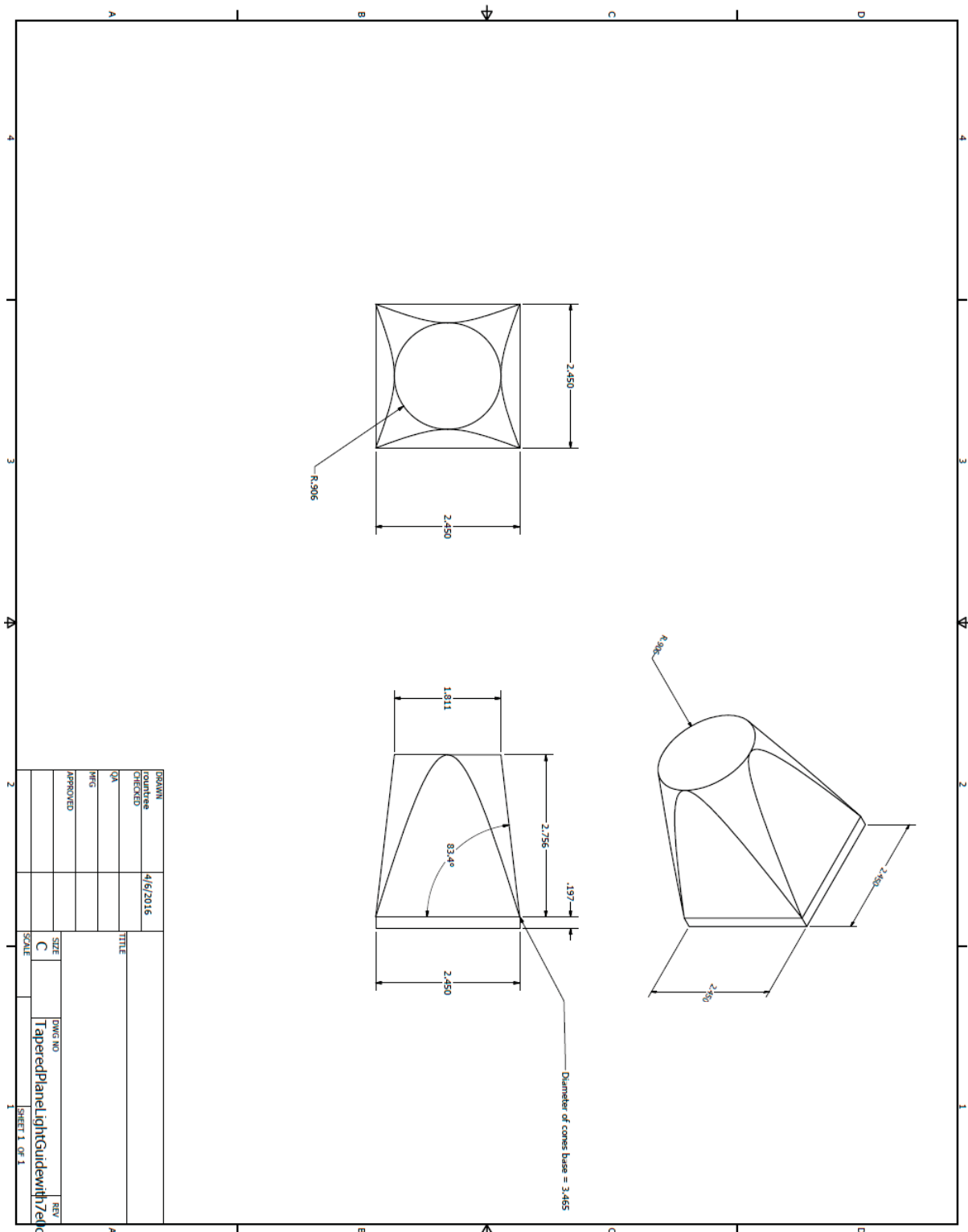
FIGURE 3.14: The CAD drawing for the current light guide design.
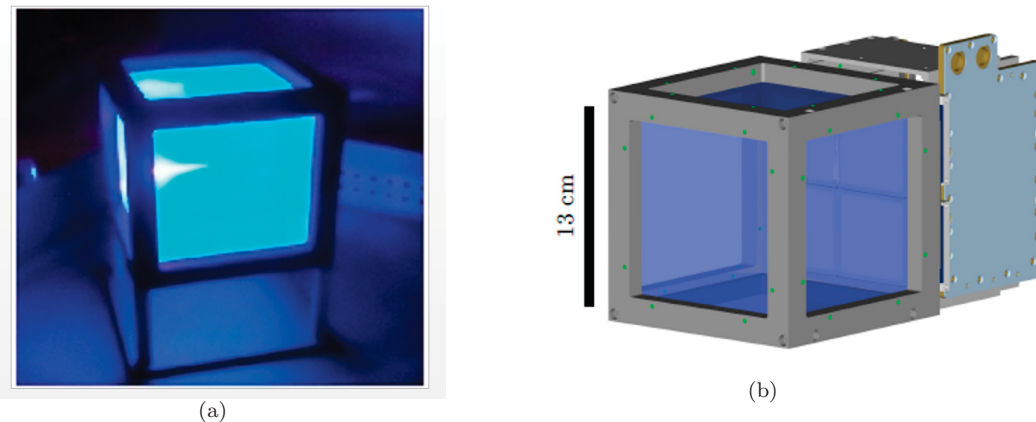
FIGURE 3.15: Figure (a) is the picture of 2.2 liter EJ-254 scintillator with laser pointer. Figure (b) is the CAD drawing of the mTC scintillator cube with one face populated with four MCPs and two electronics board stacks connected.[23]

All these readout channels are instrumented with custom electronics developed at the University of Hawaii which is exactly what currently being used by the NuLat detector. As figure 3.15 shows, the major difference between mTC and NuLat is that the core of mTC detector is one cubic scintillator, so the photons are spread isotropically everywhere and detected by 1536 PMTs around the detector. On the other hand, NuLat has a small barrier between each small cubic scintillator and the light channeling ability means the signal can be detected only by PMTs geometrically related to one specific cube.

The core of the electronics functionality is provided by the IRS[57], a family of application specific integrated circuits (ASICs) developed at the University of Hawaii. The IRS has been used in a variety of projects that require fast sampling and deep buffering.[58–60] The IRS ASIC architecture is shown schematically in figure 3.16. The core part of IRS is the 12-bit Wilkinson ADCs it included which offers high resolution transformation ability from analogy signals to digital signals which is also crucial to mTC and NuLat.

The IRS chips are mounted on the electronics board shown in figure 3.17 (a). The original mTC electronics module is as figure 3.17 (b) shows which includes 4 layers of carrier and one SCROD (Standard Control Readout and Data). Each SCROD contains a single FPGA (Xilinx SC6SLX150T). It works as the interface between electronics board and other control and data acquisition system. It mainly deals with the trigger control and clock signal sent from the CAJIPCI which will be discussed soon and makes all the boards connected to it responded properly to these signals. It also communicates with the back-end data acquisition system for register control and data transmission via fiber
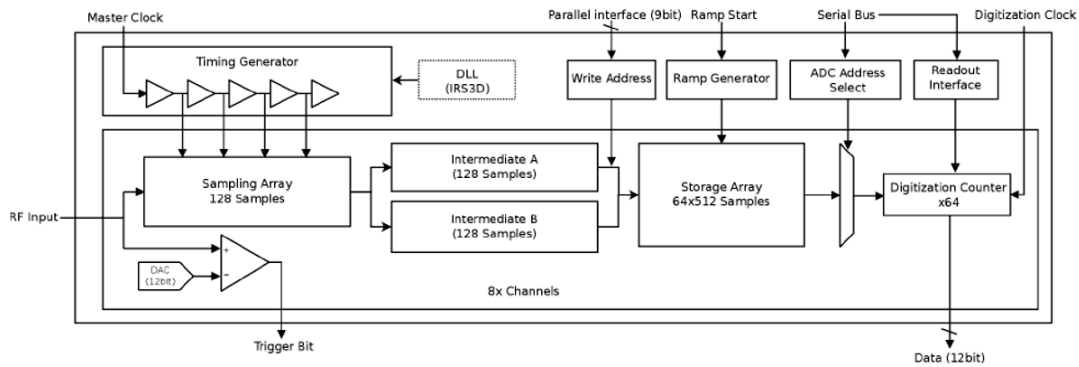
FIGURE 3.16: Block diagram of the IRS ASIC architecture. Eight channels of analog input are received by a set of eight sampling arrays, with sampling timing based on a common timing generator, driven by an external clock. This timing generator also determines timing of transfers from the sampling arrays to intermediate and storage arrays. The target location for the transfer from the intermediate to storage array is controlled by the user with a 9-bit parallel bus. A separate pin is used to start an internal voltage ramp, used to digitize 64-samples of the storage array for all eight channels in parallel. Selection of the storage address to digitize is controlled through a serial interface. A clock for the Wilkinson digitization process is generated internally (IRS3B) or provided externally (IRS3D). Once data is digitized, the channel and sample to readout are controlled by a second independent serial interface. Digitized data is available on a parallel 12-bit bus. A number of DACs and internal timing parameters are controlled by a third serial register interface.[23]
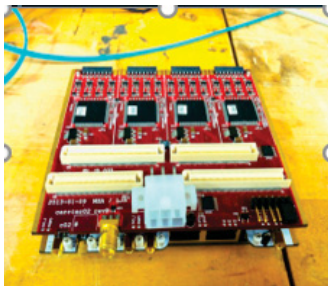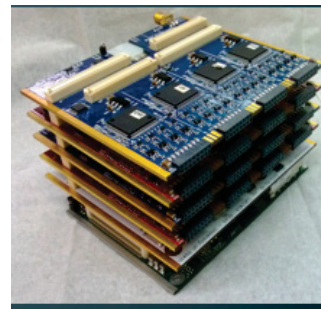
FIGURE 3.17: Figure (a) is a picture of one board of mTC electronics. Figure (b) is a picture of four boards mounted together with a SCROD.

optic cable. Currently, NuLat detector is running with 3 SCRODs and each SCROD has 2 layers of this kind of carrier. The detailed reasons will be discussed in a future chapter.

(a)

(b)
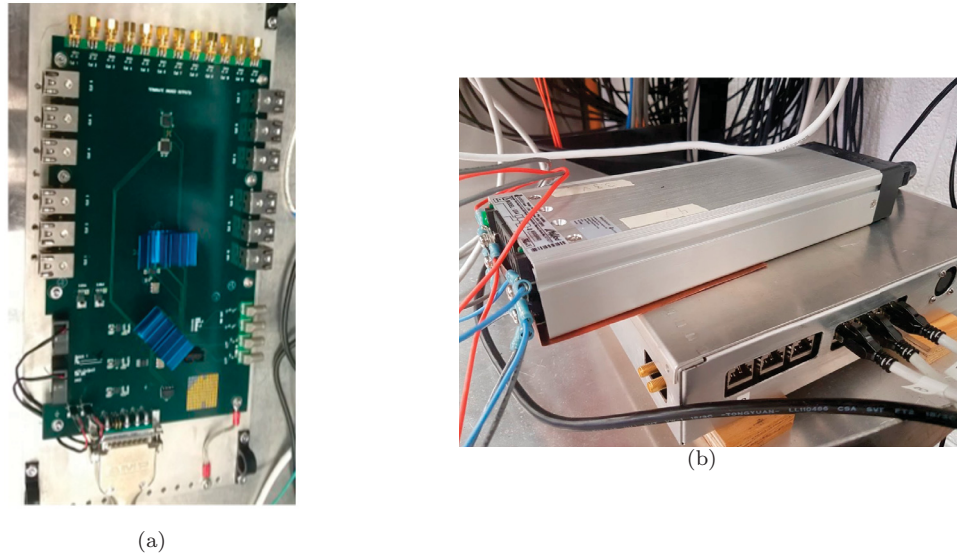
FIGURE 3.18: Figure (a) is a picture of one board of CAJIPCI. Figure (b) is a picture of CAJIPCI with 3 ARJ45 connected to different SCRODs.

All board stacks communicate with a custom PCB, designated Clock and JTAG in PCI (CAJIPCI), over differential pairs of CAT7a cable. The CAJIPCI board is shown in figure 3.18.

A quote from mTC invited paper[23]: "It provides a low jitter ($\sigma_t < 2\ ps$) clock to the front-end modules. Front-end board stacks provide a module-level trigger to the CAJIPCI over another differential pair on the same cable, and the CAJIPCI responds with a system level trigger over a third pair. The final differential pair can be used to perform flow control and limit trigger rates to the front-end electronics."

Current parameters set on front-end and back-end are listed as figure 3.19 shows.

Figure 3.20 shows a current version of trigger mode set on firmware that works on SCROD and CAJIPCI to make them working together issuing the trigger we need. First, there is level zero (L0) threshold set on each channel in a SCROD, using a DAC which is then fed into a comparator as figure 3.16 shows. This threshold will be compared to the actual signal directly from PMTs. Only when a signal from a PMT crosses this threshold with proper polarity will it fire a trigger bit. The SCROD will then add the total number

Parameter	IRS Range	mTC and NuLat Setting
Channels		8
Sampling cells		128
Storage depth		32,768
Analog bandwidth		>300 MHz
Digitization		On-chip Wilkinson
Quantization		12(9) bits logged(effective)
Dynamic range		~2V
Typical noise		~1 mV_{RMS}
Sampling rate	1-4 GSa/s	2.73 GSa/s
Master clock	8-31 MHz	21.3MHz
Buffer time	8-32 us	12 us
Conversion time	> 2us	6.2 us

FIGURE 3.19: Operating parameters for the IRS family of ASICs, and normal ASIC operating conditions for the mTC and NuLat.

of channels on itself and send this sum to the CAJIPCI. The CAJIPCI will get these numbers from all the SCRODs running with it and add them together again to get a number that shows how many channels are actually fire the L0 trigger during this clock cycle. Another level of threshold which relates to this number is set on the CAJIPCI. It will define whether this number falls into the range we require it to. If it fits the requirement, a new trigger will be fired.

If we set the trigger mode to be a simple trigger, then as long as the sum is between these levels, a true data acquisition trigger will be sent to the SCRODs to start digitizing data and send it to the computer. If we choose an AB trigger mode (neutrino trigger), then it will go through a different process. AB trigger requires both prompt signal (A) and delayed signal (B) pass these two thresholds discussed before, but there will be a temporal threshold to ensure that the time difference between A and B event falls into the range set on the CAJIPCI. Once the AB trigger is fired, the data acquisition process will digitize both A and B signals and send them to the computer. This trigger mode is crucial to IBD detection because IBD events are basically time coincidence events between a prompt and delayed signal. Figure 3.21 shows the diagram about how a simple and AB trigger works logically.

Figure 3.22 shows the screen shot of the software used to control the running of mTC

- **Upgraded system for complex (neutrino) triggering**:
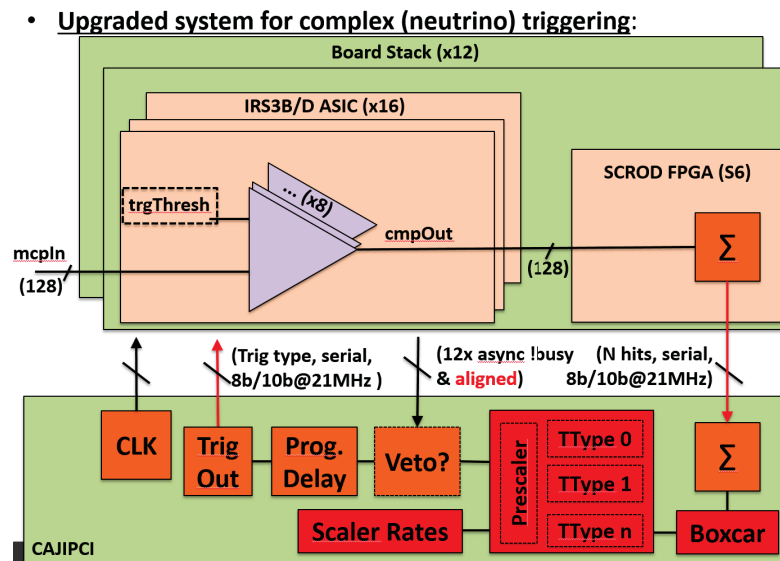
FIGURE 3.20: Current version of triggering system diagram between SCRODs and CAJIPCI.
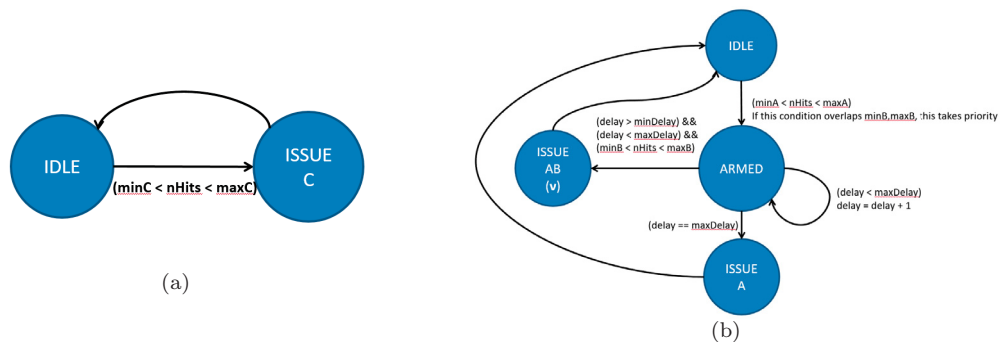
FIGURE 3.21: Figure (a) is diagram of the simple trigger mode. Figure (b) is diagram of the AB trigger mode.

electronics. The window at the right-top corner is the readout software running for monitoring the status of mTC electronics. It shows the active front-end modules, current trigger rate, the process of data taking and the current file recording the data. The right-bottom corner terminal shows the Python script running for adjusting the different level thresholds and doing other setting on the mTC electronics. The left-top corner shows a Gui-system which incorporates simplified functions run by the Python script mentioned previously. It helps the user to do simple adjustment of different threshold levels directly.

Each mTC front-end module needs 2 power supplies to offer 3.3 V with 4~5 A and 4 V with ~1 A. Figure 3.23 shows the power supply hardware the NuLat detector uses for these electronics.
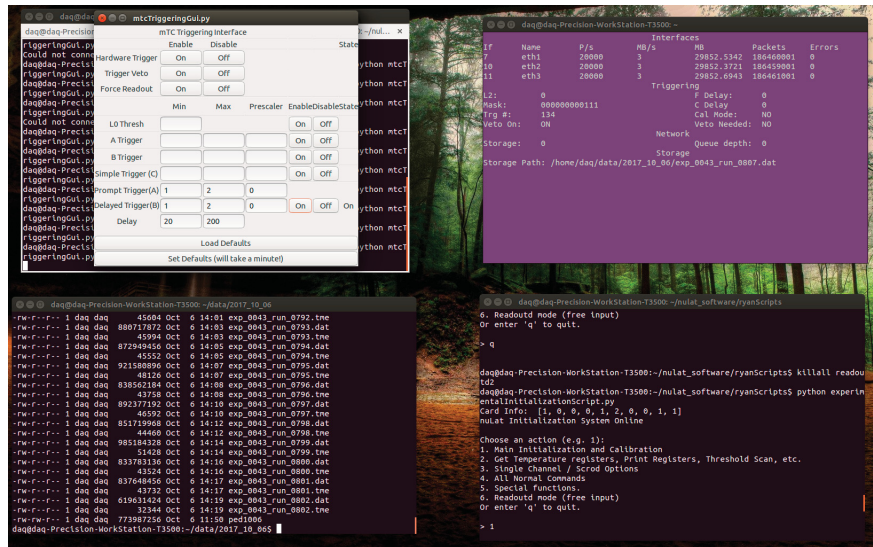
FIGURE 3.22: Screenshot of the software used to control mTC electronics.
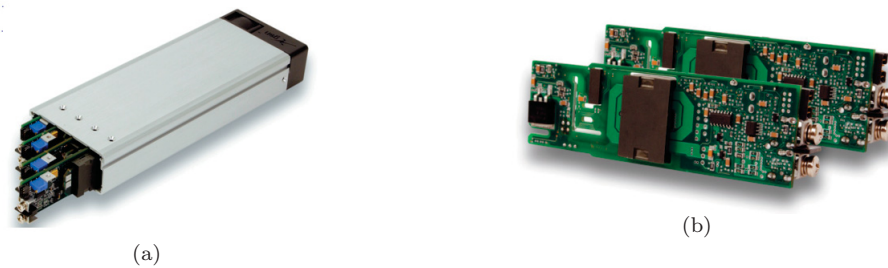
FIGURE 3.23: Figure (a) is a picture of Ux4 4 slots powerPacs. Figure (b) is a picture of UltiMod Series Power Supply board.

Chapter 4

NuLat Detector Construction
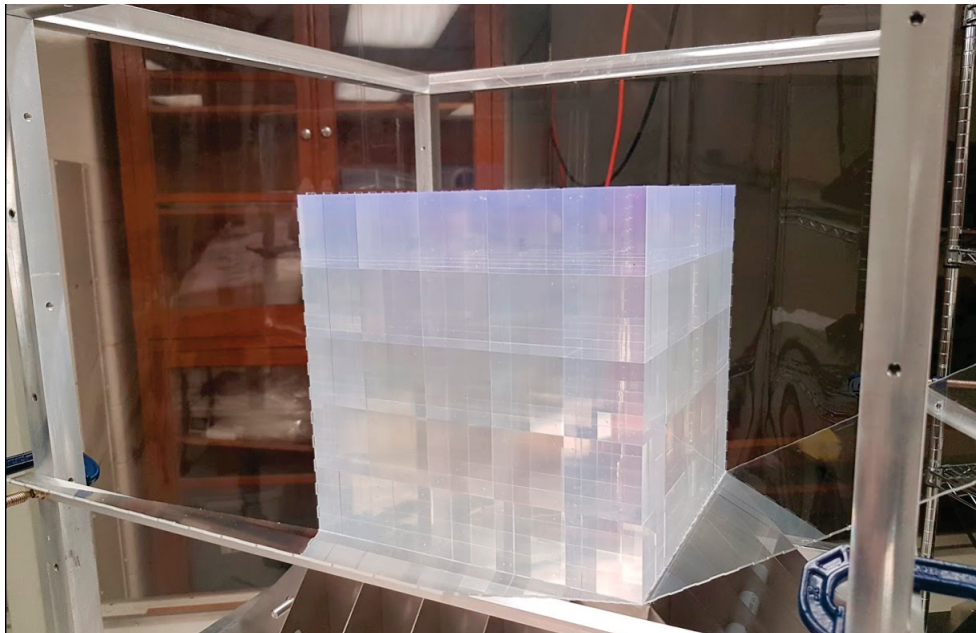
FIGURE 4.1: This picture was taken after all 125 cubes were mounted into the acrylic box.

In previous chapters, we discussed the physics behind neutrino oscillation and the NuLat detector. In this chapter, we introduce how to assemble the current NuLat detector with solid scintillator from Eljen. We need to make sure there are short gaps between each cubic scintillator so that there would be effective total internal reflection. Also PMTs and light guides need to be mounted at accurate positions. The coupling between PMT and light guide should be robust so there is no light reflection at that surface. They also need to be coupled strongly so they will stay in good condition during the assembly, testing and running.

4.1 NuLat Detector construction

The current NuLat Detector uses an acrylic box as the container to maintain cubic scintillators at the right place and protect them from damage. Also the acrylic box needs to have basic ability to hold gas without leaks, this requirement coming from our radon calibration test which will be explained later. The acrylic plates used to form a box are 1/16 inch thick. The edge of these plates were pre-cut to a stepped shape, as figure 4.2 (a) shows. These stepped edged are designed so that when we assemble two plates at 90°, they fit perfectly together. After all 6 plates are assembled nicely with the help of these steps, each edge is sealed by transparent plastic tape to avoid any potential gas leak from the edge. In practice, the assembly has to include an additional step so cubes can be properly mounted. The details will be explained later.

(a)

(b)
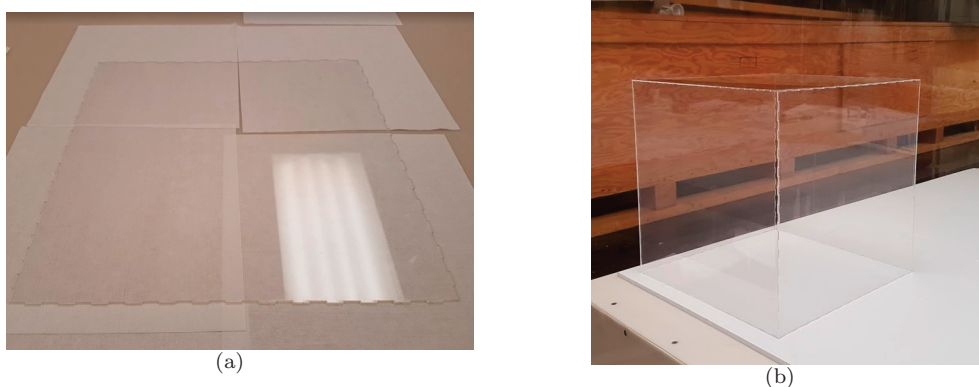
FIGURE 4.2: Figure (a) is the picture of pre-cut acrylic plate. Figure (b) is the acrylic box assembled by 6 pre-cut plates.

There is an extra step before all the scintillator cubes from Eljen can be mounted into the acrylic box. Some tiny dots made from vm-2000 reflective film have to be put carefully on the four corners of certain face of these cubes. This step is to make sure that when these cubes attach to each other, there will always be some of these dots between them so a thin layer of air gap can be created without changing the dimension of the design too much. This is exactly the gap to help our detector have a light channeling ability from total internal reflection between two different media. Figure 4.3 shows how these dots finally appear on the cubes.

We choose vm-2000 thin reflective film as the material of our spacer between cubes with the hope that photons which hit the dots can still be reflected and reach another PMT finally. To make these tiny dots efficiently, we first cut a big square sheet of vm-2000, put double sided tape on one side of it, then attached this side on a plastic working plate.
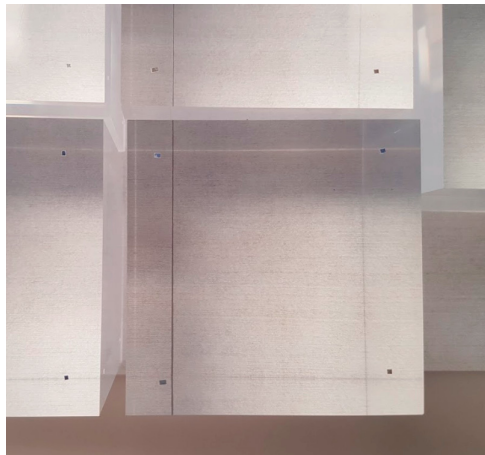
FIGURE 4.3: Picture of cubes with dots at four corners.

After this work, we used a razor blade with a ruler to cut a thin strip out of it. Figure 4.4 shows how this works in reality. We peel off this strip carefully to make sure the double sided tape is still attach to this thin film. This strip can be used to cut dots later on our preset frame.
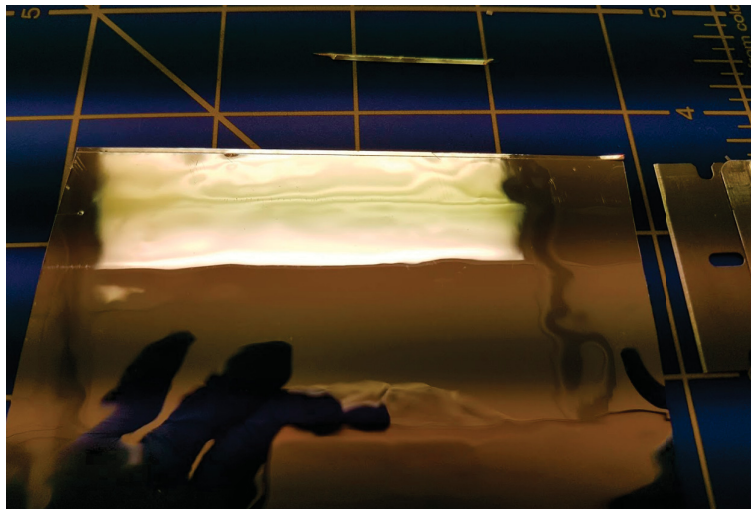
FIGURE 4.4: VM-2000 cutting exhibition. A VM-2000 sheet put on a flat working board, we use razor blade to cut thin layer out of it.

Next we cut strips of vm-2000 to small dots and put them on the cube. To make sure that the process is safe, so that there will be no damage to the (expensive) cubes and also to ensure that they are placed at roughly the right positions, we made a thin stainless steel shim as a safety mask. This shim is solid enough that sharp tools such as razor blades cannot go through easily and will not mark anything on the other side of the shim. We punched four holes at the right position of this shim so when it covered the cube, these four holes were just at the right position around the 4 corners of the cube. To make sure

when this mask cover the cube, everything is stable and will not move easily, we made an alignment equipment from PVC and tape the mask to it as figure 4.5 shows. This frame has a small concave shape just to fit a cube, so as long as the cube is pushed into this place, it should be at same position relative to the mask all the time.
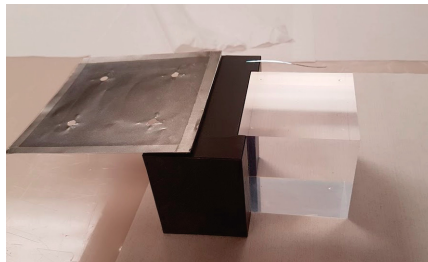
(a) Frame with cube and uncovered mask.

(b) Frame with cube and covered mask.

FIGURE 4.5: Picture of spacer mounting system.

With the help of the frame and mask we made, we worked on putting dots on the cubes properly. We first aligned the cube to our PVC frame and then cover it by the mask, then we attach one end of the strip through the hole we punched through the shim earlier to the cube. We used a razor blade to push back the end slightly so a small part of it attached to the cube relatively tighter than other part. Then we cut this small part off of the strip with the razor blade. During this time, the razor blade needs to be held vertically so that we can check the exact place it will cut. During these processes, with the help of the razor blade, we make sure the two ends of the razor blade are on the stainless steel shim to avoid leaving any scratches on the cube.

There is an easy way to check that these dots keep good space between different cubes. We can align several cubes vertically as figure 4.6 shows. Then we try to see from the top cube, if there is some sign of Newton rings, that would indicate little to no air gap between two faces of different cubes. As long as there are no Newton rings the space between different cubes is good enough for our total internal reflection requirement.

The number of dots needed on each cube are actually different. Most cubes just need 3 faces to have dots. However some cubes along sides, edges or corners need dots on 4, 5 or 6 faces. These requirements are easy to figure out by just thinking how to make sure the interface between two faces needs one layer of dots to separate them.

After all scintillator cubes have dots on the proper face, we started to mount the cubes into the acrylic box. At this point, there is some mixture of the order related to assembling the box, sealing the edges and mounting the cubes to make all these work easily.

FIGURE 4.6: Five cubes with dots being mounted vertically to check whether there is Newton rings when people looks from top.
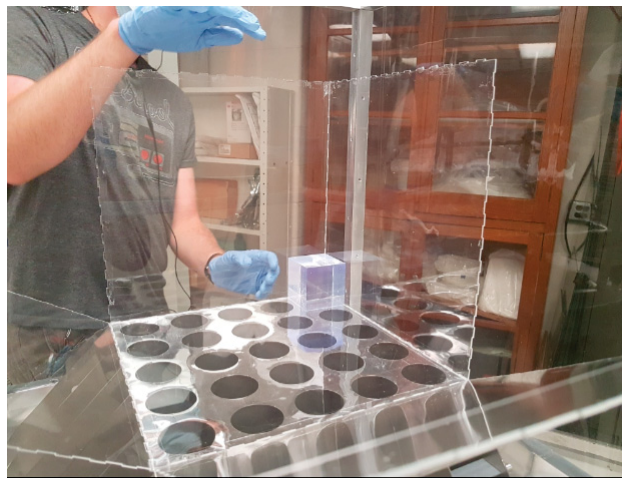
FIGURE 4.7: A prefixed acrylic box was put on the bottom grid for PMT, two sides of it were loosen and leaned against the bars fixed at proper place, a good opening was made for cube mounting purpose.

The first step is to assemble 5 pieces of acrylic plate together and leave the top side open. All the connected edges between two plates should be sealed with tape roughly, as there is no need to seal the edges perfectly at this step, they will have to be peeled off and resealed later. The reason will be explained soon. After assembly, this box will be placed on the frame of the NuLat detector. The frame is actually several aluminum bars will be used later to have side plate with PMTs on, the bottom of this frame already have the stainless steel grid for PMTs mouting in the future. The acrylic box should sit on this grid directly with a roughly centered position. The assembly of box here is just offer a relatively good reference for cubes mounting task.

Once we have the box on the right position, we peel off some tapes to loose two sides of the box from the side, so they just lean out with the bottom edge still attached to the box. We have bars across the frame of the detector to hold them at a proper position so there will not be too much pressure on the bottom edges of these two plates which are still taped to the bottom plate. It gives us a good opening for mounting the cubes. Figure 4.7 shows how it looks.

After this, we have a good reference and opening for mounting the cubes. We then mount cubes with the order from the deep corner of the opening, then layer by layer. We need to be careful to not leave any scratches on the cubes and also to make sure no dots fall down during assembly. That's why during the process, we try our best to put the cubes at the right position without sliding anything. The partial finished version of this task should looks like figure 4.1, shown at the beginning of this chapter.

After 5 layers of cubes were mounted properly, we then resealed the acrylic box with tape. We first put the two sides we has loosened before back to the right place. We also assembled the top plate which had not been touched since the beginning. At this step, we just taped all the edges to make sure they were relatively tightly connected.

Then we lifted this acrylic box so that it did not sit on the bottom grid, but instead has a small freedom to move. Also, it opened room for us to re-tape the bottom edge of the box. To do this lifting work, we made a support frame shown in figure 4.8. It was basically 25 PVC tubes glued to a PVC plate. 25 PVC tubes can go through the grid initially prepared for PMT mounting. This frame was put on a longer and wider wooden plate which then held by four big C clamps. These clamps caught the bottom of the wooden plate and aluminum framework of the detector. By adjusting the C clamps, we adjusted the distance between wooden plate and bottom of the NuLat detector. As long as the distance was short enough, 25 PVC tubes would hit against the bottom of

Figure 4.8: Homemade bottom support frame for acrylic box.

the acrylic box. From that position, when we reduced the distance more, this frame work would start lifting the acrylic box. Figure 4.9 shows how this lifting was done.
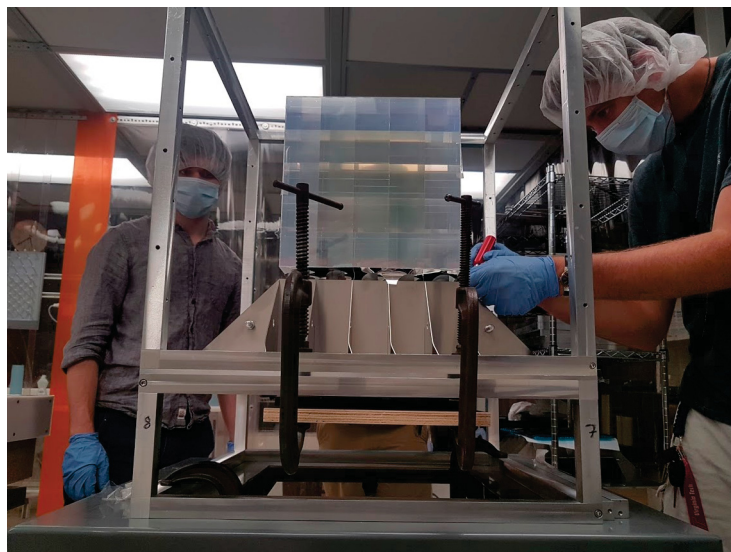
Figure 4.9: Acrylic box with fully mounted cube was lifted by support frame from bottom. One of colleagues was working on retape one of the bottom edge.

With the cube raised, we then peeled off the tape on one edge and re-taped it carefully. We used isopropanol to clean the surface before applying new tape. This was the final seal, so we needed to be careful to make sure the sealing was perfect to avoid potential

gas leakage from the edge of the box. It was difficult to prevent small leak channels at the edges with tape, even with careful overlaps. So when we cut tapes to do the sealing, we tried to cut them just the right length to reach the edge of the box. Thus each edge could be sealed by one tape, without overlaps at the corner. Also when the tape was pushed down, we used some flat and relatively rigid material (like a credit card) to press the edge, so there was no gas channel from the edge of the box to the edge of the tape. We kept doing this edge by edge until all the edges were finished. Figure 4.10 shows the process when we used a credit card to press the edges.

FIGURE 4.10: Picture of colleagues are working on retape the edge of acrylic box.

After all the edges have been sealed, we needed to add one extra layer at corners. This was an experience we obtained from a test we did with a small acrylic box as figure 4.11 shows. A small hole was drilled on one short square side of this acrylic box. Gas tubes blocked this hole with the other end connected to a hand vacuum pump. By pumping down the box, we checked how long this box would hold a relatively good vacuum. This test showed that corners were the major position for gas leaking. As long as we had an extra layer of the tape on the corners, the sample box had a lot better ability to maintain vacuum for a long time. So we cut a square shape of tape and added it to each corner to provide extra protection. The extra square shape tape on the corner is shown in figure 4.12. One thing to keep in mind during the process was that there were two corners which need openings for the nitrogen gas to go through. Details about the nitrogen gas and radon source filling process will be discussed in chapter 5.

Once all 8 corners had this extra layer of tape, we needed to test whether the box had the ability to hold gas. The test was similar to what we have done before on the small
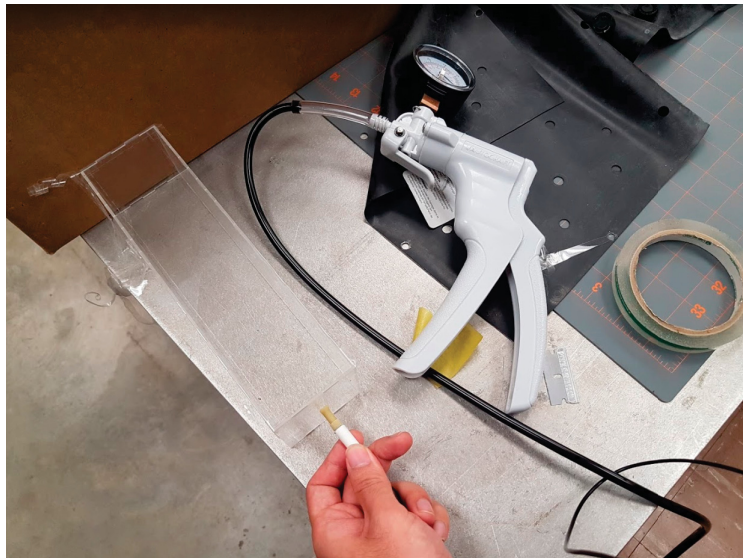
FIGURE 4.11: Picture of the process when we were testing gas leak condition on small acrylic box sample with hand vacuum pump.

sample box. Since there were holes on the top and bottom plate which were drilled for future radon filling purposes, we blocked one hole on the top with a gas tube connected to the hand pump, the other end of this tube was then blocked, the hold on the bottom was blocked just by finger. Since this was a larger box compared to the sample box, the vacuum status was not as good. However we were still be able to check the communication between these two holes using the phenomenon of Newton rings. As pumped, the lower pressure inside the box resulted in the acrylic plate being pushed by atmosphere and started to touch the surface of the cubes. The surface connecting between these two things created Newton rings. However, once we unblocked the bottom hole, the Newton rings disappeared immediately. This kind of quick disappearance showed that these two hole on top and bottom have very good gas communication.
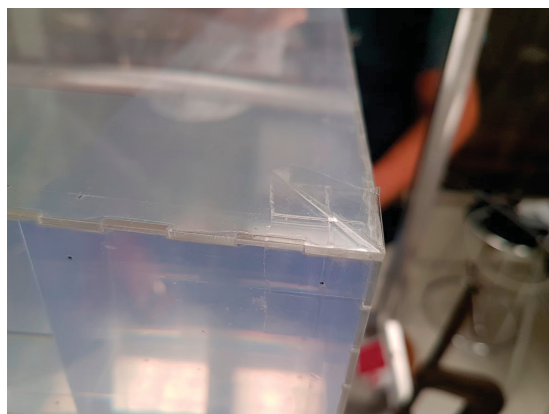
FIGURE 4.12: A square shape extra taped being tape on the corner of the acrylic box.

After the sealing and check works were done. we started to re-align the position of detector relative to the PMT grid at the bottom. We started this process by lowering the detector with the help of adjusting the C-clamps until there was only very small gap between the box and the PMT grid below. Each C-clamp needed to be kept at a relativity same extension during the process of lifting so the box was kept level. This adjustment was done several times patiently. The space between a bottom of the box and grid was as small as possible so it provided freedom to move the box but also gave us a good reference of the position between the box and the PMT grid. We then aligned the position of the acrylic box by slightly moving the wooden plate holding the support frame. As mentioned before, this process also needed extra patience. We verified the alignment of the acrylic box with the PMT grid by checking each edge while carefully watching and also with a finger touching as a secondary check. After these two checks showed all four edges have good alignment, we convinced ourselves that this box had been aligned good enough for our purpose.
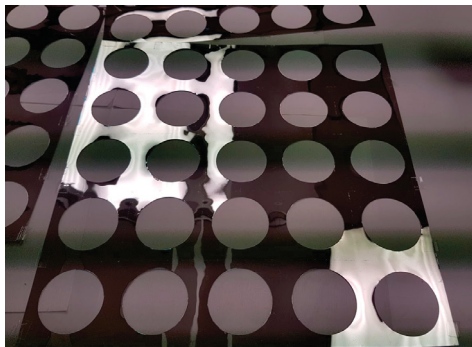
(a) Reflective sheet with holes cut for PMTs.
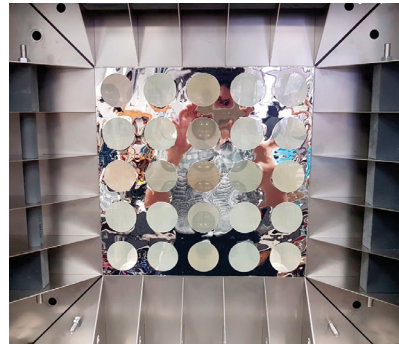
(b) Reflective sheet taped to the acrylic box with side mounted.

FIGURE 4.13: (a) shows the reflective sheet we made from vm-2000 film. It was cut to square shape with exactly same size as the side of the acrylic box. Holes were pre-cut for the PMT mounted later. (b) shows how it looks when the sheet was taped to the box and with several sides on.

During the actual test, we assembled the detector twice with different configuration. Since we only had 14 Li loaded cubes on hand during the first test, we had to use all of them and then put unloaded cubes to fill a $5 \times 5 \times 5$ geometry. After around one month of preliminary test, we received many more cubes from Eljen, so we disassembled the detector and repeated the assembly steps again with the current configuration which was $3 \times 3 \times 3$ Li loaded cubes in the center surrounded by unloaded cubes.

There was another item being changed between these two configurations: the reflective sheet setting. During the first assembly, we actually taped reflective sheets on the acrylic box after it was sealed. As figure 4.13 shows, there were holes pre-cut so PMTs can still

FIGURE 4.14: Picture of mirror we made to plug into the grid without PMT. It is made from a plastic square plate covered by a layer of vm-2000 sheet.

get the light signal it needs. For the places where there were no PMT, we made a square shape mirror plug as figure 4.14 shows. This plug can be pushed into the grid design for PMTs, the position is fixed by the two spring legs to create friction. The preliminary test after first assembly showed some signals which were geometrically not related, so during the second assembly, we decided to get rid of this kind reflective sheets.

(a)

(b)
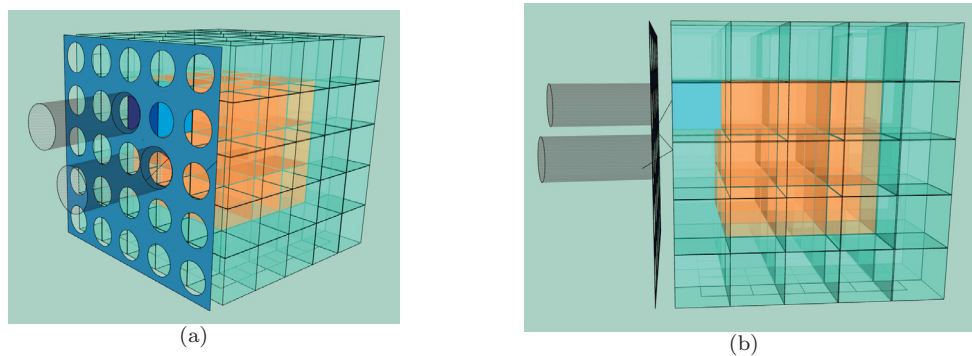
FIGURE 4.15: These two graph shows how the mirror sheet can cause geometrically unrelated cross talk which confused us for our event reconstruction. The cube marked blue in figure (a) is the cube we set as the exact light source from the real signal. The PMT facing this cube should receive the majority of the photons from this cube. However, there are some photons reflected by the sheet received by the PMT one layer below this PMT. The side view of this process is also shown in figure (b). Since this process is random, any PMTs at this side can receive such kind of signal confusing us when we try to do event reconstruction of the geometry.

There are several issues to be thought about related to this kind of mirror configuration. One of the potential reasons about why we got some events that are not geometrically related on three sides is that the photons reflected by the reflective sheets shown in figure

4.13 might not reflect back to the cube it initially come from. It perhaps was reflected by the output face of that cube and then hit the reflecting sheet again. The tricky part of the travel of this kind of photon is that during its travels, there are a lot of blank holes on the reflective sheet which have a PMT just right there, so during its travel, this kind of photons can be caught by any PMTs randomly which might be the real source of those events that confused us. This random process is explained by the figure 4.15.

Another thing about the mirror of concern is the comparison of the positive side of it to help more light collection and the negative side, where more cross talk might be introduced. A detailed test will be introduced in chapter 5, but a brief summary is that we get rid of the reflective sheet for the current version of the NuLat detector, but actually uses mirror plugs on the opposite side, where we have PMTs mounted, to help light collection. The result seems promising.

4.2   NuLat Detector PMT Mounting Method
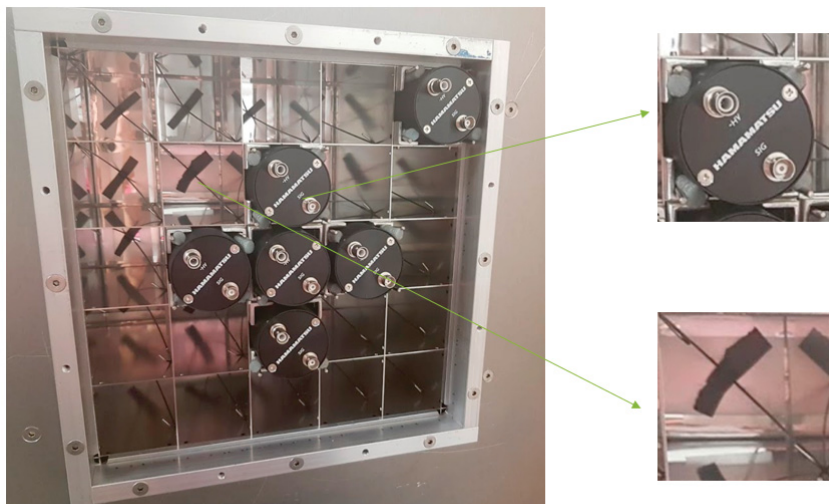
FIGURE 4.16: Picture of 6 PMTs being mounted on one side, square mirrors made by vm-2000 filled other empty places without PMTs.

In this section, we introduce several preparation steps for PMT mounting work. Figure 4.16 shows how it finally looks when PMTs were mounted into the grid. It also shows how the mirror plug looks when it is pushed into the square channel prepared for PMT and stays there stably.

In the current configuration we made a PMT mounting grid on each side, bolted to the side plate first. The benefit of this design is that PMTs on each side can be independent of the other sides. Once we need to do some modification on one side, we just need to unscrew that side and PMTs on this side can go along with this side plate without extra work. The major requirement of PMT mounting is fixing the PMTs at their right depth in the PMT grid, and coupling PMT to light guides tightly without air bubble.

4.2.1 Introduction Of $90°$ Angles And J-hooks Help PMTs Mounting
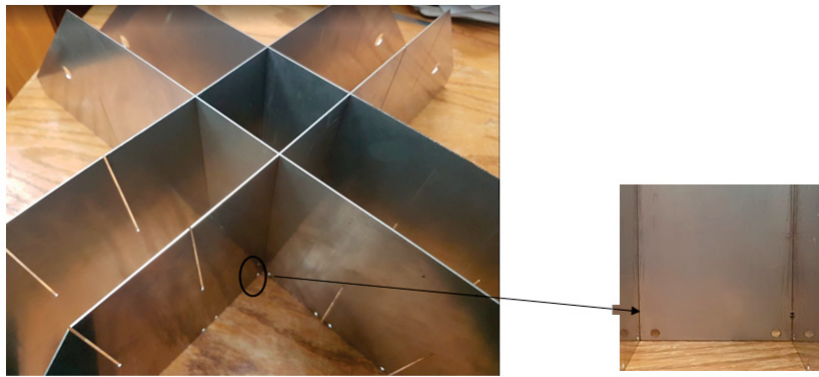
FIGURE 4.17: Holes on PMT grid used for fixing the position of PMT.

To meet the first requirement, we relied on the holes at the stainless steel plate of each PMT grid. The hole is shown in figure 4.17. We made $90°$ aluminum angles as an extra frame for our PMTs by taping them to the PMTs tightly. There was proper size of the gap pre-cut on these angles so that the stainless steel plate of the PMT grid and these angles can be connected by J-shape hooks we made specifically for this purpose. All these small parts are shown in figure 4.18 (a).

Figure 4.19 shows how all these parts are connected together and lock the position of PMTs. J-shape hooks go through the slot on the angles and holes on the PMT grid simultaneously to lock them together. Since the angles are already taped to the PMT tightly, the PMT then has a fixed position within the PMT grid. There are foam plugs we press into the gap between this J-hooks and the PMTs to make sure they will not fall out easily. This kind foam can be seen in figure 4.16 which is how everything looks when assembled.
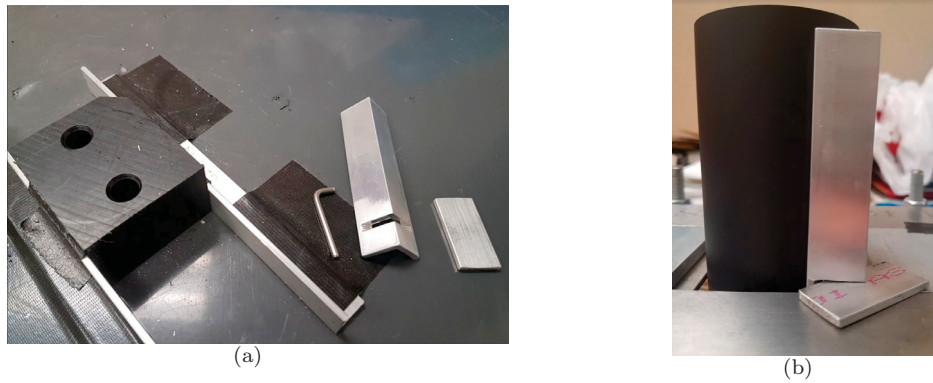
FIGURE 4.18: Details of angles and PMT assembly. Figure (a) shows different parts used for PMT mounting. Figure (b) shows angles with slot mounting framework.
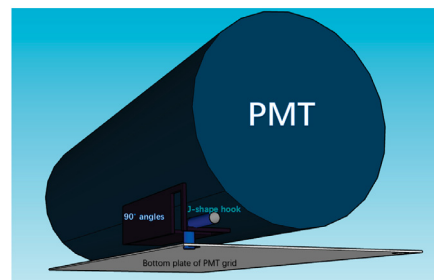
FIGURE 4.19: Idea of mounting PMT with 90° aluminum angles and J-shape hook on the PMT grid through holes.

Aligning the guide rails to the PMT housing needed to be very accurate. Since where the angles and slots relative to the PMT defines the position of PMTs within our detector, we needed to make sure all the angles were put on the PMTs at exactly correct place. Figure 4.20 shows an alignment platform we made to do quality control of the assembly of aluminum angles and PMTs.

Figure 4.18 (b) shows details of how this framework helped the assembly. A PMT is placed vertically by plugging in BNC and HV connectors into holes we pre-drilled into a PVC block, so when the PMT is put there, it has the same height relative to the base plate every time. As figure 4.18 (b) shows, slots on the 90° angles are plugged by a small aluminum alignment plate, the rest of this plate leans against the frame. With this design, every time the 90° angles align like this, the height of this angle would only be defined by the frame. As long as we adjust the height of frame properly, angles would have the right position relative to the PMTs. The height of the frame can be adjusted easily by the nuts on the threaded rods at four corners of the frame. These four threaded
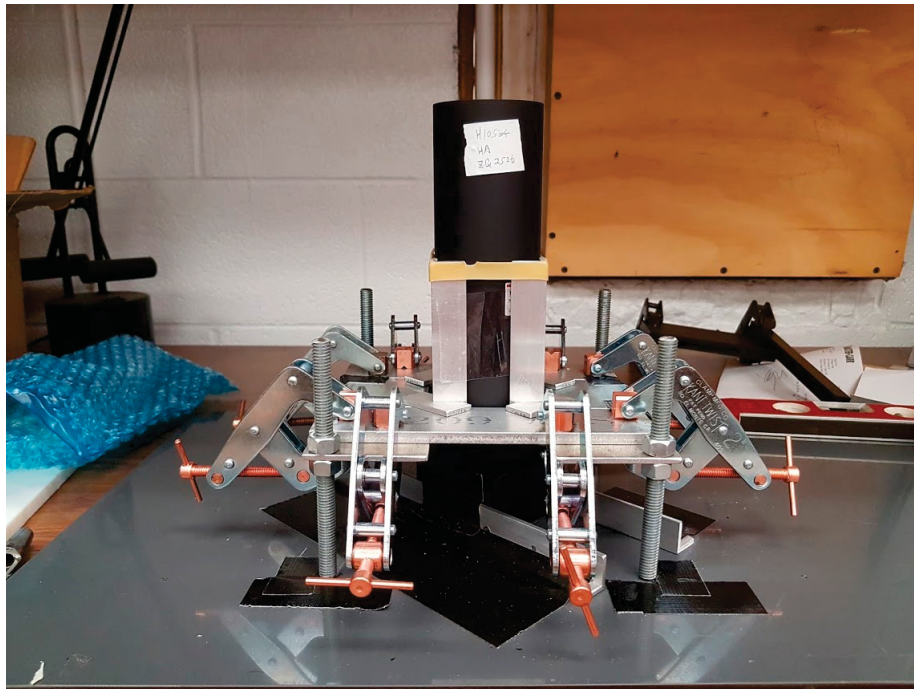
FIGURE 4.20: Picture of frame we made for accurate assembly of angles and PMTs.

rods were treated as four legs for this frame.The J-shape hook is made by cutting 1/8 " rod to around 1 3/4" long, then 1/2" of it is bent 90°.

Since we currently only have 25 light guides, there are two different structures of PMT and angle assembly. One was made for 50 PMTs which would be mounted without light guides. The height of the frame was measured to make sure that when PMTs mounted into the grid with a J-hook, the front end of PMT would be flush with the front end of the grid. The other structure was made for 25 PMTs with light guides, it was measured to make sure that once one end of the light guide coupled to a PMT nicely, the other end is flush with the PMT grid when it is mounted there. After several tries and measurements, these two dimensions were measured and PMTs were being mounted accurately.

4.2.2 Assembly of PMTs and Light Guide

Figure 4.21 shows a nice example of assembly of a PMT with a light guide. This assembly has two requirements. One is to make sure the PMT and light guide are aligned perfectly, a slight off-center can be a big problem when they are finally plugged into the PMT grid. The other is that the optical coupling between light guides and PMTs should be good so there will be no light reflection at the connection.

FIGURE 4.21: Picture of one PMT pre-taped with 90° angles coupled with light guide tightly.

FIGURE 4.22: Frame made to align PMT with light guide during the coupling of these two parts.

Figure 4.22 shows a frame we made for the alignment requirement. PMTs with angles should slide in from the top, the square tube from top was made so angles pre-mounted onto the PMT fit snugly. When a PMT slides down, it can thus be straight. Light guides should be put on the bottom with one edge fit into the concave gap made by two angles. The dimension of this gap was also designed to fix the position of the light guide. With these two features, light guides and PMTs can be assembled with good alignment.

The PMT manufacturer suggested that we use silicone grease to maintain good optical coupling for the connection. So we used silicone grease, as shown in figure 4.23. There

FIGURE 4.23: These two pictures show the optical interface pads and the silicone crease we use for the connection between the PMTs and the light guides.

were also optical interface pads between PMTs and light guides. We first put a small drop of silicone grease on the light guide, spread it uniformly and then put an interface pad on it. We did same thing on the PMT, first spread grease and then assembled the PMT and light guide together using the frame just explained.
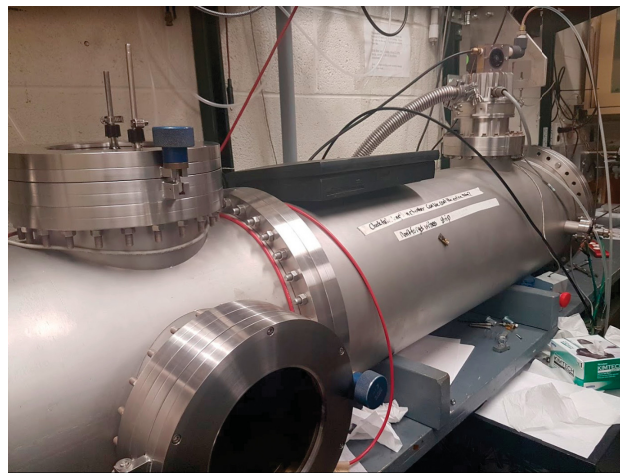
FIGURE 4.24: Vacuum-chamber used to get rid of air bubble at the junction of PMT and light guide.

After assembly work was done, we put the whole piece into a vacuum chamber shown in figure 4.24. We pumped down the chamber using a scroll pump to 1 torr and then left the whole piece under this vacuum condition overnight. It helped to get rid of the air bubbles which might still be in the connection.

These steps helped to get rid of the air bubbles and maintain good optical connection between PMTs and light guides. However there were still some imperfection for the

connection, as some small air bubbles were difficult to get rid of. So the assembly work still needs some improvement in the future.

FIGURE 4.25: Exhibition of fully mounted PMTs. (a) is picture of 25 PMTs fully mounted on one face. (b) is picture of PMT on one side with rubber sheet covered and cable connected.

After all the PMTs went through the preparation steps introduced above, they were mounted properly to the detector frame with J-shape hooker. To keep the light sealed out of the detector, we used a rubber sheet to cover all the PMTs which is shown in figure 4.25. There are holes pre-cut in the rubber sheet so the BNC and HV connectors can pass through. These sheets were taped to the frame by black tape. To check the light leak condition of the detector, we slightly turned on a PMT and check the signal coming out from this PMT. By comparing the signals with room light turned on or not, if there is no difference between these two conditions, this means the light seal is good enough for our purpose. Once we verify there is no light leak, the assembly of the NuLat detector is finished.

The connection between PMTs on the detector and MTC Daqs is shown in figure 4.26. Three sides of PMTs are connected to 3 different SCRODs. Cables are labeled by three different colors to avoid confusion of the connectors. The side noted as the blue side is where PMTs on this side have light guides connected. One of the benefit of connecting PMTs from different sides to different SCROD independently is that it included the first order geometry information directly by different SCRODs, so for the firmware design in the future to reconstruct geometry information on hardware, the design can be a lot easier.
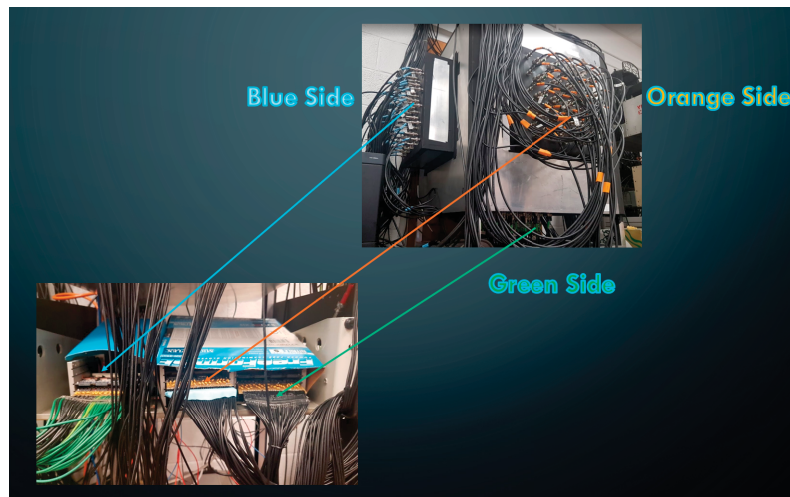
FIGURE 4.26: Current connection between 3 PMTs and 3 SCRODs.

Chapter 5

Preliminary Hardware test

In this chapter, we describe several hardware tests we performed before taking data with the NuLat detector. There are two aspects to try and understand via these tests. The first is light transmission properties of scintillator cubes, such as loss per cube and potential signal cross talk. The second is a test of the mTC DAQ system. It gives us a basic understanding of limitation of the mTC DAQ.

5.1 Light Transmission Test

(a)   (b)
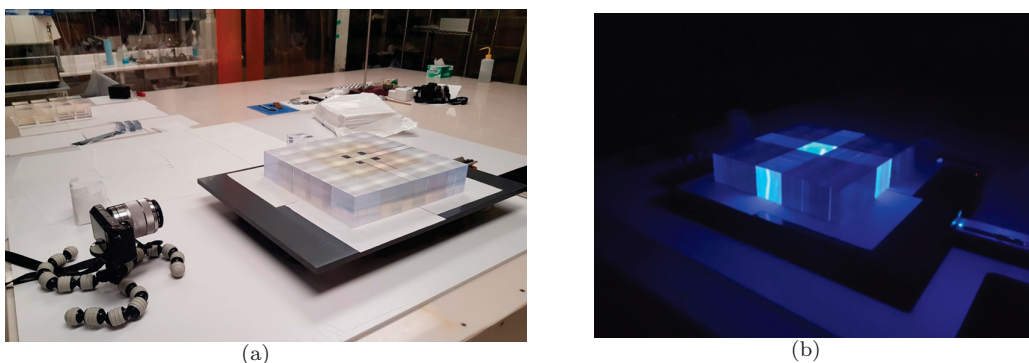
FIGURE 5.1: Exhibition of light channeling hardware into configuration. A laser beam is fed underneath the PVC plate at a 90° angle. There is a 45° mirror underneath the middle cube. This mirror reflects the laser beam vertically up , making it go through the middle cube. This configuration make the middle cube our light source. Figure (b) shows how the light channeling looks with this configuration.

The light transmission properties of our scintillator are very important for the NuLat detector. As a ROL based detector, good light channeling ability and energy resolution are

the advantages of this design. To get results similar to those of theoretical computations, we must ensure that light loss during transmission and cross talk between neighboring cubes is low.

Since we only have 75 PMTs fully running now, only three diagonal faces have PMTs mounted taking 3D information. This means some signals at certain cubes has to go through four extra cubes to reach the PMTs. Also for one of the potential version in the future, NuLat will have $15 \times 15 \times 15$ cubes with PMTs fully mounted on all six sides. The signal from the center cube would then have to go through 6 extra cubes to reach the PMTs. So we clearly need to understand how much light loss there will be when it go through several extra cubes.

A major advantage of the NuLat detector is the ROL structure which gives us full 3D information of each event because of total internal reflection. So each cube needs to have low cross talk with its neighbors, otherwise the result will have confusing geometrical information and will be difficult to analyze.

5.1.0.1   Light Transmission Test with ^{6}Li Loaded And Unloaded Cubes
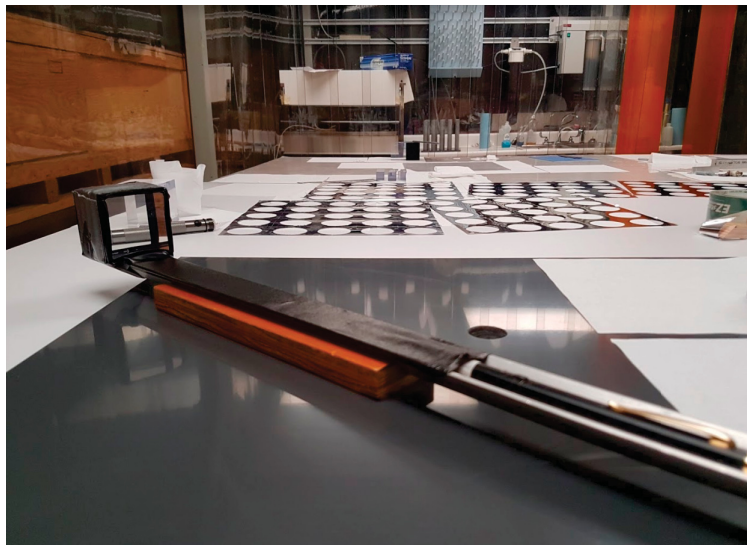
FIGURE 5.2: The cube surrounded by vm-2000 taped on the 90° angles, laser pen is put along with this angles so the laser path can be pre-defined.

The first step of our light transmission test is to make a diffusive light source which can mimic the realistic condition when particles deposit energy into one cube. Figure 5.2 shows how one of the diffusive light sources we made looks. Four sides of one unloaded cube are warped by vm-2000 reflective film and tightly taped. The bottom side film has

a hole which leaves a space for laser light go through. A 45° diffusive reflective film is underneath this hole. These parts are taped tightly on a 90° angle for alignment. Then we feed a laser pointer along the support angle iron. The laser beam should be automatically aligned. When the light feeds in, the reflection from the mirror surrounding it makes it a diffusive light source with two sides open for light to come out.
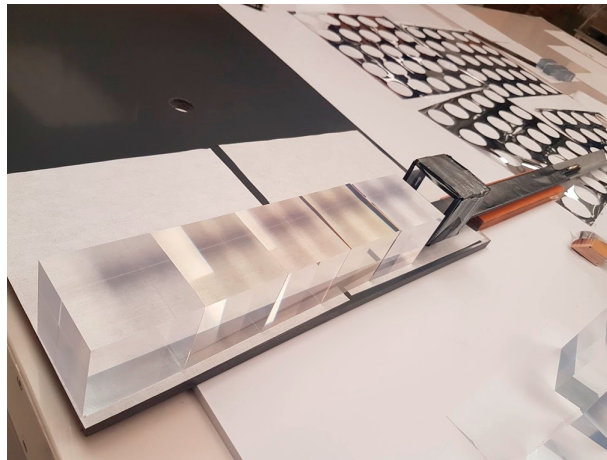
FIGURE 5.3: Example of the light transmission test. It has five cubes aligned together with 3 Li-Loaded cubes in the middle, our homemade light source is located after that.

To understand the light transmission information, we used a camera as our preliminary test detector. The camera we use is a Sony-Nex-5R. We disabled all the automatic adjustments this camera has which might confuse us later. The general geometry is shown in figure 5.3. We put different numbers of cubes in front of our light source, with the camera focused on the face of the last cube from the light source along the same direction. As previous sections already explained, we currently have a $3 \times 3 \times 3$ ^6Li loaded cube in the center of the detector, surrounded by unloaded cubes to form a $5 \times 5 \times 5$ geometry, so when we do this light transmission test, we also adopt this geometry structure as shown in figure 5.4. Yellowish cubes represent cubes having ^6Li loaded and the solid blue cube represents the light source. The experiment was done in a dark environment, so camera should only receive light information from the cube.

After collecting picture data, we analyzed the results by counting the RGB value from the RAW format file of the pictures we took. The general idea is shown in figure 5.5. The center of the graph has a blue square, where light generated by the light source which passed through cubes was centered and caught by the camera. We choose a very small square—300×300 pixels to avoid edge effects, then we added the RGB values independently of this area. As example of figure 5.5, R and G values were around 0 since the light source is from a blue laser. So the B value was the major concern. We used blue
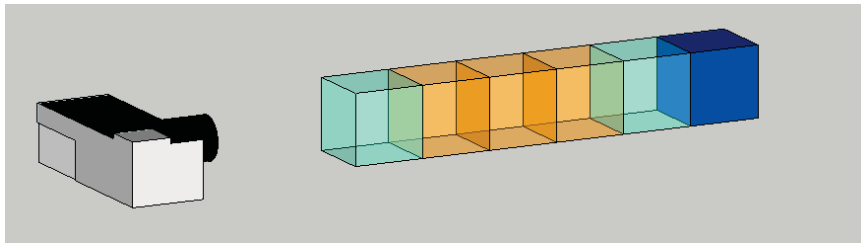
FIGURE 5.4: Sketch of the camera, cubes and light source for the light transmission test.

laser for this test is mainly because the wavelength of the emission from the scintillator we adopted is from 400-500 nm[56], which is the wavelength of the violet and blue light.
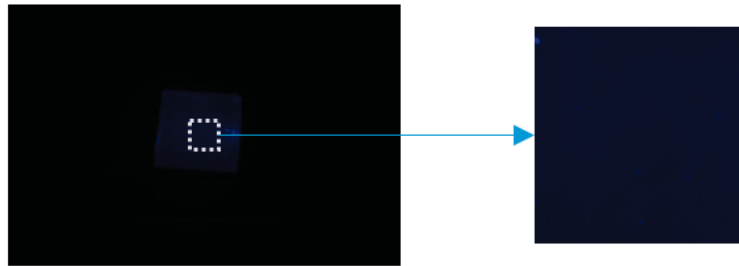
FIGURE 5.5: Example of the data analysis from RAW format picture.The camera was setted for f/4, ISO 800 for 1/50 sec.

Figure 5.6 shows the result of tests we did with unloaded cubes. The picture was taken from the light source directly, then one cube in front of the light source, the one more and finally we had 3 cubes in front of the light source. Different total B values from these 4 different configurations are histogramed in figure 5.6 and their values are labeled on top of each histogram. These value shows that there is around 13% light loss when light passes through one unloaded cube.

Figure 5.7 shows the result of the test we did with just Li loaded cubes. The process is the same as we did for unloaded cubes. The result from figure 5.7 shows that there is around 17%-23% light loss when light passes through one Li loaded cube.

Figure 5.8 shows the result of the test we did with the same configuration of current detector, 3 Li loaded cubes were at the center and one unloaded cube at each side. The process of data taking was the same as explained before. The result is consistent with the other two tests with purely unloaded and loaded cubes. All three tests generally showed that the signal we may get will be around 10%-20% weaker when it goes through one more cube.
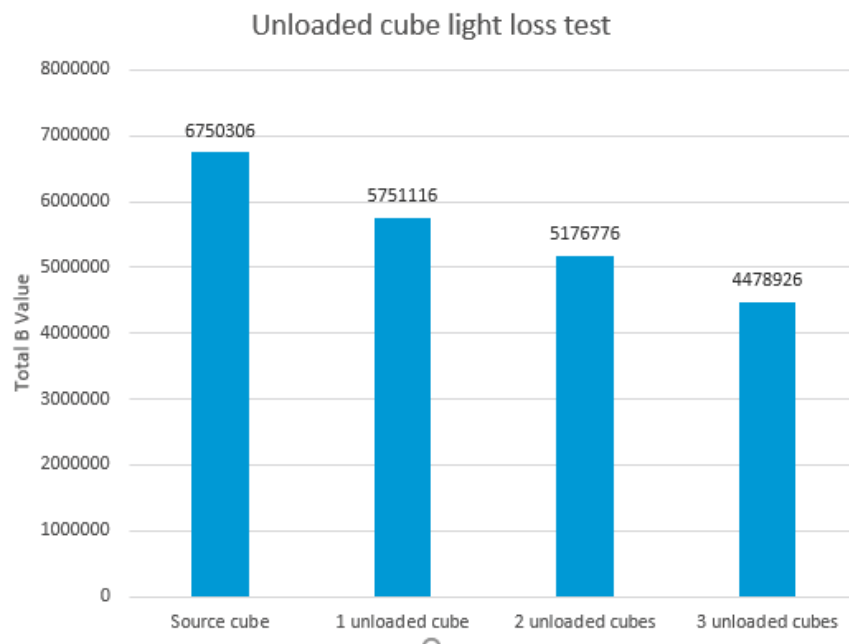
FIGURE 5.6: Data analysis result from light transmission test for unloaded scintillator.
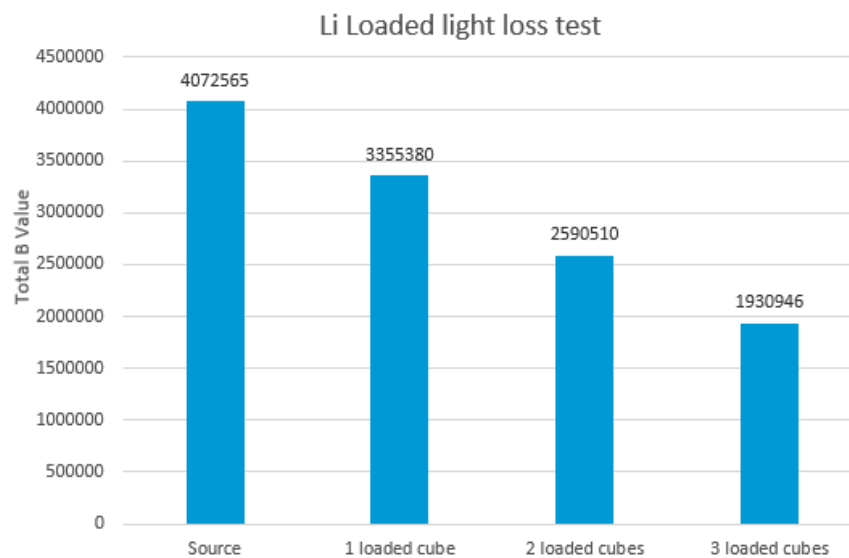
FIGURE 5.7: Data analysis result from light transmission test for loaded scintillator.
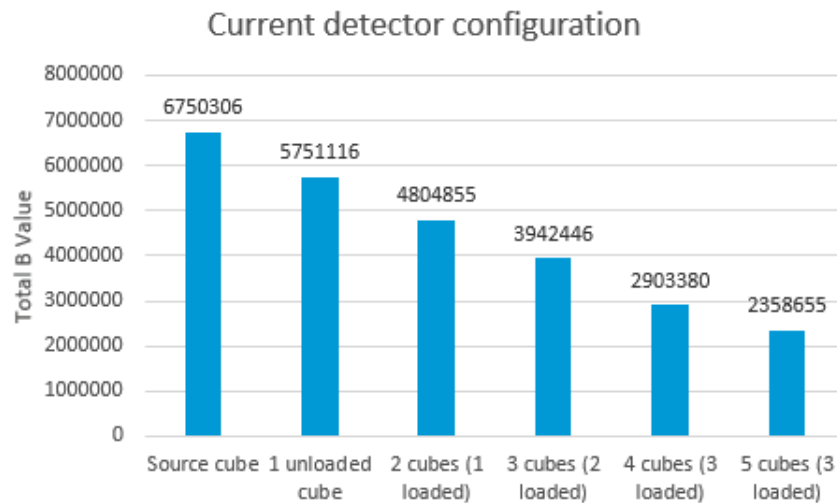
FIGURE 5.8: Data analysis result from light transmission test for current geometry. Three Li loaded cubes aligned together with two unloaded cubes at both ends.

5.1.0.2 Cross Talk test
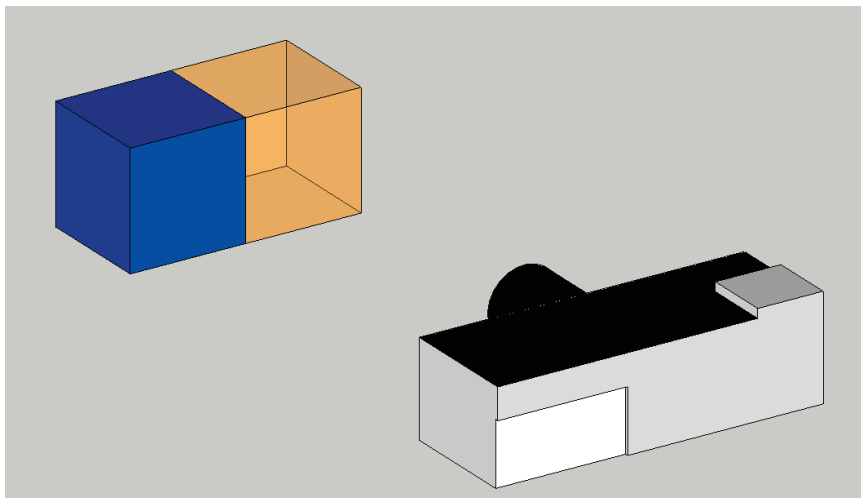
FIGURE 5.9: Sketch of structure about camera, cubes and light source for the cross talk analysis.

To have a basic understanding of the cross talk property of our Li loaded cube, we used a similar method as for the light loss test but with a different geometry as figure 5.9 shows. We put a light source at the right side of the Li loaded cube to be tested, then we took pictures from side as figure shows. The real picture is shown in figure 5.10. We compare the B value from the side to the B value from the front of the light source, it shows that around 1.5% of light was being detected from this face compared to the value we got from the light source.

FIGURE 5.10: The picture from cross talk test. Light source was put on the left side of the test. Light went through one cube and out to the right side of the cube.

To understand the cross talk actually happens in the detector, we performed a test with the current assembled NuLat detector. We used the same light source, tried to hold it at a position where it just fit exactly to side of one cube, then we took the picture of the whole detector. This geometry is similar to the condition that one cube has a particle deposition and real signal being transmitted through our detector. The picture of the whole detector from one face should mimic how all 25 PMTs on this side would respond to such a signal.

We did this test two times with different configurations and settings. For the first time, the test was taken for the configuration that the whole detector was covered with mirrors. On the side where the PMTs were mounted, there were holes previously cut so PMTs could go through there. The test was taken when the whole detector and PMTs were already assembled. We only took off one side with PMTs, so the picture was taken with the camera and light source at the same side. The geometry is shown in figure 5.11 (a).

Another test was performed when we reassembled the detector with the current Li loaded cube configuration. A picture was taken with all the side plates off. So we used better geometry. We put the light source at one side and camera on the opposite side. This setting gives the picture of the signal from both the light source directly and also the cross talk between it and the other cubes. The geometry is shown in figure 5.9 (b).

Since these two tests have totally different configurations and the first version has only 15 Li loaded cubes mounted along the center axes, it is difficult to quantify the data to do comparison. However the picture taken from these two test already showed a huge
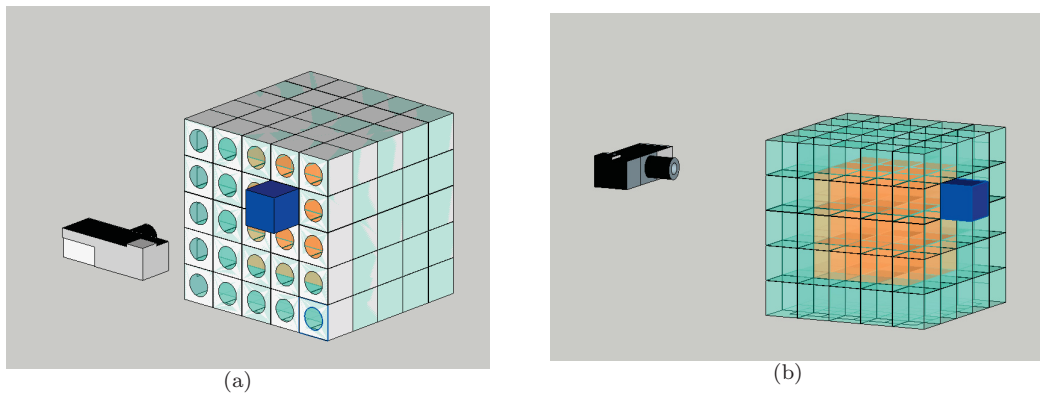
FIGURE 5.11: Figure (a) is the configuration of the cross talk test when the detector was covered by mirrors. Camera and light source are at same side. Figure (b) is the configuration of the cross talk test with just cubes and acrylic box. Light source at one side of the box and camera at the opposite side of the detector.

difference. Figure 5.12 shows the example of the pictures from these two tests. The first picture has a 10 sec exposure time and the second picture has a 25 sec exposure time, with all the other settings exactly the same on the camera. With a lot shorter exposure time, the first picture taken from the configuration with mirrors still shows a clear sign of the cross talk into a lot of different channels. However the second picture taken with the configuration with no mirror only shows slight cross talk from the channels neighbor to the main cube align with the light source. The dramatic difference of these two pictures shows that our mirror introduce a large cross talk compared to the configuration without mirror.

FIGURE 5.12: Figure (a) is the picture taken from the cross talk test with whole detector covered by mirror. The camera was set for f/4.5, ISO 800, 10 sec exposure. Figure (b) is the picture taken from the cross talk test with just cubes and acrylic box. The camera was setted for f/4.5, ISO 800 and exposure of 25 sec.

To understand better how much cross talk would be introduced by the mirror which seems more than expected, we tried another 2D version to mimic our 3D condition. Figure 5.13

shows how this experiment was setup. 25 cubes were assembled to form a 5×5 2D geometry. There are 9 Li loaded cubes in the middle with a 3×3 geometry to mimic the $3 \times 3 \times 3$ geometry we currently have in our NuLat detector. A cardboard frame was made with vm-2000 sheet attached inside to mimic the mirror we might put surrounding the cubes.

FIGURE 5.13: Cross talk experiment with a 2D version which kind mimic our current NuLat configuration. Cardboard on three sides have vm-2000 attached inside.

Two different light sources were used for this test. Figure 5.14 shows how these two light source were setup. Figure 5.14 (a) shows that the diffusive light source we used for other tests discussed before was put on top of the center cube. The light source is very weak with this configuration. So we also tried another configuration which was to put a laser beam underneath the cubes. A 45° reflective film was put underneath the center cube, there was also a hole pre-drilled there, so the laser beam could be reflected by the film and pass through the hole and the center cube.

(a)

(b)
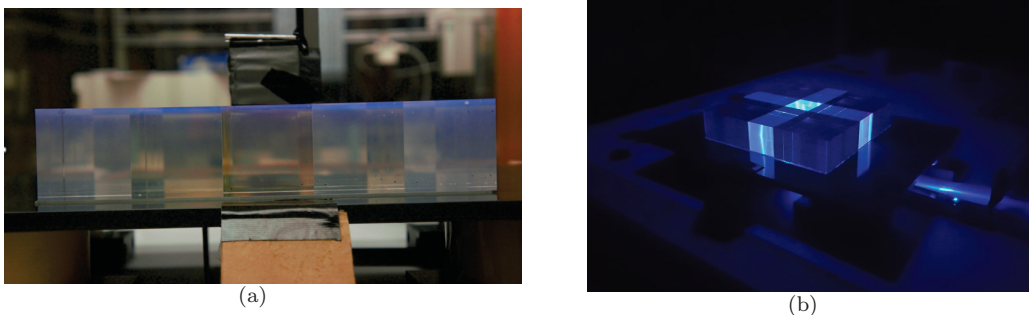
FIGURE 5.14: Cross talk test with different light source. Figure (a) shows a picture that diffusive light source was put on top of the center cube. Figure (b) is the picture that laser beam was reflected from bottom to go through the center cube.

A camera on the side can take a picture of the front face of 5 cubes. Two different pictures were taken with all the other conditions kept constant, including light source and camera setting, one with the cardboard frame surrounding to mimic the mirror existence and the other without the cardboard frame as the condition without mirrors. The actual picture taken by the camera from different light source is shown in figure 5.15.

(a) Cross talk picture with diffusive light source.

(b) Cross talk picture with laser beam source.
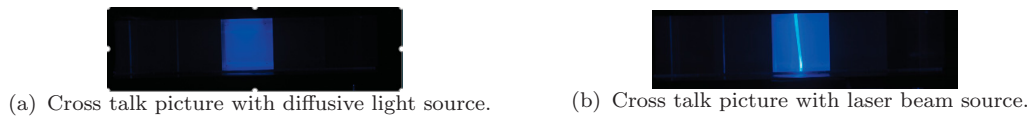
FIGURE 5.15: Pictures of cross talk test with different light source.

The analysis of the result was similar to what we did for the light transmission test. We counted the B value from a small square range we picked from different cubes and then compared them. Since the light source for this 2D version test was actually the center cube, the B value of the center face should be the major channel received, the signal from 4 faces on the two sides should be the cross talk. We normalized the result to the center face to understand how much cross talk actually shows up on different sides.

The results from different tests are shown in figure 5.16. The diffusive light source was really weak, so we have to use longer exposure time like 15 s and 25 s. On the other hand, the laser beam light source is very strong, so the exposure time for this test was set to only 0.25 s. These tests did show the difference of cross talk with and without mirrors. Although different conditions show different ratios of cross talk with and without mirror, by comparing the result from the same conditions with and without mirrors, we can tell that the crosstalk will potentially increase by $40\% \sim 100\%$ with mirrors. Since the absolute value of cross talk is not big, these amounts of increase should still be acceptable.

5.2   mTC DAQ Calibration

5.2.1   Electronics Modification

Another preliminary test we did was the calibration of the mTC DAQ system. Since this DAQ was not designed for the NuLat project, there were some hardware modification involved in the calibration.

As figure 5.17 shows, the original design make the input signal go through a $40\times$ amplifier. Because of the light channeling ability of NuLat detector, the PMTs actually receive a

(a) Laser beam source without mirror.

(b) Laser beam source with mirror.

(c) Diffusive source without Mirror (15 s exposure).

(d) Diffusive source with Mirror (15 s exposure).

(e) Diffusive source without Mirror (25 s exposure).

(f) Diffusive source without Mirror (25 s exposure).
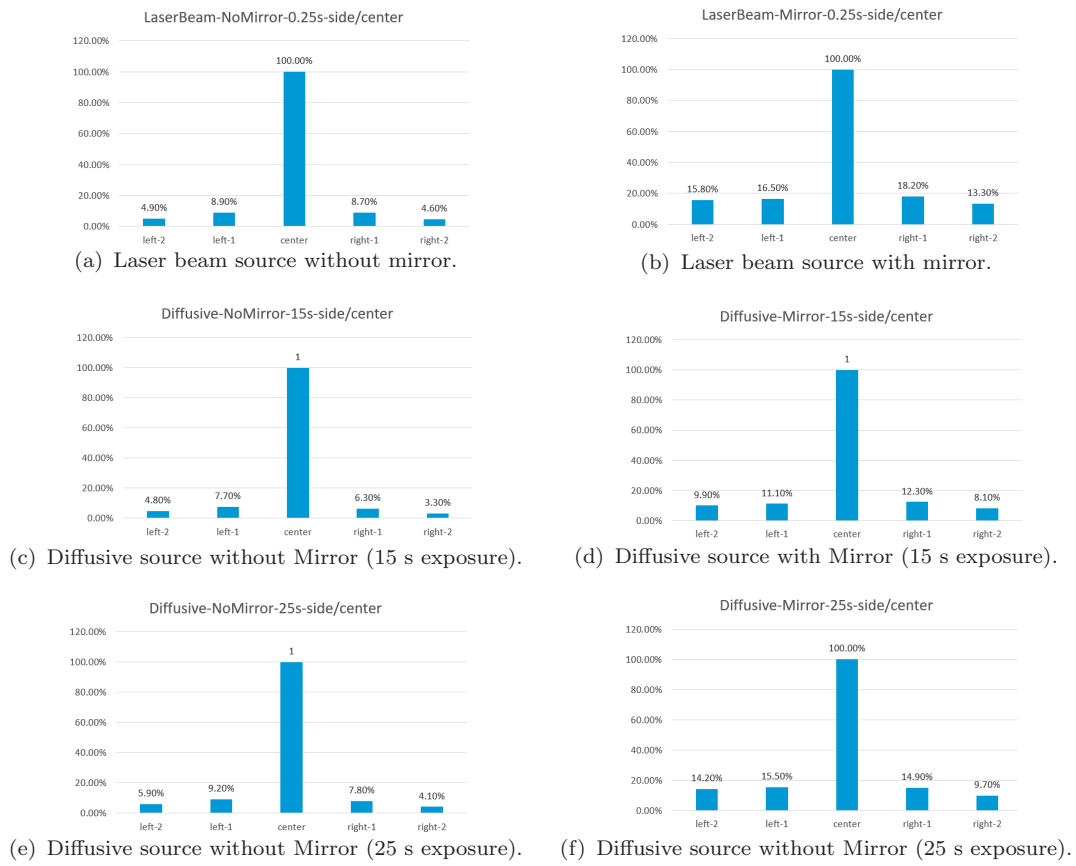
FIGURE 5.16: Different results of cross talk test with different source and exposure time.
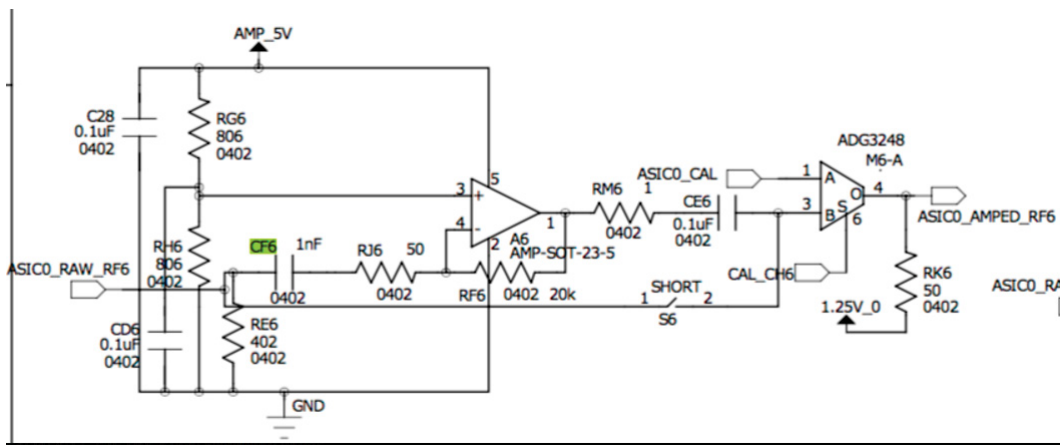
FIGURE 5.17: The partial related to the input end of the circuit on the mTC DAQ.

lot more photons than mTC detectors. So this kind of amplifier is not suitable for the requirements of NuLat. Fortunately there is a bypass switch on the board, we can solder two points on the board to close this switch and bypass the amplifier directly.
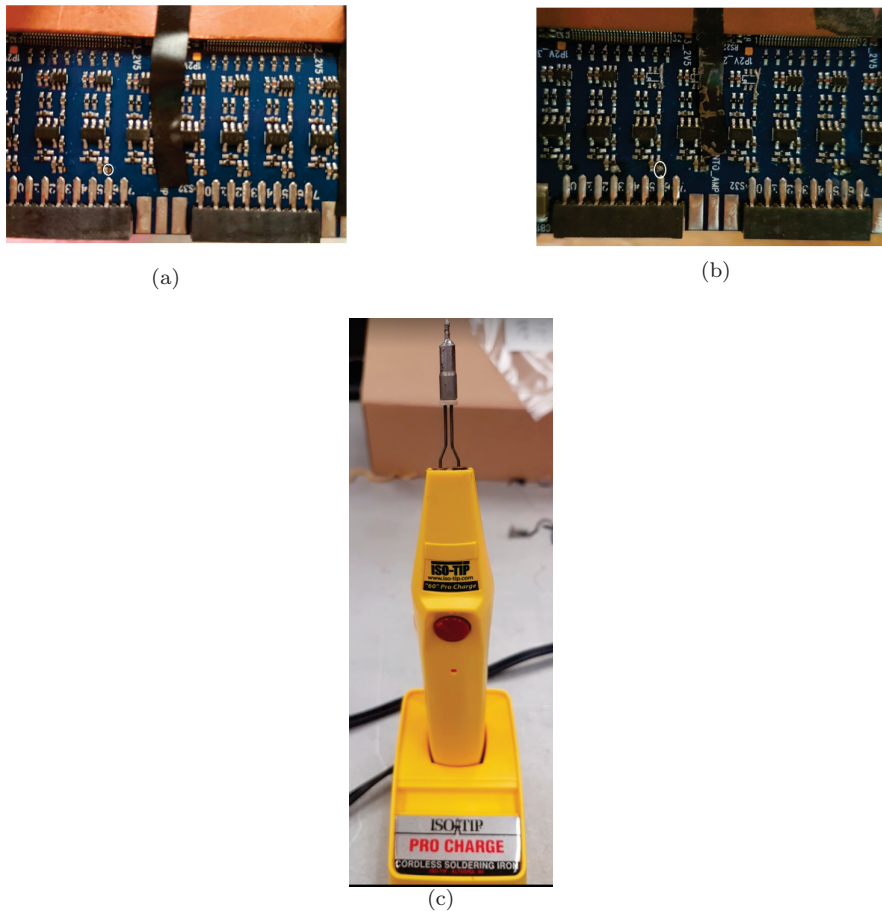
FIGURE 5.18: Figure (a) shows what the mTC board looks like originally. In figure (b), the white circle shows the position for the soldering work. A half circle golden color pin being soldered to the pin just besides it. Figure (c) shows the soldering iron we adopted to do this soldering work. It has a tiny pin which was suitable for this work.

Figure 5.18 shows how to bypass this amplifier on the real board. A half circle gold plated tip needs to be soldered to the pin just beside it. We used a special soldering iron for this work. This special tool helped to make precision soldering possible.

Another electronic modification was in the signal cable. The original ribbon cable had a different impedance than that of most RF cables used in particle physics experiments (specifically 50 Ω). However, the DAQ board shown in figure 5.17 has active 50 Ω. So, the ribbon cable was not proper for our purpose. The solution was to make a board with 32 RF cable by ourselves. We bought and cut in half some RG 58 BNC cables. The
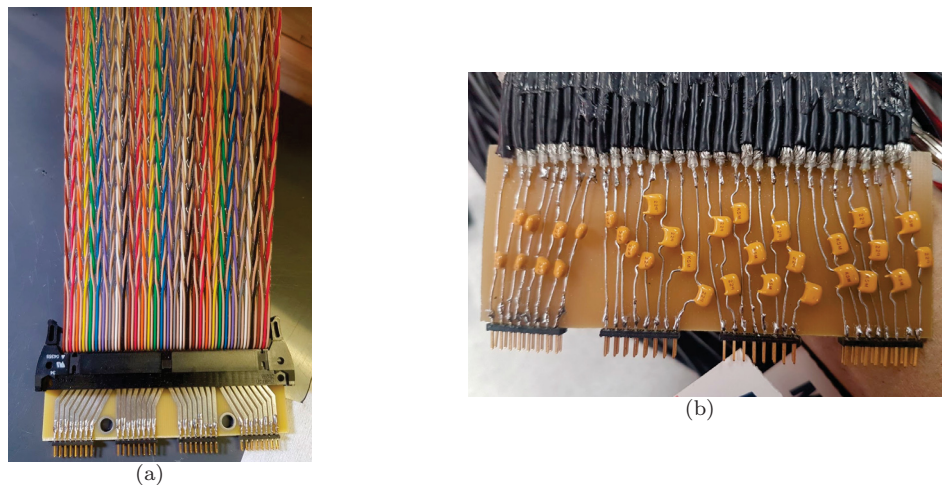
FIGURE 5.19: Figure (a) shows the original ribbon cable and connector. The impedance of this is unmatched to the common 50 Ω. Figure (b) shows the homemade connector with common RG-58 cable.

cut end was stripped a little to separate the ground shell and the wire connected to the pin. Thirty-two holes were pre-drilled on the copper clad board we bought. The wire connected to pins went through this hole and to the plastic side of the board. The ground shell was left on the other side of the board which already covered by a sheet of copper to offer common ground. After this work was done, we added a 220 nF capacitor from the wire to the pin which would plug into the DAQ board finally. This capacitor helps to block any DC offset from the signal end. The finished version is shown in figure 5.19 (b). With this design, modifications for other purpose is possible. Like figure 5.19 (b) shows, we can actually add extra resistors for signal attenuation purposes. Also we can add pull-up resistors which can give use larger dynamic range in the future if necessary.

One more modification is related to the design of our PMT (R10533). Some unexpected damage happened to the DAQ during our test. It took a while for us to realize that the PMT was actually the cause of the damage. As figure 5.20 shows, the PMT has no resistor to ground at its output end, so any charge on the anode could directly transfer to the DAQ which is not good for this kind of board. To add extra protection for this, we add a Y-shape splitter at the output end of each PMT as figure 5.21 shows. One end is connected to the signal cable as normal. We added 50 Ω terminator to the other end so the output of the PMT will have a resistor constantly connected to ground. Besides the protection this design added to our system, one more benefit is that any reflection due to the unmatched impedance will be terminated at this end. It helps us get a cleaner signal. The negative side of this kind of protection is it attenuates the signal to half, which is a big fraction of the signal.
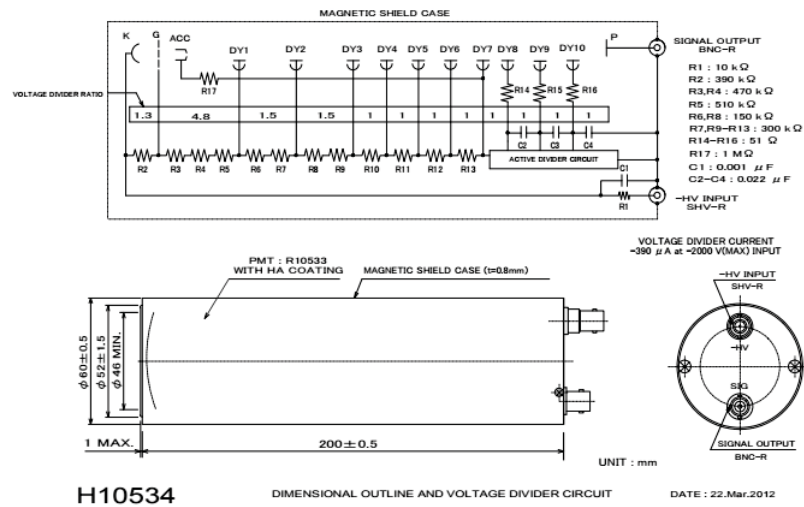
FIGURE 5.20: PMT configuration diagram.[24]

FIGURE 5.21: Picture of a Y-Shape Splitter with a PMT.

5.2.2 Test Signal Calibration

There are two things we want to understand before real data taking. First is the dynamic range of the DAQ board. The other is the effectiveness of our analysis program related to the mTC DAQ data file.

To get a brief idea of the dynamic range of the DAQ, we used a pulse generator as our source shown in figure 5.22. It has 2 channels and 4 outputs (two for complimentary pulses). This generator has ability to adjust pulse height, polarity of pulse, pulse shape (like the width of rising and falling edge) and the time difference of pulses between two channels. These functions can be set for various purposes.

FIGURE 5.22: Picture of pulse generator used for calibration purpose.
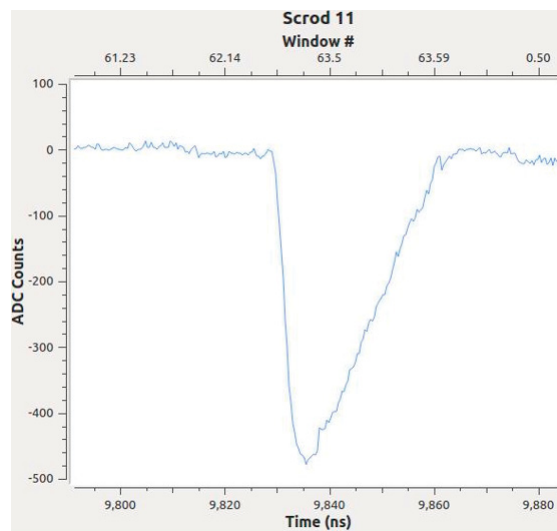
FIGURE 5.23: Example of the pulse shape from the mTC DAQ data taking process.

We used this pulse generator in a test by having it output pulses of different heights and reading output on the DAQ. It helped us to understand what kind of pulse would saturated the mTC DAQ. The sample of the calibration pulse read by mTC DAQ is shown in figure 5.23. The mTC DAQ board has a 12 bit Wilkinson ADC from 0-2.5 V. The counts for the whole range should be around 4096. With the base line around 1.25 V, at the middle of this range, the maximum a negative pulse can reach should be around 2000 counts. Because of the current firmware setting, the pulse will saturate the DAQ when it reach around 1500 counts for the ADC.

As figure 5.24 shows, we make a mapping by comparing the different pulse height from pulse generator and the recorded pulse from the mTC DAQ. The pulse from the pulse generator started at 200 mV. We adjusted its height by 50 mV each step. By comparing the original pulse and the recorded pulse from the mTC board, the figure 5.24 (b) histogram shows mTC DAQ has good linearity up to 600 mV. After that, the linearity is

pulse peak	MTC Daq
200	489
250	601
300	712
350	824
400	945
450	1074
500	1166
550	1235
600	1285
650	1346
700	1393
750	1437
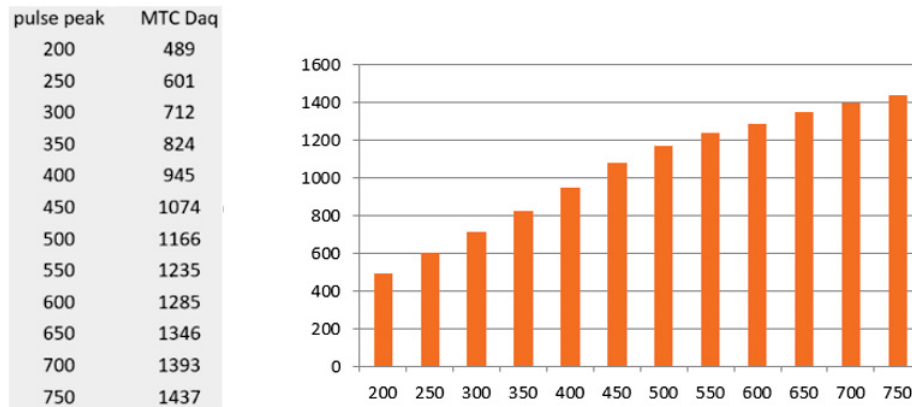
FIGURE 5.24: Data analysis of the mTC DAQ responded to the pulse from pulse generator.

not so good. Also, input signals larger than 750 mV are very close to saturate the ADC.

FIGURE 5.25: NaI detector used for mTC DAQ calibration.

The original data structure from the mTC DAQ is just the digitization of the original pulse. During our pre-analysis process, we read all the digitized information to recreate the original pulse and then we take the integral of this pulse to find the value which directly related to the energy deposited by the particle into the scintillator. To verify that our code works effectively to regenerated the pulse and compute the integral related to the energy right, we employed a NaI detector and used a ^{60}Co source as our calibration source. Figure 5.25 shows the NaI detector looks. The ^{60}Co source is a common source used for calibration. The decay process of ^{60}Co emits two gammas with different energies, one is around 1.732 MeV and the other around 1.332 MeV. So theoretically we should see

two peaks in the spectrum of this source, showing these two different energies. Also there should be a small bump which comes from the sum of these two energies. The signal from NaI detector was transferred directly from the NaI detector to the mTC DAQ system.
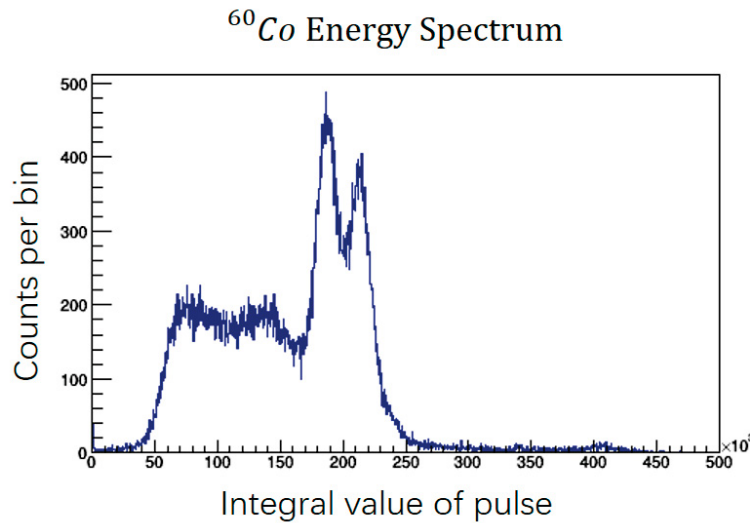
FIGURE 5.26: Spectrum from NaI detector with ^{60} Co source.

Figure 5.26 shows the energy spectrum we got after the analysis of the raw data from this data taking process. The x-axis is the integral of the pulse and the y-axis is the number of events falling into the range of the histogram defined on the x-axis. As this figure shows, there are two clear two peaks as expected. Also there is a small bump around the position doubled where the two peaks are located. This test verifies that our analysis code is compatible with the mTC DAQ to get a good energy spectrum.

Chapter 6

Radon Calibration

In this chapter, we discuss how we use radon as our calibration source to calibrate the NuLat detector. The reason to choose radon is that within its decay chain, there is a Bi-Po coincidence which is a great mimic of the IBD signal. As figure 6.1 shows, the Bi-Po coincidence begins with the β decay of ^{214}Bi and followed by an α decay of ^{214}Po with a mean lifetime of 164 μs. The maximum energy of the electron from the decay of ^{214}Bi is around 3.27 MeV. Because of the quenching effect, the light production of the alpha signal will be around 750 keV. This coincidence provides a spatially, temporally, and energetically similar structure to the IBD signal of aa anti-neutrino capture in NuLat.

FIGURE 6.1: Figure (a) shows the related decay we take advange of from the decay chain of radon. Figure (b) shows how the temporal coincidence appears on a time axis.

6.1   Radon Source

In chapter 3, we explained that when we assembled the acrylic box, we carefully sealed all the edges with tapes and checked whether it had a relatively good ability to hold gas without leakage. All these steps were for our radon calibration. In this section, we will explain how we fill radon into our detector with an adjustable system. We also describe how we use a series of NIM electronics modules to check our radon density in the detector without a too complicated analysis.

6.1.1   Radon filling method

The radon source we use for calibration was produced by our collaborators at Princeton University for testing a radon filter in the clean-room in which the Borexino vessels were constructed.[61] The source is made by Pylon Electronics and is model Rn-1025 with an equilibrium activity of 21.4 kBq and provides a continuous activity of 2692 mBq/minute[62]. The source contains powdered radium salts between two fine glass filters encased in a sealed aluminum housing with two needle valves and can be operated under vacuum or at flow rates of up to 10 LPM at 3 bar pressure.[63]

FIGURE 6.2: Picture of radon source mounted on the leg of the cart holding the current NuLat detector.

As figure 6.2 shows, the radon source is mounted on one of the legs of the cart holding the detector. Nitrogen gas is injected from the bottom. There are two paths controlled by valves. Figure 6.3 shows the gas flow diagram of our radon source filling system. To fill the radon, we need to turn on valves B and C for the nitrogen gas go through the radon source and drive radon into the detector. Valve A and D need to be closed during the filling process. With valve E and F open, radon should flow from the bottom of the detector and out from the top, then flow through the gas tube to reach the fume hood, which has slightly negative pressure to accumulate waste gas. If we want to stop radon flow and purge the detector, we need to close valve B, C and open valve A, which will let pure nitrogen gas go through the detector. If we just need to purge the gas line, we should turn off valve B, C, E and F, leave valve A and D open which will let nitrogen just flow through our gas line.
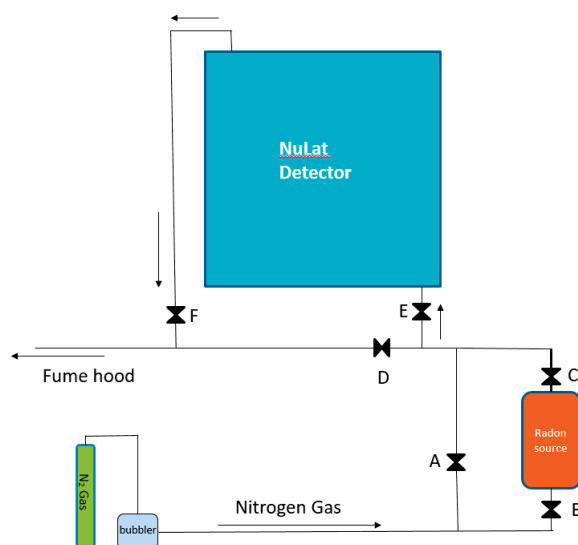
FIGURE 6.3: Radon source and gas flow diagram.

As figure 6.4 shows, the nitrogren gas flow rate is controlled by a flow-meter, and then go through a homemade bubbler. One end of the bubbler is connected to the nitrogen tube out of the gas bottle. The other end is connected to the tube directly through the input end of gas flow system. The bubbler is filled with mineral oil. The vapor pressure of mineral oil is around 1000 times lower than water. This is the reason we chose mineral oil instead of water for our bubbler. The flow rate is controlled at 1 bubble every 5 seconds. The flow rate cannot be too fast because we have to give radon enough time to build up its decay product. However, although we have tried our best to seal the acrylic box, there might still be some leakage existing somewhere around the connection. Also, the tiny negative pressure generated by fume hood keeps pulling gas out, so we also need

to maintain the speed of radon flow above certain threshold to have a steady build up. The system should finally reach a balance to maintain the radon in the detector at some stable density. It is difficult to quantify proper flow rate of nitrogen gas for our radon filling purpose because we have no clear idea about the leak rate of our detector and what kind of effect is caused by the negative pressure from the fume hood. So we tried several different flow rates and tested the radon density by checking the Bi-Po coincidence signal with the NIM-Logic electronics. We will explain how this check goes later. After several different tests, we believe the current speed of 1 bubble every 5 seconds is the proper rate for our purpose.

(a)

(b)
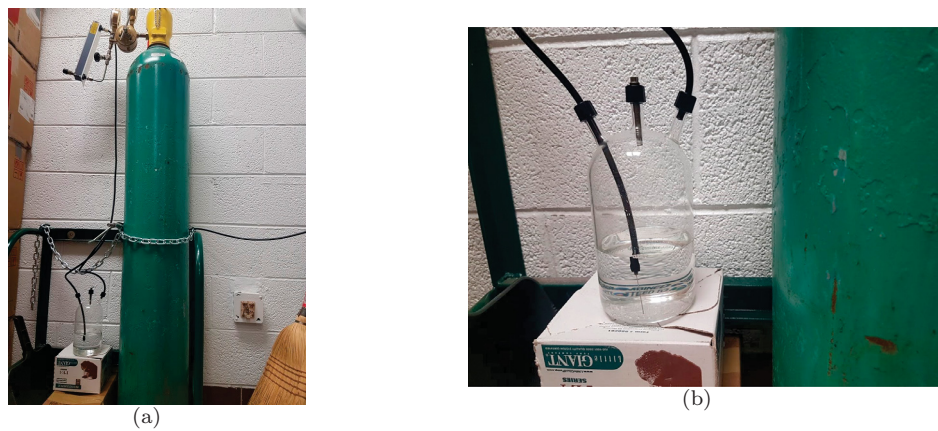
FIGURE 6.4: Nitrogen gas flow rate control system. Figure (a) shows the connection between nitrogen gas bottle, flow meter and the homemade bubbler. Figure (b) shows the detail of the homemade bubbler.

6.1.2   Method to Check the Existence of Radon

To distinguish that signals are actually from a radon decay process instead of some background noise, we use the Bi-Po coincidence in the radon decay chain as a signature. A series of electronics modules are used to check this temporal coincidence event. They connected to each other with a lot of cables shown in figure 6.5. The temporal relation of Bi-Po coincidence has been explained at the beginning of this chapter. Briefly the process is the prompt signal being the beta emission from ^{214}Bi and the delayed signals the alpha emission from ^{214}Po with lifetime of 164 μs. So if we actually catch such temporal coincidence events, we should be able to find a relation between event rate and the time difference between prompt and delayed signals of each event. The relation should be able to fit to a decay curve consistent with the 164 μs lifetime of ^{214}Po.
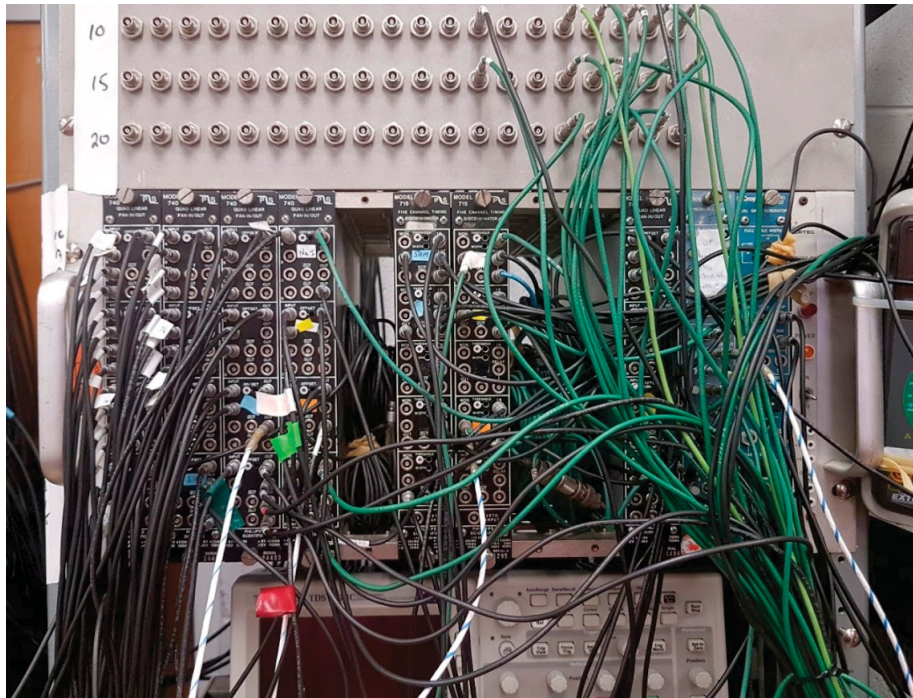
FIGURE 6.5: NIM-Trigger-Electronics.

To design a way to check whether we have such a relation in our detector, we choose to use the coincidence of 3 PMTs as our trigger source. These 3 PMTs are picked to specifically make sure they are on three different sides of detector, and diagonally they can be related to the same specific cube. A coincidence of these 3 PMTs will represent this specific cube generated some photons because of some energy deposition. We will set two trigger requirements. The first just requires the coincidence of signals from these 3 PMTs. This trigger is our prompt trigger. The other trigger is called the delayed trigger. Besides these 3 PMTs, it also requires the coincidence with a time guard signal we create deliberately. This time guard signal should be created with an adjustable delay from the prompt signal and have a fixed time window so any coincidence of three PMTs which falls into this range can fire the trigger. Within a certain amount of time of running of this system with this kind of setting, we should be able to get information about the rate of the delayed signals that fall into this fixed range of time guard with different delay from the prompt signals. This can help us verify whether this relation is consistent to the decay curve we should have.

Figure 6.7 shows the logic diagram of the electronic modules connection to providing this trigger. A LeCroy 465 is used to generate the trigger based on the coincidence of inputs. We use two ports of one LeCroy 465. One is used to generate the prompt, the input of this port is the three PMTs we picked up to select a single cube. Besides the
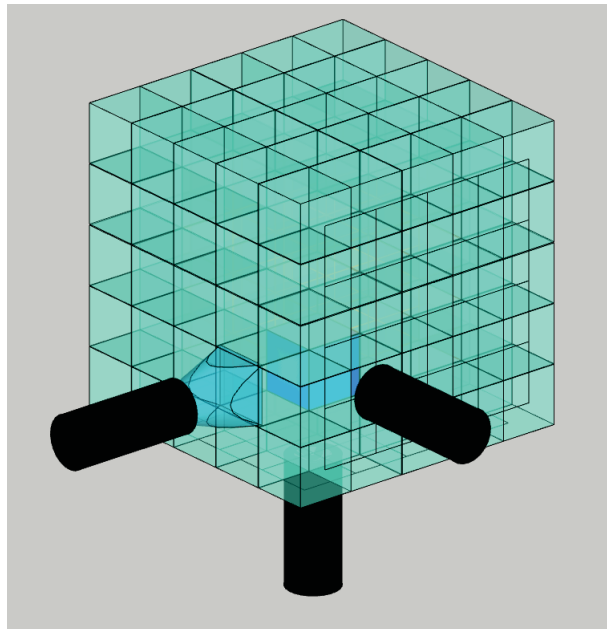
FIGURE 6.6: Three PMTs triggering structure.

same 3 PMTs, the other port has one more input from the signal generated intentionally to catch the delayed signals within a controllable range. On one side, the 25 PMTs are added together by a Phillip 744 fan in/fan out. One of the non-negligible backgrounds is from muons created by cosmic rays. The sum of 25 PMTs from a whole face can be used to veto such signals. Most muons are produced high in the atmosphere (typically 15 km) and lose about 2 GeV to ionization before reaching the ground.[64] Muons deposit around 2 MeV/cm when they pass through PVT plastic scintillator.[65] So if there are muons passing through the NuLat detector, the sum of the whole face should show a huge signal (around 12 MeV from one cube) compared to the signal from radon decay. We are using Phillip 715 constant fraction discriminator modules to set a high threshold (0.5 V) for this summed signal and feed the output into the veto port of the LeCroy 465 modules to detect the coincidence. If the summed signal crosses the threshold, then the event will be vetoed because of this connection.

A Lecroy 222 is used to create the two time guards we need to verify the temporal coincidence. In practice, one Lecroy 222 will create a delayed signal immediately after the prompt signal is fed in. Simultaneously a NIM square signal representing how long the delay has been set would be fed into a veto to make sure no more signals would be accepted as a prompt signal within this time range. This delayed signal will be fed into another port of the Lecroy 222, a 10 μs NIM square signal will then be generated and fed into another port of LeCroy 465 for the delayed coincidence trigger.
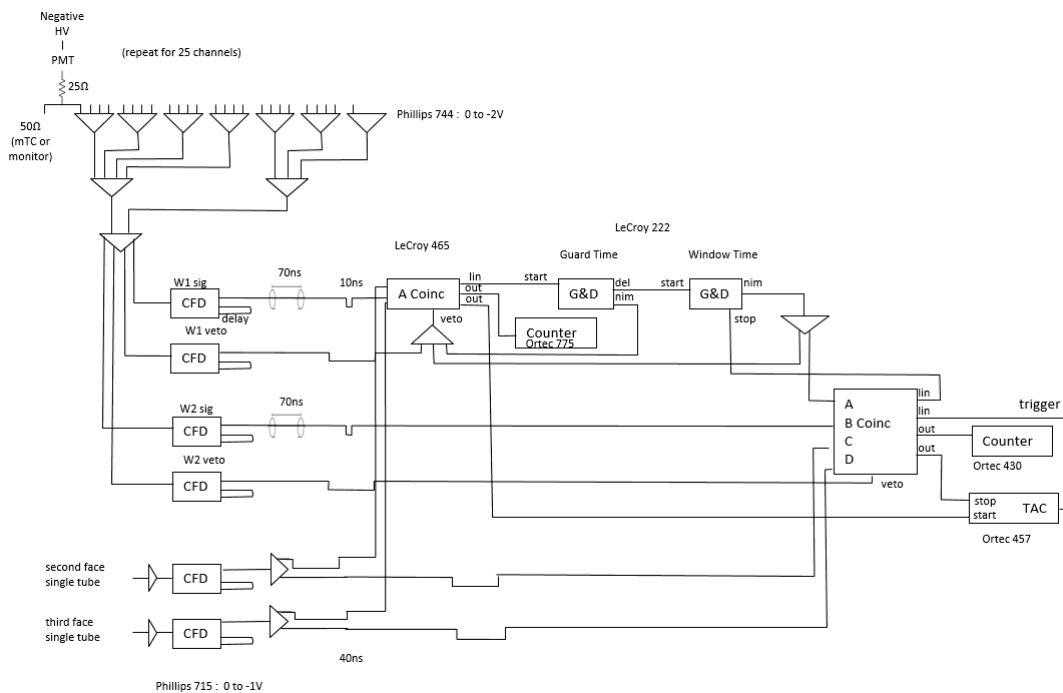
FIGURE 6.7: NIM-trigger-diagram.
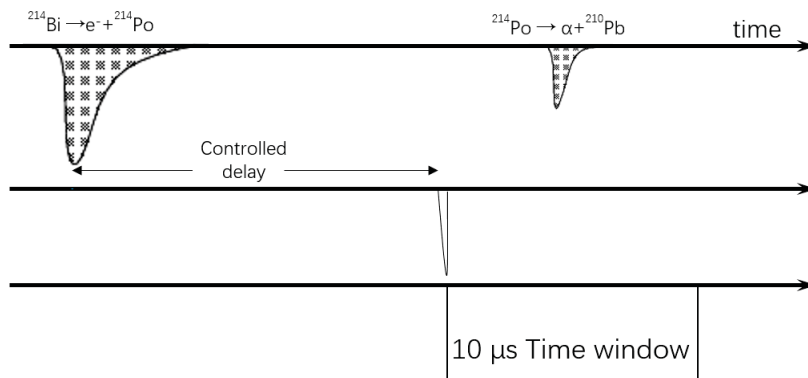
FIGURE 6.8: Timing diagram of the triggering for coincidence.

As figure 6.8 shows, by adjusting how long the delayed signal will be generated after the prompt signal, we can actually adjust the time difference between the 10 μs guard signal and the prompt signal. If a real Bi-Po coincidence is being caught by this guard effectively, the event rate should be reduced just like the decay curve of ^{214}Po as we adjust the delay of the 10 μs guard signal away from the prompt signal.

As explained before, since the lifetime of ^{214} Po is 164 μs, if the temporal coincidence being caught is far away from that, like 1000 μs, the event being caught should not be related to the ^{214}Po decay, and we can treat that rate as our background. Although we mostly did counting within a certain time range (typically a 200 s run), the coincidence events being counted cannot be used directly. We also need to include the effect that each run has different number of prompt events. Especially when we adjust the time difference between the 10 μs guard signal and the prompt signal, it introduces different dead time for each counting which affect the number of prompt signals being caught by each run dramatically. So during the actual measurement, we counted both the number of coincidence event and prompt event and treat the ratio between these two numbers as the true coincidence rate.

In practical work, there are some electronics we employed to simplify the counting job. We used ORTEC model 719 timer to create a 200 s time window. This time window was an input gate into a ORTEC 775 counter and ORTEC model 430 scaler so these two devices would doing counting in this 200 s. Model 775 was connected to the prompt trigger signal to count the prompt evens within 200 s. Model 430 was connected to the delayed coincidence event to count how many coincidences we got in this time window.

PMT(V)	windows(us)	guard(us)	run (s)	N (stop)	N (start)	1k*stop/start	background-cut
1750	10	10	200	1878	83842	22.40	7.4
1750	10	50	200	1764	81114	21.75	6.7
1750	10	100	200	1573	77841	20.21	5.2
1750	10	150	200	1453	74999	19.37	4.4
1750	10	174	200	1417	73967	19.16	4.2
1750	10	200	200	1331	72652	18.32	3.3
1750	10	300	200	1186	68955	17.20	2.2
1750	10	400	200	1056	65824	16.04	1.0
1750	10	500	200	1004	63019	15.93	0.9
1750	10	600	200	914	61272	14.92	-0.1
1750	10	700	200	936	59066	15.85	0.8
1750	10	800	200	870	57740	15.07	0.1
1750	10	900	200	827	55852	14.81	-0.2
1750	10	1000	200	1637	108896	15.03	0.0

FIGURE 6.9: Event counting result from different time delay setting.

Figure 6.9 shows the example of one counting we did for Bi-Po coincidence check. We started with a time difference between the prompt event and delayed square signal of 10 μs. Then we kept pushing the delayed 10 μs time window away from the prompt event until reaching 1000 μs. We compute the effective rate by dividing the number of stop

signals to the number of start signals. Stop signal should be related to the coincidence and starts related to the prompt events. The rate we got at 1000 μs delay was treated as the background rate, so the true rate for all the other event should be the

$$Rate_{true} = Rate_{raw} - Rate_{bg} . \tag{6.1}$$
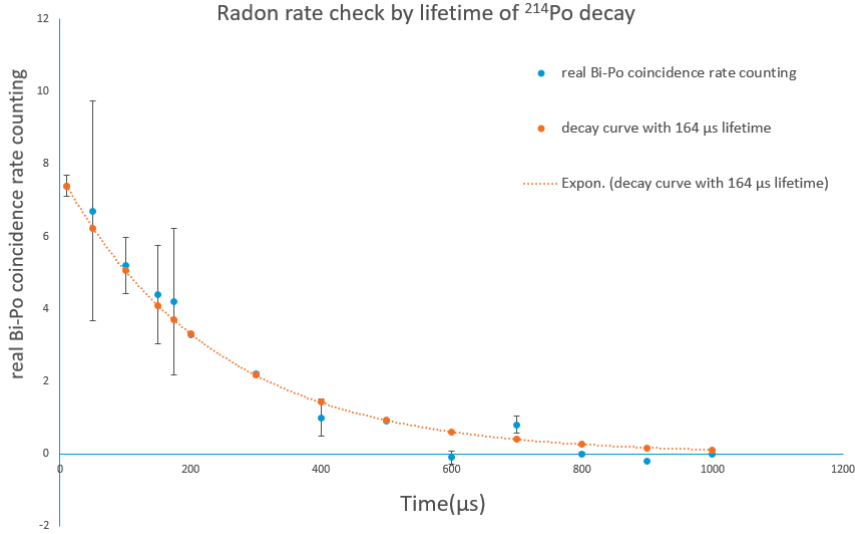
FIGURE 6.10: Comparison of the coincidence rate from experiment and the theoretical curve from the lifetime of ^{214}Po decay.

Figure 6.10 shows the decay curve checking we did from this data set. Blue dots are the data we got from actual data taking, and orange dots and curve show a curve with decay time of 164 μs. From this figure, we can tell that they matched to each other pretty well. It was a good proof that we actually have radon in our detector and our trigger method is able to pick up the true events effectively. Using this system, we can check the Bi-Po coincidence caught by a specific cube easily.

6.2 Radon Calibration with Muon Trigger Mode

6.2.1 Three PMTs Triggering Mode

In the last section, we discussed how we verified radon existence in our detector with logic electronics. There is a direct way to adopt the same schematic, feed the signal into mTC

DAQ system and get the energy spectrum of the alpha signal. In this section we explain how this goes and what the spectrum looks like.
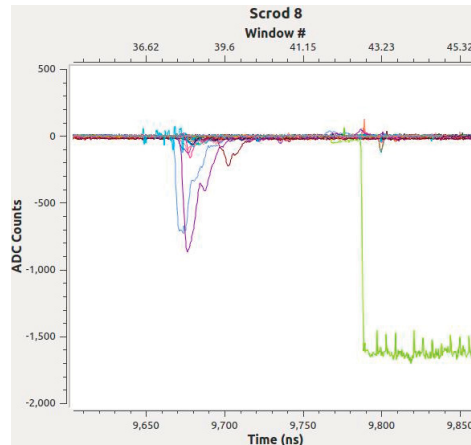
FIGURE 6.11: Sample of signal from simple trigger with NIM Electronics. The huge green square signal is the signal of the NIM trigger. All the pulses in front of this square signal are actual pulses being recorded by each channel.

As explained in chapter 3, there is a simple trigger mode which can be set on the mTC DAQ. We can adopt this trigger mode with the NIM-Logic signal we explained before to trigger the data acquisition process. The NIM-Logic signal will be fed into one channel of the DAQ. Except for this channel, L0 for all the other channels will set to their maximum. This setting make all these channels unable to be triggered by any signal. L0 for the channel with the NIM-Logic signal input should be set around 500 counts lower than the baseline. This threshold is low enough so only the NIM-Logic signal can cross this threshold. Besides the L0 trigger, we also set the range of number of hits which will fire the simple trigger to be from 1-2, this requires that if one channel crosses the L0 threshold, it will start the digitizer and data acquisition process. Figure 6.11 shows how the data looks from a simple trigger mode. The green square pulse is the pulse from NIM-logic, the pulses in front of it are all the pulses which need to be analyzed.

We can work on two different geometric settings for this kind of trigger. The first structure is exactly the same as explained before, three PMTs orthogonal to each other on three sides being picked up by the geometry that they all align with the same cube. We just need to use the same trigger logic with the pulse being digitized by mTC DAQ to analysis the Bi-Po coincidence being caught by this specific cube.

To get the background spectrum from this setting, we directly adopt the signal from the prompt event as our trigger. Since there is no temporal coincidence requirement in the trigger, all sorts of energy deposition to this cube from all different kind of sources being
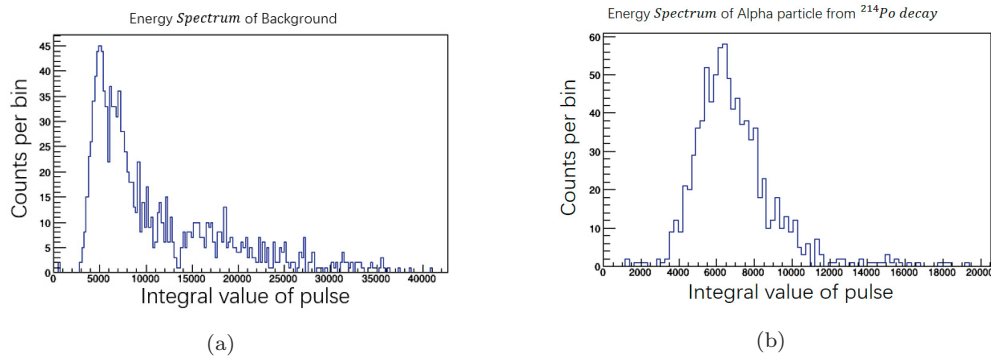
FIGURE 6.12: Figure (a) is the spectrum from the background data and figure (b) is the spectrum from the alpha particle deposition.

fed into the DAQ are triggered. So the analysis of the result from this setting shows how the spectrum of background looks like. Figure 6.12 (a) shows an example of this analysis. For the real alpha particle spectrum analysis, the trigger is from the delayed events, which requires there should be a temporal coincidence realtion between prompt and delayed signal. It is triggered by the delayed signal, so only pulses from delayed signals are recorded. As we already explained, the delayed signal is from alpha particles with effective quenching energy around 750 keV. Figure 6.13 (b) shows a Gaussian like spectrum which should directly relate to this energy.

6.2.2 One PMT Triggering Mode

Another trigger mode is to use only one PMT as our trigger source instead of coincidence from 3 PMTs. Figure 6.13 shows how this setting geometrically looks. The negative side of this is there will be more background noise than the geometry we discussed before. 3 PMTs give us a better defined geometrical requirement which can reject most of the noise. However, it gives the benefit that within same time of data taking, all the Bi-Po coincidence being caught by 5 cubes aligned with this PMT are triggered. So by analyzing the data taken from this geometry, we can calibrate all 5 cubes simultaneously.

The extra noise from this geometry can be rejected by requiring that the largest signals on each of 3 sides correspond to a single cube. Figure 6.14 shows this requirement being used during the analysis process. We do an energy mapping as figure 6.14 (b) and (c) shows. All the energy for different PMTs are mapped geometrically to where they belong. Based on our configuration, if the analysis shows that the specific PMT we trigger from has a large energy deposition but all the other PMTs on the same side have low signal, it
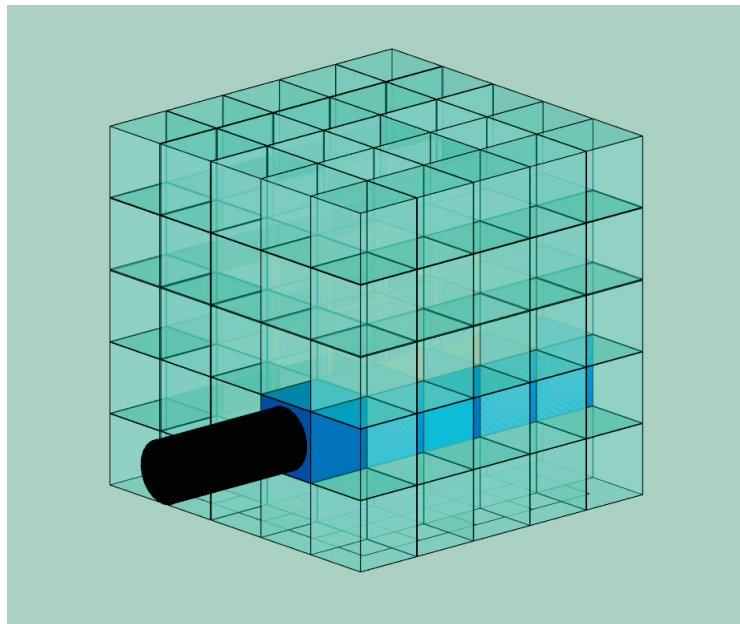
FIGURE 6.13: Sketch of the geometry for triggering by one PMT.

(a)

(b)

(c)
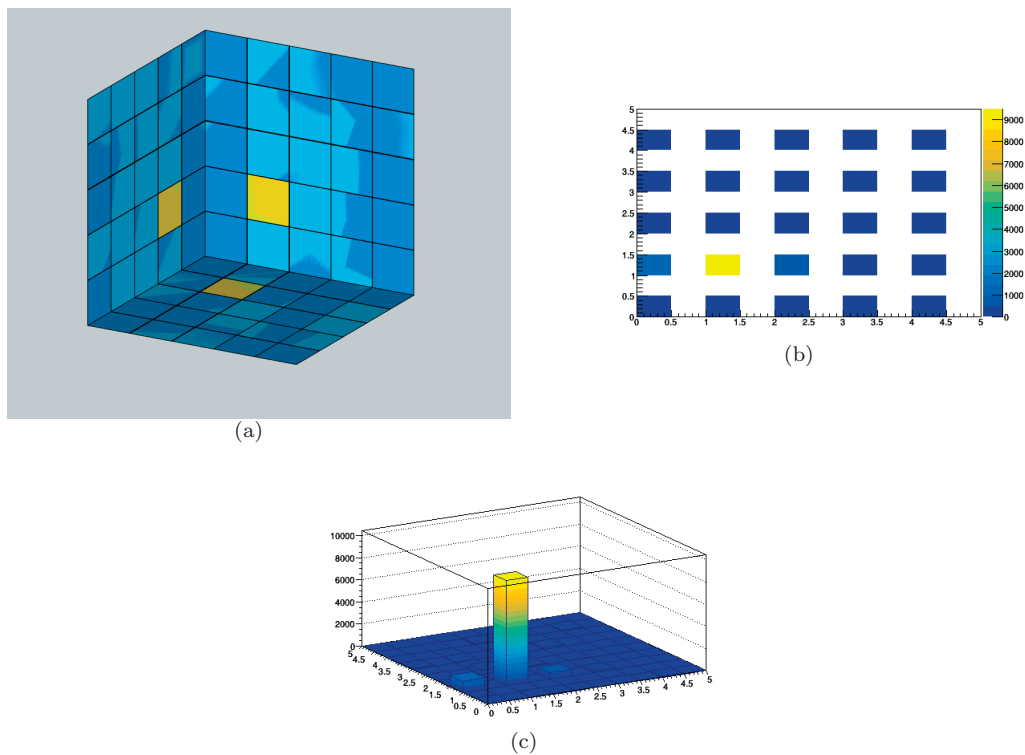
FIGURE 6.14: Example of energy mapping from data analysis. Figure (a) shows a 2D energy mapping on three side of the detector. The pixel with yellow color means it received real signals and the pixel with blue color means there are really low or no signal has been received. Figure (b) shows an example of the 2D mapping from one side of the detector, it also contain the bar shows the meaning of color mapping. Figure (c) shows a 3D example of the same energy mapping from one side of the detector.

means only cubes aligned with this PMT have energy deposited. As figure 6.14 (a) shows, if all three sides have PMTs meeting this requirement and these three PMT diagonally converge to the same cube, it shows that the signal is exactly from one specific cube. With this setting, although we only trigger from one PMT, all the information related to each cube aligned with this PMT can be deliberately picked out and analyzed individually. Since we can locate which cube has the alpha particle deposition, we can then analyze the pulse and get the spectrum from 3 PMTs geometrically aligned with this cube. Then the spectrum should looks similar to what we got when we intentionally triggered from only one cube.

With the first geometry, we can only understand how the alpha energy spectrum looks from 3 PMTs. However with this geometry, a lot more information can be understood which is extremely useful. Firstly, since one PMT is our trigger source, it is aligned with all 5 cubes being analyzed. So we can check how the energy spectrum looks like on this PMT from these 5 different cubes. The major source of the energy spectrum should comes from 750 keV alpha deposition. However, since the photons generated by the scintillator have to go through different number of cubes to reach this PMT, by comparing the 5 spectrum from 5 different cubes, we can understand light loss during the travel of photons through each cube. Another analysis which is useful is PMT gain match test. Since there are also 5 PMTs on another side that related to these 5 cubes independently, but the distance between the cubes we are analyzing and these PMTs are the same, so the alpha spectrum from these 5 PMTs actually shows the different gain of these 5 PMTs responding to the similar number of photons they received.

Figure 6.15 shows how these two analyses looks. Figure 6.15 (c) is a 2D graph to show how PMTs and cubes are related. The orange PMT labeled number 2 is the PMT of our trigger source, we just name it PMT-O2 in this section. There are 3×3 cubes in the middle marked as brown color to show that they are Li loaded and all the others are ordinary scintillator cubes. In figure 6.15 (a), cubes are labeled 1-5 depending on the distance between them and the PMT-O2. The first cube which directly attached to the PMT-O2 is labeled 1. Figure 6.15 (a) shows a relative linear drop for each cube further from the PMT-O2 and the drop is around 14% after each cube. This amount of drop is consistent with the light loss check we did with the camera explained in chapter 5. Figure 6.15 (b) shows the result of PMT gain matching test. The result is from 5 PMTs labeled 1-5 with blue color. This graph shows that there is actually big difference between the gain of these 5 PMTs.
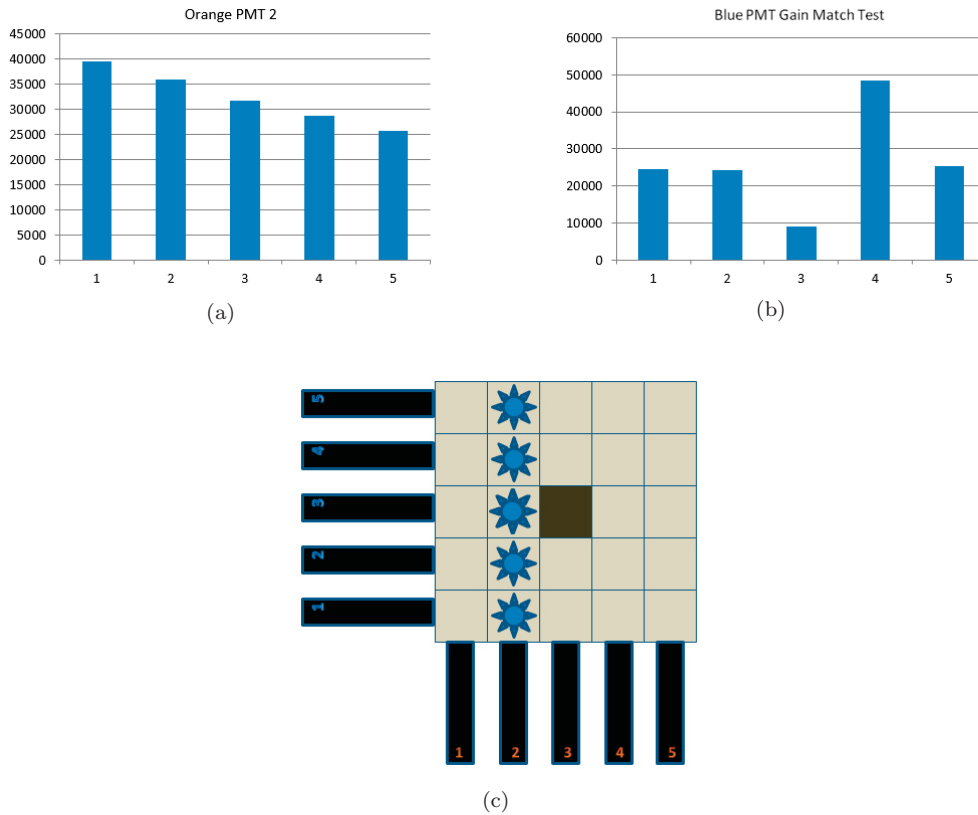
FIGURE 6.15: Calibration analysis done by one PMT trigger mode. Figure (a) shows the calibration of same PMT with signals from different cubes aligned with it. Figure (b) shows the calibration about different cubes and different PMTs with same number of cubes between them. Figure (c) shows the 2D sketch showing calibration triggering by one PMT.

6.3 Radon Calibration with AB Trigger Mode

This simple trigger model can be used for calibration purpose, but for IBD event data acquisition in the future, it is not good enough because this trigger mechanism loses all the information from the prompt event. The AB trigger model controlled by the CAJIPCI should be the major trigger mode when the NuLat detector does an effective antineutrino detection. The mechanism of AB trigger has already being discussed in chapter 3. Currently, the time difference between prompt signal and delayed signal current is limited to a range from 0-10 μs. We can use this time window as time coincidence to catch prompt signal and delayed signal. For our radon test, prompt signals should from beta capture and delayed signal should from alpha capture. For the future antineutrino detection, the prompt signal would be positron capture and delayed signals would be neutron capture. A more effective AB trigger mode will be a mode also contains geometrical coincidence,

which should effectively reduce the background rate. But it needs more work on firmware programming and should be done in the near future.
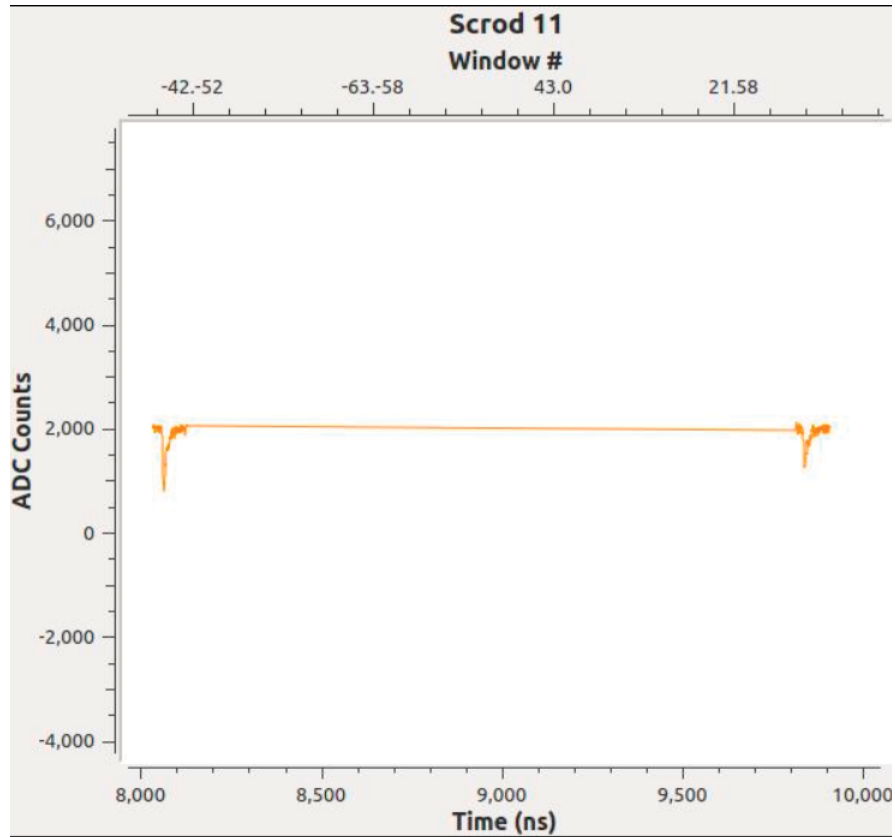
FIGURE 6.16: Sample of signal from AB trigger mode. It shows that both prompt and delayed signals are being digitized and recorded.

To avoid the large background rate with currently basic AB trigger mode, we adopted the same geometry explained before which is triggering from only one PMT. Since the AB trigger has the temporal coincidence requirement already, we can trigger the system just from the DAQ without the help from NIM-Logic we introduced before. Although by doing this, we lose the other features such as the muon veto ability from hardware, but it is easy to fix this by analyzing the data afterwards.

To set this trigger, we set the L0 trigger similar to the way we do for a muon trigger. In practice, we set the threshold for this channel just around 30 counts lower then the baseline. This should be low enough to avoid any trigger caused by electric noise from the hardware without rejecting real events. The threshold of all the other channels are set to be maximum to avoid any trigger from these non-relevant channels. The minimum and maximum number of hits are set to be 1 and 2 as we did for the simple trigger explained before. Also we need to set the range of the time difference between A and B events. We

normally set it to be 20-200 time windows which means 1-10 μs. This setting means as long as B event happens within this range after A event, the data acquisition process will be triggered. Figure 6.16 shows how the pulses looks from the AB trigger mode.

6.3.1 Beta and Alpha Spectrum Analysis with AB Trigger

(a) 3D geometry of one PMT trigger.

(b) 2D energy mapping on three side of the detector.

(c) 2D energy mapping of one side of detector.

(d) 3D example of the same energy mapping from one side of the detector.
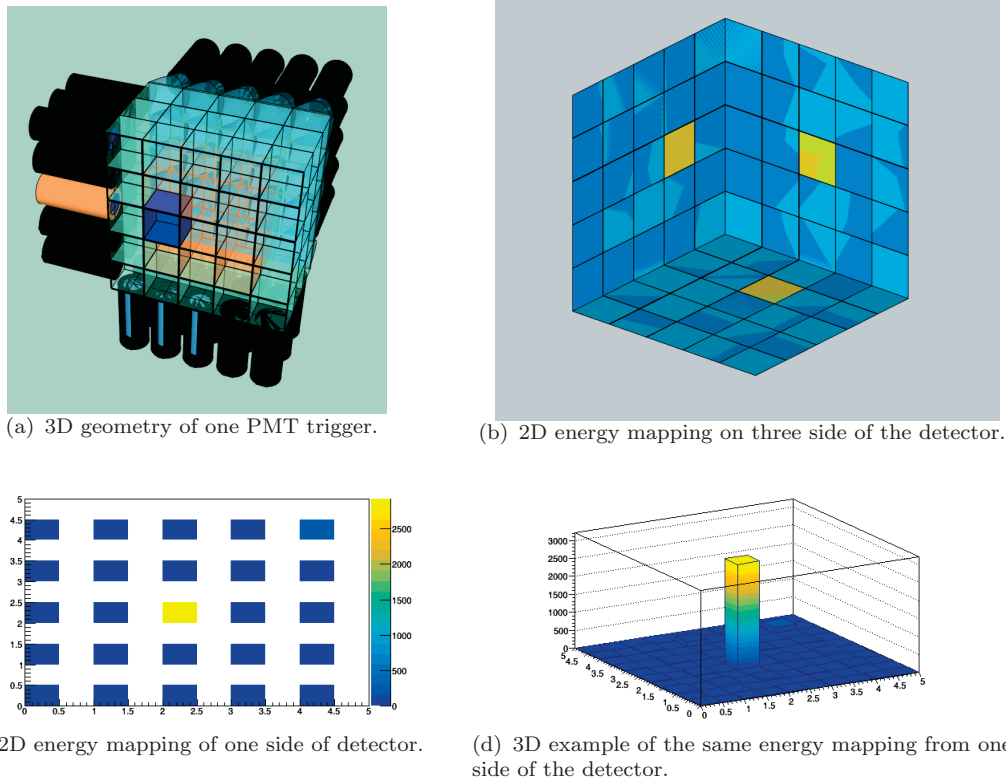
FIGURE 6.17: Example of one cube analysis from AB trigger result.

Since the trigger source is one PMT, the analysis of the result will be similar to what we explained in the last section. Figure 6.17 shows an example of a one cube analysis we did with this AB trigger mode. The PMT marked orange is the source of trigger. The cube marked blue is the cube we picked by geometry to analyze. As explained before, to make sure only this cube gets energy deposition during the data acquisition of this event, we do a energy mapping of three sides of the detector and check whether only the PMTs geometrically aligned with this cube have large signals. Figure 6.17 (b) shows a 2D energy mapping of three sides of this detector. We can tell from figure 6.17 (c) and (d) that if the color of the pixel close to blue, it means the signal from PMT at this pixel is really low. On the other hand, yellow color means the PMT at this pixel actually has real signal output.

The major benefit of this AB trigger mode compared to the simple mode we explained before is that we are able to recreate the pulse from prompt signal the same as the delayed signal. With this ability, there are several useful analysis approaches we can use to have a better understanding about the coincidence event we are interested in.
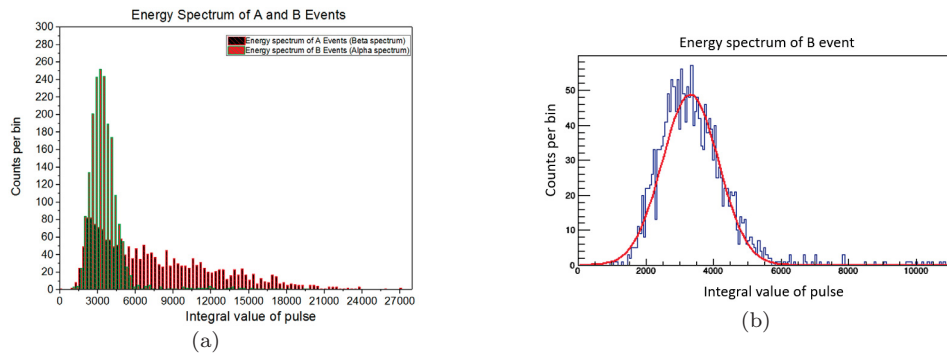
FIGURE 6.18: Spectrum analysis about Bi-Po coincidence. Figure (a) shows a combined version with both beta and alpha spectrum being presented. Figure (b) shows a separate alpha spectrum from same data set.

The direct analysis we can do is to get the spectrum from both prompt and delayed signals. Figure 6.18 shows how the spectrum looks. Figure 6.18 (a) shows both of the spectrum from prompt and delayed signal. These two spectrum are actually analyzed from the same PMT and we search for the events geometrically well defined so both prompt and delayed signals came from the same cube. It shows clearly that delayed signals look like a unique energy spectrum from alpha particle deposition and the spectrum of prompt events has a wider energy range which is consistent with a beta spectrum. Also as we already know from the Bi-Po coincidence, the maximum energy of beta particles is close to 3.27 MeV and the energy of alpha particles is around 750 keV with the quenching effect of the scintillator. So the edge of the beta spectrum should be around 4 times higher than the mean value of the alpha spectrum. When we check this ratio with figure 6.18 (a), this figure is actually consistent with our prediction. This analysis is a good mimic of IBD event analysis NuLat detector should deal with in the future. IBD events have similar temporal coincidence like Bi-Po coincidence. The delayed signal in an IBD event is from neutron capture by ^6Li and also have a unique energy like the alpha particle from the decay of Po. This analysis helps us to get an energy spectrum of the positron created by the IBD reaction which carries most of the energy from the antineutrino we want to detect.
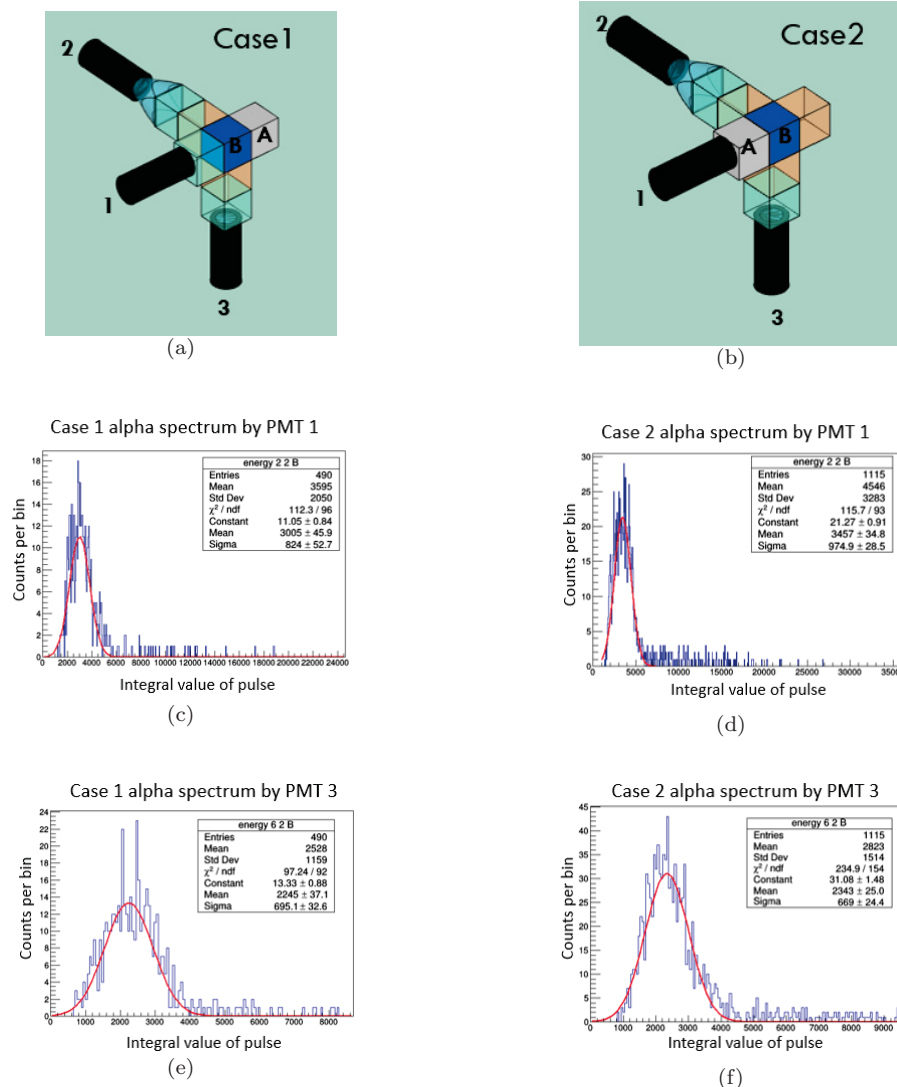
FIGURE 6.19: Analysis where signals of A and B are from different cubes. Figure (a) and (b) shows different definition of the geometry when we pick up real events. Figure (a) shows that the events are defined intentionally to the plane between the second and third cube from the PMT1, on the other hand, figure (b) shows another geometry that events are required to happen at the plane between the first and second cube. The Alpha spectrum from these two case received by PMT 1 and 3 are summarized in figure (c)-(d).

6.3.2 Well Defined Geometry Analysis with AB Trigger

Another analysis which is a little different to what we just explained is that we can also require A and B signals come from two different cubes neighboring each other, thus deliberately picking up events where the Bi-Po coincidence happens in the thin air gap between these two cubes. Figure 6.19 shows this analysis. Figure 6.19 (a) and (b) show two different geometrical structures, the delayed signal comes from the same cube, but prompt signal comes from different cubes. In case 1, Bi-Po coincidence is in the air gap between two cubes away from PMT1, however in case 2, Bi-Po coincidence is in the air gap only one cube away from PMT1. Figure 6.19 (c)-(d) shows four different energy spectra related to PMT1 and PMT3 from case 1 and 2 separately. These 4 energy spectrum are all alpha spectra detected by these 2 PMTs in these 2 cases. By comparing the mean value of these spectra, we can tell that the mean value of the spectrum from PMT1 has a clear rise of around 14% when the air gap where the Bi-Po happens one cube earlier related to the PMT1. This shows that when photons travel through 2 cubes instead of one cube, there is an extra 14% loss. This loss rate is actually consistent with what we got from our camera analysis and also from the result of analysis we did with the simple trigger explained before. When we check the response of PMT3 with these two different geometric structures, the mean value becomes a lot closer. This is also consistent with our prediction because the distances photons have to travel to reach PMT3 in these two cases are actually very similar.

6.3.3 PMT Gain Matching Analysis with AB Trigger

Besides these two analysis which depend highly on the geometrically defined A and B signal, we can also do the PMT gain matching which is similar to what we did with the simple trigger. Figure 6.20 shows an example of how we are doing this analysis and understanding the difference of gain of 9 different PMTs on one side. Three PMTs marked orange are the source of trigger from three different data acquisition process. Each time when we set one PMT as our source of trigger, the signal generated by 5 cubes aligned with this PMT can be well understood. So when we organize the analysis of the result from the data with these 3 different PMTs as our trigger source, we can fully understand the 15 cubes align with them. However, because we currently have $3 \times 3 \times 3$ Li loaded cubes in the center surrounded by unloaded cubes, and these two kind cubes have different light yield, we only pick up the result from 9 Li-loaded cubes as our major calibration cubes. Figure 6.20 (b) shows how these 9 cubes relate to the PMTs with light

	Y1	Y2	Y3
X1	2287	6687	8201
X2	5763	6191	4122
X3	2406	6251	5953
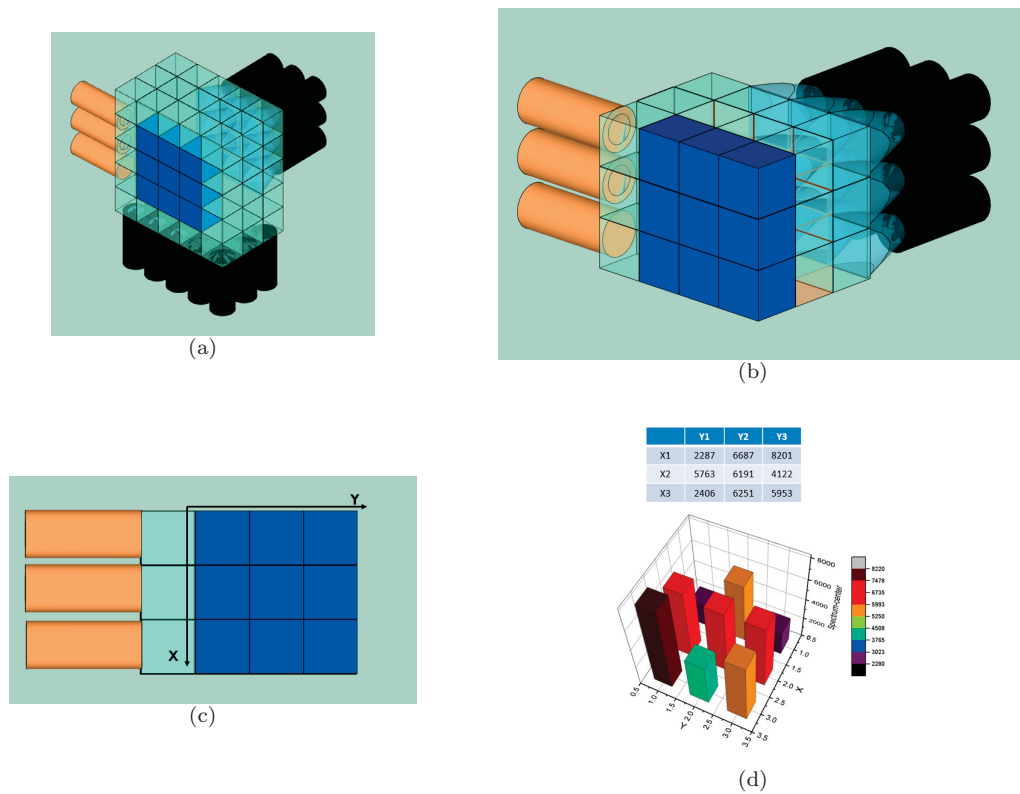
FIGURE 6.20: Example of analysis for PMT gain match. It shows the result from the analysis of the different gain on the side with PMT and light guide. All 9 PMTs facing the Li Loaded cubes are compared by their response to the alpha signal from the third cube from these PMTs. Figure (a)-(c) explain the geometric structure of this analysis, PMTs marked as orange are the PMTs working as trigger source for each data taking run. Figure (d) shows a summary of the result from this gain matching analysis.

guides. There are two cubes between the cubes we analyzed and PMTs with light guides. The mean value of the alpha spectrum from these PMTs are mapped by a 3D histogram shown in figure 6.20 (d).

Chapter 7

Summary Of Calibration Result Related To The Solid Scintillator

In chapters 5 and 6, we described many tests we performed. Some of them were directly on the scintillator and electronics, others were from actual data taking from the assembled NuLat detector. In this chapter, we summarize all the information we got from these tests related to the current solid scintillator we are using. It also gives us hints about what kind of improvement we need for the next generation NuLat detector.

7.1 Light Transmission Property of Current NuLat Detector
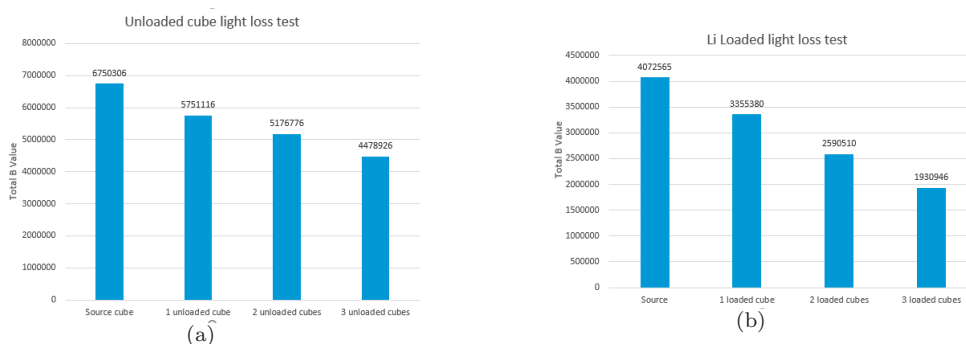
FIGURE 7.1: (a) Data analysis result from light transmission test for unloaded scintillator (b) Data analysis result from light transmission test for unloaded scintillator.

In chapter 5, we introduced the light transmission test through a different number of cubes with a diffusive source. The result from unloaded cubes and Li loaded cubes are as figure 7.1 shows. The comparison shows that the light loss through each unloaded cube is around 11%-14%, however, this ratio increase to around 20% or higher when a Li loaded cube replaces the unloaded one. There might still be some misinterpretation of the result from the camera, but we are convinced by the comparison that there is more light loss during the light transportation due to the Li loaded cubes.

(a) A and B signal defined to different cube with A signal at the cube further from PMT1.

(b) A and B signal defined to different cube with A signal at the cube closer to PMT1.

(c) Alpha spectrum by PMT1 from case 1.

(d) Alpha spectrum by PMT1 from case 2.
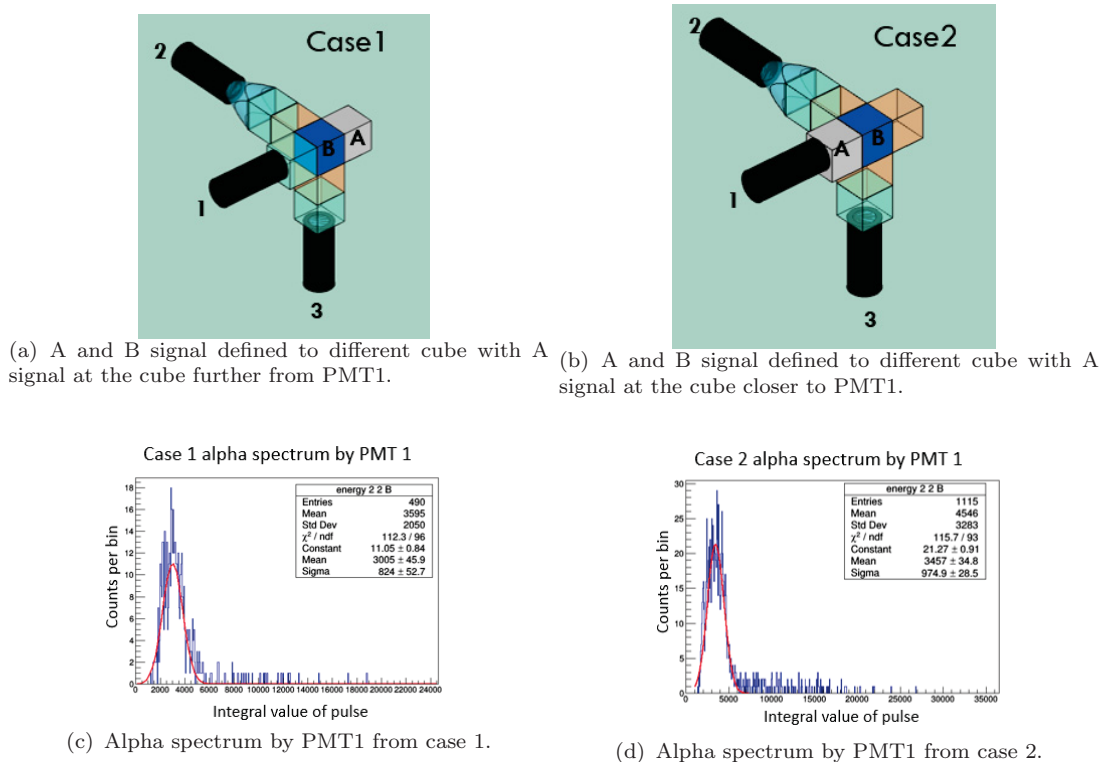
FIGURE 7.2: Analysis about signal of A an B on different cube.

The value of how much light is lost through one Li loaded cube is also measured by radon calibration introduced in chapter 6. Figure 7.2 shows how this test works and the result of it. Two sets of data were pick specifically as figure 7.2 (a) and (b) shows. By requiring prompt and delayed signals caught by different cubes, the position of the Bi-Po coincidence is well defined at a plane between these two cubes. Figure 7.2 (a) shows that the alpha signal defined by this geometry needs to go through 2 cubes to reach PMT1, however in the geometry in figure 7.2 (b), it only needs to go through one cube. The spectrum of signals from these two planes received by PMT 1 is shown in figure 7.2 (c) and (d). The mean value of the spectrum which signal need to go through two cubes is 3005, however in the case in which signal only needs to go through one cube the value is

3457. So this analysis shows that there is around a 14% light loss through one Li loaded cube.

This number is lower than what we got from the camera test, but not too far from it. The major concern about the light loss through each cube is because this property actually set a limitation to the volume NuLat detector can be. As explained in chapter 3, when we estimate the sensitivity of the detector, the volume of the detector is directly related to how good statistics we would reach. That's why in the estimation, we put a large scale like $10 \times 10 \times 10$ model or even $15 \times 15 \times 15$ model into the simulation. However, an actual detector with such big volume cannot have good energy resolution from each cube with this kind of light loss ratio. So at this point, this version of scintillator from Eljen has been shown to be not quite suitable for the NuLat detector. The similar conclusion has been drawn also by the light yield test we will explain in the next section.

7.2 Light Yield Difference between Li Loaded Cubes and Unloaded Cubes

We knew there was a different light yield from Li loaded and unloaded cubes. However, because of the two spectra shown in figure 7.3, we figure out that the difference is actually a serious issue for our neutrino detection.
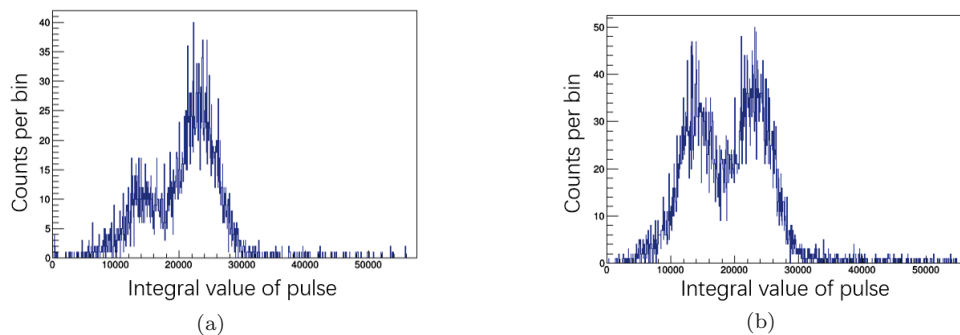
FIGURE 7.3: Figure (a) shows alpha spectrum from a analysis process that requires both prompt and delayed signals caught by the unloaded cubes, figure (b) shows alpha spectrum from a analysis process that only require delayed signal caught by the unloaded cubes.

Two spectra shown in figure 7.3 are from the same data set with different analysis processes. The geometry information about the data set used in figure 7.3 is shown in figure 7.4. This is just a regular Bi-Po test as we explained in chapter 6. As figure 7.4 shows,

the alpha spectrum we try to analysis is selected from a unloaded cube. The spectrum shown in figure 7.3 (a) comes from the analysis process that both prompt and delayed signals are required to be caught by the same cube. The spectrum shown in figure 7.3 (b) comes from the similar process, the difference is that only delayed signals are well defined in this cube. So the events picked up by the spectrum in 7.3 (a) have a better defined geometry than those picked by the spectrum in 7.3 (b).
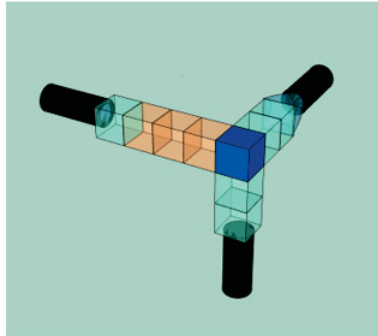
FIGURE 7.4: Geometry structure related to the data sets of figure 7.3.

There is clearly a big difference between these two spectra. There are two peaks shown in spectrum 7.3 (b), however, only the higher integral value position shown in spectrum 7.3(a) dominates. The other peak in 7.3 (b) becomes a small bump in spectrum 7.3 (a). A reasonable guess about this is that the peak located at higher integral value appeared in both spectrum is the actual alpha peak from the Bi-Po coincidence. The other peak shown in 7.3 (b) (corresponding to the bump in 7.3 (a)) is actually from other alphas created in the radon decay chain. Actually, within the radon decay chain, before the Bi-Po coincidence, there are three alphas emitted and the quenching effective energy of all these three alphas are around 400 keV. As we explained before, the effective energy of the alpha from Bi-Po coincidence is around 800 keV. Because these lower energy signals are from events with no temporal and spatial coincidence, that's why the peak becomes a lot smaller in 7.3 (a) when we have a better geometry requirement.

This guess is actually verified by a result we got earlier from a PSD test with radon source shown in figure (7.5). The hot spot located around 1000 on horizontal axis and 0.1 on the vertical axis is the spot related to alphas from Bi-Po coincidences. However, there is also a smaller spot besides it shown in the area which has similar vertical position. This is the signal from the other alphas in the radon decay chain just as explained. So these two different test actually are consistent with each other at this point. This test also shows
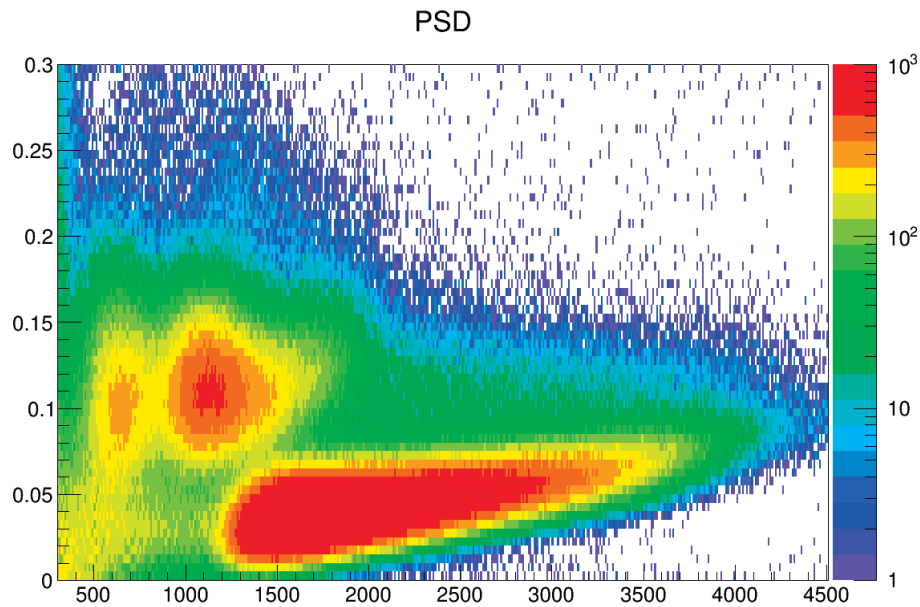
FIGURE 7.5: PSD result from Bi-Po coincidence test. The horizontal axis is the integral value of the pulse. The vertical value is the ration between the integral of the tail of the pulse to the integral of the entire pulse.

that the ROL concept and the geometry reconstruction ability NuLat has can actually reject a lot of background using its well defined geometry.

However, a problem revealed itself when we did a similar analysis on Li loaded cubes. We only get one peak as some results presented in chapter 6. The explanation of this finally goes to the different light yield between Li loaded cubes and unloaded cubes. The guess is that the light yield of Li loaded cube is so low that the alphas with effective energy around 400 keV cannot be detected. This guess may not be far from the truth. The pulse height responding to the alpha signal from Bi-Po sometimes can be as low as 50 which is already very close to the base line. Recall that when we introduce the process of neutron capture by ^6Li, the effective energy which can be detected is around 400 keV. So the phenomenon that the current version of the detector has trouble to detecting these background alphas from radon decay shows it could have a similar problem dealing with the neutron capture signal.

The analysis of the actual light yield difference between these two kind of cubes is shown in figure 7.6. The same PMT is picked to avoid any gain matching confusion between different PMTs. A Li loaded cube and an unloaded cube are picked to be neighbors to each other and align with this PMT. The peak position of the alpha spectrum from the Li loaded cube is around 2000, however in the spectrum from unloaded cube, the peak
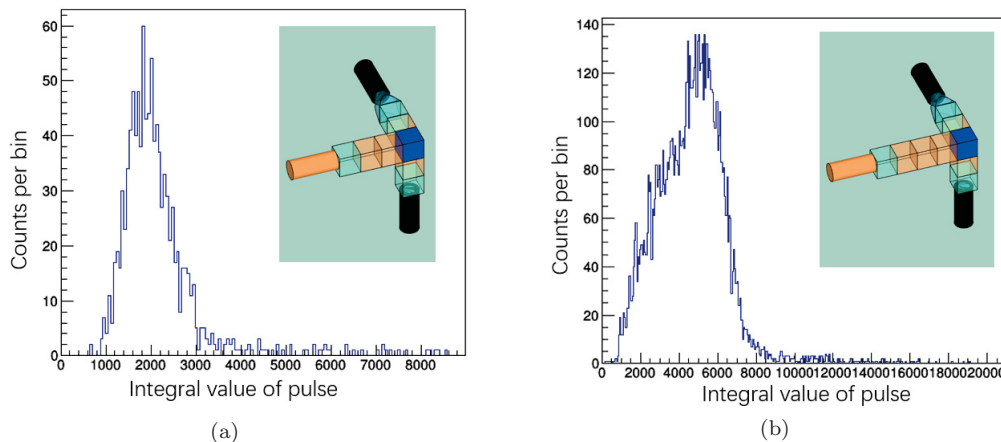
FIGURE 7.6: Light yield comparison between Li loaded and unloaded cubes. The spectrum are from PMT marked as yellow in the graph. (a) has the geometry that alpha signal being detected is from Li loaded cube located three cubes away from this PMT. (b) has the geometry that alpha signal being detected is from unloaded cube located four cubes away from this PMT.

position is actually around 5000, even though there is one more cube that photons need to pass through from this cube compared to the Li loaded one. This analysis shows that there is at least 60% difference of light yield between these two kind of cubes.

So similar to the conclusion we obtained from the last section, there is a necessary improvement we should make for the scintillator used by the next version of NuLat detector.

One option we have is using liquid scintillator like Ultima Gold AB instead of solid version we currently have. The liquid scintillator can be filled into a cubic shape acrylic box which sealed perfect so liquid will not be able to leak out. Teflon films can be used to create barriers we need for the ROL requirement. A proper arrangement of Teflon films can form the small cell so that the structure of the liquid version NuLat detector have each cell with Ultima Gold AB and the barriers between them are Teflon films. The refractive index of Ultima Gold AB and Teflon films are 1.56 and 1.34, based on the simulation we introduced in chapter 3, we should still be able to do effective geometry reconstruction with these kind properties. One of the benefits of liquid scintillator is that we can control the Li loading ratio based on our requirement. Lower the loading ratio can increase the light yield and transparency of each cell. Although there is also negative side of lower the Li loading ratio, it means the average time of the neutron capture will be longer compared to the current version which will reduce the signal to background ratio, that's why some actual tests need to be done to verify what kind of ratio is best for our purpose.

Besides the improvement of scintillators, there is another simple improvement we can make for the current version of the NuLat detector. As shown before, we have only 25 light guides mounted in the current detector. Our collaborators are currently working hard making another 50 for this detector. With all the PMTs mounted with light guides, a better light collection might help the low light yield issue from Li loaded cubes. Although in the long run, a better scintillator material need to be defined for sure.

Chapter 8

Conclusion

Significant assembly and calibration work has been done with the current version of the NuLat detector. The advantage of ROL based detector to reject background is verified by the radon calibration result as discussed in chapter 7. The energy mapping we showed in chapter 6 also shows low cross talk of the current NuLat detector, so the light channeling ability and geometric reconstruction ability are all verified by these tests. With the AB trigger mode on mTC DAQ, both prompt and delayed spectrum from Bi-Po coincidence have been analyzed and the values are consistent with the prediction, so that the basic trigger mode can be used for IBD is verified at this point.

On the other hand, low light yield from the current version ^6Li loaded plastic scintillator and the high light loss rate shown in the measurement are crucial issues which need to be fixed for next version of the NuLat detector. The potential solutions are having light guide fully mounted to increase the light collection ability and searching for the new type of scintillator and with lower ratio of ^6Li doping. The liquid scintillator like Ultima Gold AB with Teflon films work as the barriers may be a good candidate for the next version of the NuLat detector.

Another topic is the improvement of the firmware currently running on the mTC DAQ. As introduced in Chapter 6, the current firmware cannot define the geometry of the signal by itself. So we have to deal with the issue by some advanced triggering methods coupled with some software analysis. These problems can potentially be solved by a re-design of the firmware in the near future. The background rate can be greatly reduced if the DAQ can do a preliminary check for spatial coincidence of prompt and delayed signals, so only the events having these two signals happen in the same or neighboring cube can

be triggered. Also by requiring a range that only the number of PMTs get signals fall into this range can fire a trigger, it can help reject background signals effectively.

Bibliography

[1] K. Nakamura and S.T. Petcov (particle data group). Neutrino mass, mixing, and oscillations. June 2016. URL http://pdg.lbl.gov/2017/reviews/rpp2016-rev-neutrino-mixing.pdf.

[2] Fumihiko Suekane. Neutrino oscillations: A practical guide to basics and applications. April 2015.

[3] John N. Bahcall and Aldo M. Serenelli. New solar opacities, abundances, helioseismology, and neutrino fluxes. *The Astrophysical Journal*, 2005.

[4] B.T. Cleveland et al. Measurement of the solar electron neutrino flux with the homestake chlorine detector. *Astrophys J. 496, 505*, 1998.

[5] SNO Collaboration. Measurement of the e and total 8b solar neutrino fluxes with the sudbury neutrino observatory phase i data set. *Phys.Rev.C75:045502,2007*, 2006.

[6] super-kamiokande collaboration. Evidence for oscillation of atmospheric neutrinos. *Phys. Rev. Lett. 81*, 1998. URL https://journals.aps.org/prl/abstract/10.1103/PhysRevLett.81.1562.

[7] SK collaboration. Evidence for an oscillatory signature in atmospheric neutrino oscillations. *Phys. Rev. Lett. 93, 101801*, 2004.

[8] K2K collaboration. K2k beam line. URL http://neutrino.kek.jp/Images/Figures/nubeam.gif.

[9] N.Baker et al. *Phys. Rev. D25, 617*, 1982.

[10] K2K collaboration. Measurement of neutrino oscillation by the k2k experiment. *PRD 74, 072003*, 2006. URL https://arxiv.org/pdf/hep-ex/0606032.pdf.

[11] K.Eguchi et al. First results from kamland: Evidence for reactor antineutrino disappearance. *Phys. Rev. Lett. 90, 021802*, 2003. URL https://journals.aps.org/prl/abstract/10.1103/PhysRevLett.90.021802.

[12] KamLAND Collaboration. Reactor on-off antineutrino measurement with kamland. *arXiv:1303.4667*, 2013.

[13] KamLAND Collaboration. Reactor on-off antineutrino measurement with kamland. 2013. URL https://arxiv.org/abs/1303.4667.

[14] G. Mention et al. The reactor antineutrino anomaly. *PHYSICAL REVIEW D 83, 073006*, 2011.

[15] M. Laveder Y.F. Li S. Gariazzo, C. Giunti. Updated global 3+1 analysis of short-baseline neutrino oscillations. *arXiv:1703.00860 [hep-ph]*, 2017.

[16] N. Haag and A. Gtlein et al. Experimental determination of the antineutrino spectrum of the fission products of 238u. *10.1103/PhysRevLett.112.122501*, 2013.

[17] Patrick Huber. On the determination of anti-neutrino spectra from nuclear reactors. *Phys.Rev.C84:024617,2011*, 2011.

[18] The antineutrino energy structure in reactor experiments. *arXiv:1512.03366*, Dec 2015. URL https://arxiv.org/abs/1512.03366.

[19] C Mariani. Review of reactor neutrino oscillation experiments. *Mod.Phys.Lett. A27 (2012) 1230010*, 2012. URL arXiv:1201.6665.

[20] Steven Derek Rountree. Using diode lasers for atomic physics. May 2010. URL https://vtechworks-lib-vt-edu.ezproxy.lib.vt.edu/bitstream/handle/10919/27803/Rountree_SD_D_2010.pdf?sequence=4&isAllowed=y.

[21] Joachim Kopp and Pedro A.N. et al. Sterile neutrino oscillations: The global picture. *JHEP 1305:050, 2013*, 2013.

[22] Zachary W Yokley. Solar and sterile neutrino physics with the raghavan optical lattice. June 2016. URL https://vtechworks-lib-vt-edu.ezproxy.lib.vt.edu/handle/10919/71330.

[23] V.A. Li and R. Dorrill et al. Invited article:minitimecube. *Rev. Sci. Instrum. 87, 021301 (2016)*, 2016.

[24] Hamamatsu Company. Pmt data sheet.

[25] Russell R. Mammei. Thin films for the transport of polarized ultracold neutrons for fundamental symmetry study. 2010. URL https://arxiv.org/abs/nucl-ex/0512041.

[26] Srubabati Goswami et al. Probing the mass hierarchy via atmospheric + survival rates in megaton water cerenkov detectors. *Nucl. Phys B143*, Aug 2005. URL https://arxiv.org/pdf/hep-ph/0506145.pdf.

[27] SNO collaboration. Combined analysis of all three phases of solar neutrino data from the sudbury neutrino observatory. *PHYSICAL REVIEW C 88, 025501*, 2013.

[28] SK collaboration. Atmospheric neutrino oscillation analysis with subleading effects in super-kamiokande i, ii, and iii. *Phys. Rev. D 81, 092004*, 2010.

[29] T2K Collaboration. First muon-neutrino disappearance study with an off-axis beam. *Physical Review D 85, 031103(R) (2012)*, 2012.

[30] Marcela Batkiewicz. Latest results from t2k. 2017. URL https://arxiv.org/abs/1705.04277.

[31] H. Furuta T.J.C. Bezerra and F. Suekane. A global fit determination of effective δm_{31}^2 from baseline dependence of reactor $\bar{\nu}_e$ disappearance. 2013. URL https://arxiv.org/pdf/1304.6259.pdf.

[32] A. Aguilar and L.B. Auerbach et al. Evidence for neutrino oscillations from the observation of electron anti-neutrinos in a muon anti-neutrino beam. *Phys.Rev.D64:112007,2001*, 2001. URL https://arxiv.org/abs/hep-ex/0104049.

[33] MiniBooNE Collaboration. Unexplained excess of electron-like events from a 1-gev neutrino beam. *Phys.Rev.Lett.102:101802,2009*, 2009. URL https://arxiv.org/abs/0812.2243.

[34] MiniBooNE Collaboration. Event excess in the miniboone search for $\bar{\nu}_\mu \to \bar{\nu}_e$ oscillations. *Phys.Rev.Lett.105:181801,2010*, 2010. URL https://arxiv.org/abs/1007.1150.

[35] GALLEX Collaboration. Final results of the ^{51}cr neutrino source experiments in gallex. *Physics Letters B Volume 420, Issues 12*, 1998. URL http://www.sciencedirect.com/science/article/pii/S0370269397015621#!

[36] SAGE Collaboration. Measurement of the response of a ga solar neutrino experiment to neutrinos from an 37ar source. *Phys.Rev.C73:045805,2006*, 2006. URL https://arxiv.org/abs/nucl-ex/0512041.

[37] M.Laveder. Unbound neutrino roadmaps. *Nuclear Physics B - Proceedings Supplements Volume 168, June, Pages 344-346*, 2007.

[38] Marco Laveder Carlo Giunti. Short-baseline active-sterile neutrino oscillations? *Mod.Phys.Lett.A22:2499-2509*, 2006.

[39] Marco Laveder Carlo Giunti. Statistical significance of the gallium anomaly. *Phys.Rev.C83:065504*, 2011.

[40] Y.F. Li Q.Y. Liu H.W. Long C. Giunti, M. Laveder. Update of short-baseline electron neutrino and antineutrino disappearance. *Phys.Rev. D86 (2012) 113014*, 2012.

[41] Super-Kamiokande Collaboration. Solar neutrino measurements in super-kamiokande-iv. *arXiv:1606.07538 [hep-ex]*, 2016.

[42] Borexino Collaboration. Final results of borexino phase-i on low energy solar neutrino spectroscopy. *Phys. Rev. D 89, 112007 (2014)*, 2014.

[43] Libby McCutchan et.al Anna Hayes, Gerard Jungman. Analysis of the daya bay reactor antineutrino flux changes with fuel burnup. *arXiv:1707.07728*, 2017.

[44] S. B. Kim. New results from reno,. *Proceedings of the 25th International Conference on Neutrino Physics and Astrophysics (Neutrino 12), Kyoto, Japan*, 2012.

[45] S. B. Kim. Observation of reactor electron antineutrino disappearance at reno,. *Nuclear Physics BProceedings Supplements, vol. 235236*, 2013.

[46] S.-H. Seo. New results fromreno and the 5mev excess. *AIP Conference Proceedings, vol. 1666*, 2015.

[47] H. de Kerret. Results from double chooz. *Proceedings of the 26th International Conference on Neutrino Physics and Astrophysics*, 2014.

[48] Recent results from daya bay. *Proceedings of the 16 International Workshop on Neutrino Telescopes, Venice, Italy, March 2015*, 2015.

[49] KarstenKossert. Measurementofwavelength-dependent refractive indices of liquid scintillation cocktails. *Applied Radiation and Isotopes82(2013)382388*, 2013.

[50] Robert D. Cousins Gary J. Feldman. A unified approach to the classical statistical analysis of small signals. *Phys.Rev.D57:3873-3889,1998*, 1999.

[51] K. M. Heeger and B. R. Littlejohn et al. Experimental parameters for a reactor antineutrino experiment at very short baselines. *10.1103/PhysRevD.87.073008*, 2012.

[52] K.A.Olive et.al. Review of particle physics. *Chin.Phys.vol.C38,p.090001*, 2014.

[53] Robert D. Cousins Gary J. Feldman. A unified approach to the classical statistical analysis of small signals. *10.1103/PhysRevD.57.3873*, 1998.

[54] P. Vogel* and J. F. Beacom. Angular distribution of neutron inverse beta decay. *PHYSICAL REVIEW D, VOLUME 60, 053003*, 1999.

[55] R10533 data sheet. 2015. URL https://www.hamamatsu.com/jp/en/R10533.html.

[56] ELJEN. Ej-254 data sheet.

[57] The ice radio sampler (irs) is a descendant of the buffered labrador series of asics, and was originally designed for performing radio searches for ultra-high energy neutrinos using antennas embedded in antarctic ice.

[58] B.Dey and M.Borsato et al. Design and performance of the focusing dirc detector. *arXiv:1410.0075*, 2014. URL https://arxiv.org/abs/1410.0075.

[59] K. Bechtol and S. Funk et al. Target: A multi-channel digitizer chip for very-high-energy gamma-ray telescopes. *arXiv:1105.1832*, 2012. URL https://arxiv.org/abs/1105.1832.

[60] P. Allison and J. Auffenberg et al. Design and initial performance of the askaryan radio array prototype eev neutrino detector at the south pole. *arXiv:1105.2854*, 2012. URL https://arxiv.org/abs/1105.2854.

[61] A.Pocar. Low background techniques and experimental challenges for borexino and its nylon vessels. *PHD thesis*, 2003. URL https://inspirehep.net/record/637851/files/A.Pocar_PhD_Thesis.pdf.

[62] Pylon Electronics. Rn-2015/th-2015/rnc flow-through radon source datasheet. 2003.

[63] Steve Hardy. Measuring the 7be neutrino flux from the sun:calibration of the borexino solar neutrino detector. *PHD thesis*, 2010.

[64] J.Matthews etc. J, J. Beatty. Cosmic rays. *particle data group*, 62:1–21, 2011. URL http://pdg.lbl.gov/2011/reviews/rpp2011-rev-cosmic-rays.pdf.

[65] H.Bichsel etc. Passage of particles through matter. *particle data group*, 32:1–32, 2014. URL http://pdg.lbl.gov/2014/reviews/rpp2014-rev-passage-particles-matter.pdf.

[66] K. P. Hickerson and X. Sun et al. First direct constraints on fierz interference in free neutron decay. 2017. URL https://arxiv.org/abs/1707.00776.

[67] R. W. Pattie Jr. and N. B. Callahan et al. Measurement of the neutron lifetime using an asymmetric magneto- gravitational trap and in situ detection. 2017. URL https://arxiv.org/abs/1707.01817.

[68] M. P. Mendenhall and R. W. Pattie Jr et al. Precision measurement of the neutron beta-decay asymmetry. 2017. URL https://arxiv.org/abs/1210.7048.

[69] L. J. Broussard and B. A. Zeck et al. Detection system for neutron decay correlations in the ucnb and nab experiments. 2017. URL https://arxiv.org/abs/1607.02656.

[70] A. Saunders and M. Makela et al. Performance of the los alamos national laboratory spallation-driven solid-deuterium ultra-cold neutron source. *Rev.Sci.Instr.84, 013304*, 2013. URL http://neutron.physics.ncsu.edu/UCNA/protected/RevSciInstrum_84_013304.pdf.

[71] M. A.-P. Brown and E.B. Dees et al. New result for the neutron -asymmetry parameter a0 from ucna. *arXiv:1712.00884*, 2017.

[72] C. L. Morris et al. A new method for measuring the neutron lifetime using an in situ neutron detector. *arXiv:1610.04560*, 2016.

[73] T. M. Ito and R. Adamek et al. Performance of the upgraded ultracold neutron source at los alamos national laboratory and its implication for a possible neutron electric dipole moment experiment. *arXiv:1710.05182*, 2017.

[74] S. B. Treiman J. D. Jackson and Jr. H. W. Wyld. Possible tests of time reversal invariance in beta decay. *Physical Review, 106(3):517521*, 1957. URL https://journals.aps.org/pr/pdf/10.1103/PhysRev.106.517.

[75] John Robertson. Mechanism of sp3 bond formation in the growth of diamond-like carbon. *Diamond and Related Materials,14:942948*, 2005.

[76] R.W. Pattie Jr et.al. Evaluation of commercial nickel-phosphorus coating for ultra-cold neutron guides using a pinhole bottling method. *arXiv:1703.00508*, 2017.

[77] Z. Tanga et al. Measurement of spin-flip probabilities for ultracold neutrons interacting with nickel phosphorus coated surfaces. *arXiv:1510.06490v3*, 2016.

Appendix A

Guide Coating for UltraCold Neutrons Experiment

In this chapter, we introduce a new topic. Although it is unrelated to the NuLat detector, a lot of work was done over the last six years on this topic, resulting in numerous publications with Xinjian Ding as co-author[66–73]. This topic is mainly about the guide coating development for ultracold neutrons (UCN) transportation. UCN have energies below 300 neV which give it the name "ultracold" neutron. Many experiments to use these unique UCNs to do different measurements for various physics motivations. Our work at Virginia Tech (VT) was to develop a reliable method to manufacture effective guide system so ultracold neutrons can be transported from source to the detection area without too much loss and with stable physics status like the spin state of the neutrons. Since its an unrelated topic to NuLat, we just briefly introduce some important content related to this topic. We start with the actual UCN experiments our guides and source part are being used for. Then we introduce the physics idea behind the guide coating and how we make it happen in real life.

A.1 Introduction About UCN Related Experiment At Los Alamos National Lab (LANL)

The UCN experiment area is located at LANL TA-53, Neutron Science Center. Figure A.1 shows the diagram of how the research area looks like at LANL. Spallation neutrons from the 800 MeV proton accelerate impinging on a tungsten target are fed into the solid

deuterium UCN source[70] and produce UCN via down-scattering. This part is shown at the left part of figure A.1. The solid deuterium needs to be made by a cooling process until it reach 4K temperature. After that, UCN will be guided by the guides we made to different research areas. The major benefit of this kind of UCN source is that UCN can be 100% polarized. This makes it really useful for different measurements needing a controllable spin state of the neutrons. In the area, there are several apparatus related to this spin control work, like the PPM (pre-polarized magnets) and the AFP (Adiabatic Fast Passage). These apparatus all contain super conduct material which also needs to be run at 4K temperature.
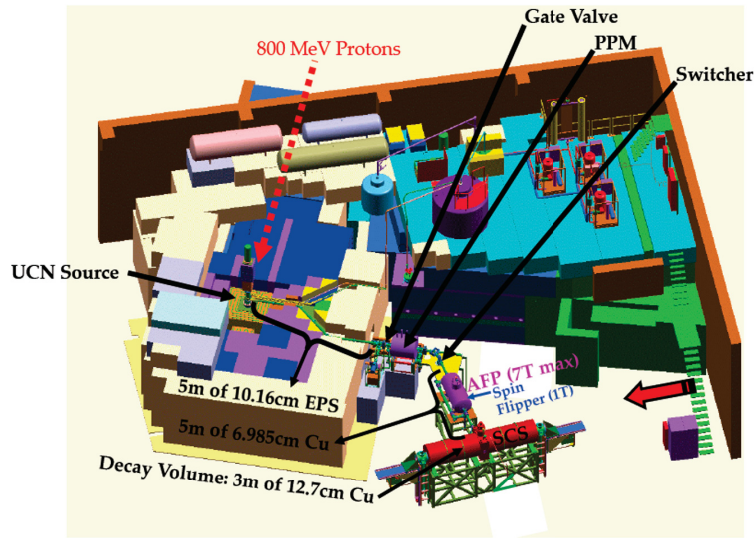
FIGURE A.1: Diagram of UCN research area at LANL.

The expression of beta decay rate is deduced by Jackson et al.[74] as shown in equation A.1.

$$
\begin{aligned}
dW \propto\ & G_F^2 V_{ud}^2 (g_v^2 + 3g_a^2) F(E_e) dE_e d\Omega_e d\Omega_{\bar\nu} \\
& \times \left[1 + a\frac{\vec{p_e}\vec{p_{\bar\nu}}}{E_e E_{\bar\nu}} + b\frac{m_e}{E_e} + <\vec{\sigma_n}> \left(A\frac{\vec{p_e}}{E_e} + B\frac{\vec{p_{\bar\nu}}}{E_{\bar\nu}} + D\frac{\vec{p_e}\times\vec{p_{\bar\nu}}}{E_e E_{\bar\nu}} \right) \right] .
\end{aligned}
\tag{A.1}
$$

G_F is the Fermi constant. V_{ud} is first component from the CKM matrix. $g_{\bar\nu}$ and g_a are respectively the vector and axial-vector factor that corresponds to one possibility for a Lorentz invariant coupling. F_{E_e} is the Fermi function which gives the allowd shape of the energy spectrum. E_e and $E_{\bar\nu}$ are related to the energy of electron and anti-neutrino.

E_e and $E_{\bar{\nu}}$ are related to the mass of electron and anti-neutrino. $\vec{\sigma}_n$ is the neutron spin. Beta decay observables a, A, b, B and D are called correlation coefficients. Different detectors are designed for measuring these observables with the UCN source. These experiments are named after what coefficient they designed to measure like UCNA, UCNB and UCNb. Also there is an experiment designed for measuring the life time of neutorn named UCN-tau. Since it is just a brief introduction, I will not discuss too much about these experiments. More detail can be found from Ref[66–69].
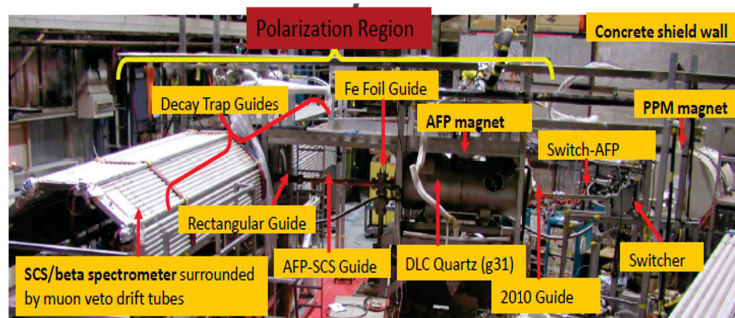
FIGURE A.2: Picture about part of guide system at UCN research area.

Figure A.2 shows part of the guide system mounted at the UCN research area at LANL. These guides are named by different purposes they serve. All these guides can be categorized into three groups. Stainless Steel coated with ^{58}Ni by EBeam (electron beam) evaporation are mostly used for UCN source. Copper and Quartz coated with diamond like carbon (DLC) are mostly used for UCN transportation and decay. Quartz tube is specifically picked to be used in the region where radiation needs to penetrate to act on the neutron's spin.

FIGURE A.3: The coating chamber located at Virginia tech.

Most of these guides were made in the chamber at VT shown in figure A.3. In the next 3 section, I will briefly introduce the physics idea about guide development and what kind of method we used to do actual coating in this chamber.

A.2 Theory of Neutron Interaction With Materials

As shown in the previous section, there are long journeys from where the UCN were created to the detection area. Except for the complicated geometry, there are also designated special areas for fully polarizing UCN and picking neutrons with right spin status. All these make it extremely important that we have proper equipment to guide UCNs from source area to the detection area with high efficiency. The way to achieve this relies on the physics of interaction between UCN and the surface it hits. The detailed logic behind the physics will be omitted here, but the idea can be simplified as figure A.4 shows.
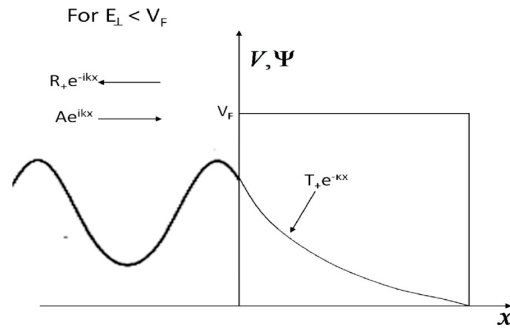
FIGURE A.4: Wave function of a particle reflected from a material surface represented by a step in potential energy.

This is just a simple quantum mechanics model about a wave function hitting a potential step which has higher energy than the wave function itself. The probability of refection and transmission is determined by the height of this potential step. This model and related computations can be found in any quantum mechanics book. The potential energy V_F here is what we call the Fermi potential, which is defined as follows

$$V = \frac{2\pi\hbar^2}{m} Na \ , \tag{A.2}$$

where a is the scattering length which depends on what atoms interacts with UCNs, and N is the number density in the material. In addition to the effective Fermi potential,

there are also other factors which might cause the loss of UCNs during the interaction. It might be that the UCNs are absorbed by the material, or it could be that there is inelastic up-scattering which results in greater energy of UCNs than the Fermi potential. The simple way to fix this in our calculation is to make a replacement of Fermi potential V_F to a complex form $U = V_F - iW$. The new imaginary part iW represents the loss factors of interaction between UCN and the material of surface. With this simple quantum model and defined materials, we can easily have a pretty accurate prediction about the probability of reflection and transmission related to the surface with a specific structure and different energy of UCNs.
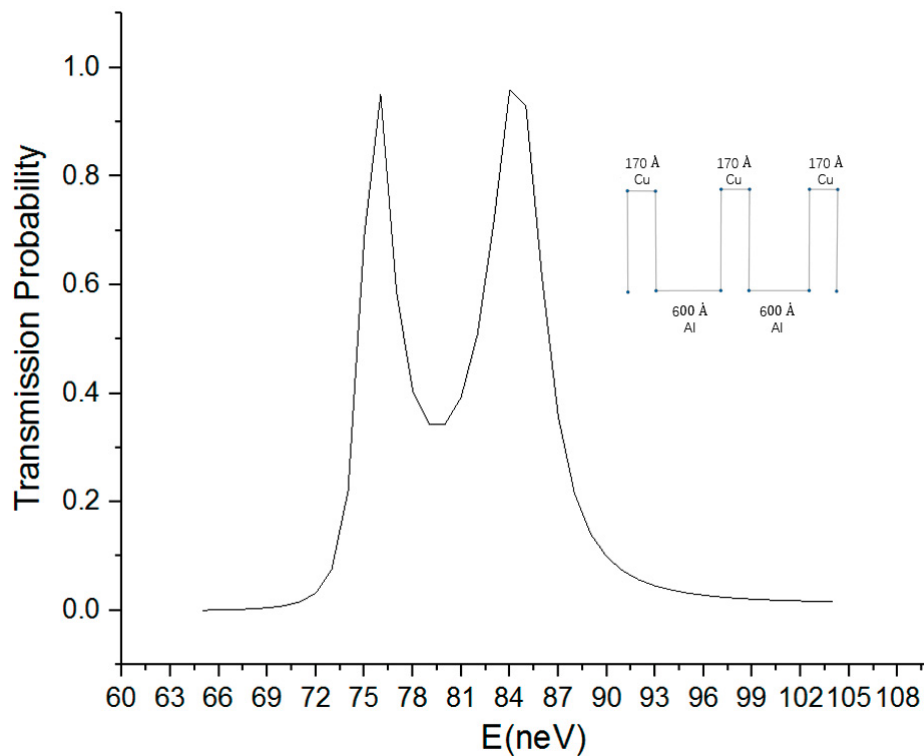
FIGURE A.5: An example of multilayer films which were designed to have a resonance like effect on transmission of certain energies of UCNs.

Figure A.5 is an example showing different transmission probabilities of UCN of various energies when they hit the surface with same structure. This complicated structure is composed of 3 layer Cu with 170 $\mathring{A}$ and 2 layer Al with 600 $\mathring{A}$ thickness. This specific multilayer film was designed intentionally to let neutrons with energy around 76 neV and 86 neV all being transmitted, but neutrons with all the other energies below 100 neV being reflected.

Material	$V_F(neV)$	Prob.loss/bounce (10^{-5})	Prob.spin flip/bounce (10^{-6})
^{58}Ni	346	5	5×10^5
316L Stainless Steel	183	< 100	4000
Cu	170	15	1
Quartz	90	59	14
Be	250	7.1	7.2
PLD DLC	220-270	< 1	2

TABLE A.1: Materials suitable for UCNs transportation with different purpose.

The design of coating systems and the material we should use is predicted by the same computation. Potential materials suitable for our UCNs transportation requirement are listed as Table A.1.

Some materials like ^{58}Ni have really good Fermi potentials which seems pretty good for our transportation purpose. However, since it is a magnetic material and most of the UCN related experiments require stable polarization status during transportation, so we only use this material around the source area. The most common surface we used for the transportation is diamond like carbon (DLC) coated by pulsed laser deposition (PLD) inside Cu or Quartz tubes. The reason to choose this material is because the high Fermi potential and low spin flip probability it has as listed in the table A.1.

A.3 Pulse Laser Deposition System For Diamond Like Carbon (DLC)

As explained before, the reflection probability of neutrons is highly depends on the Fermi potential of the surface it hits. We designed our system to work with carbon deposition to form a suitable surface for high reflection probability, since the scattering length, a, is predefined by carbon atoms, so the only way we can increase the Fermi potential is to raise the density of the carbon films. That is the major reason we try to form more sp^3 hybridization structures instead of sp^2 during our deposition process and call the structure diamond like carbon (DLC).

Besides higher ratio of sp^3 hybridization structure in our carbon films, we also wanted to estimate how thick our film should be. So we did a computation as explained in the last section with basic quantum mechanics. The result shown in figure A.6 shows clearly
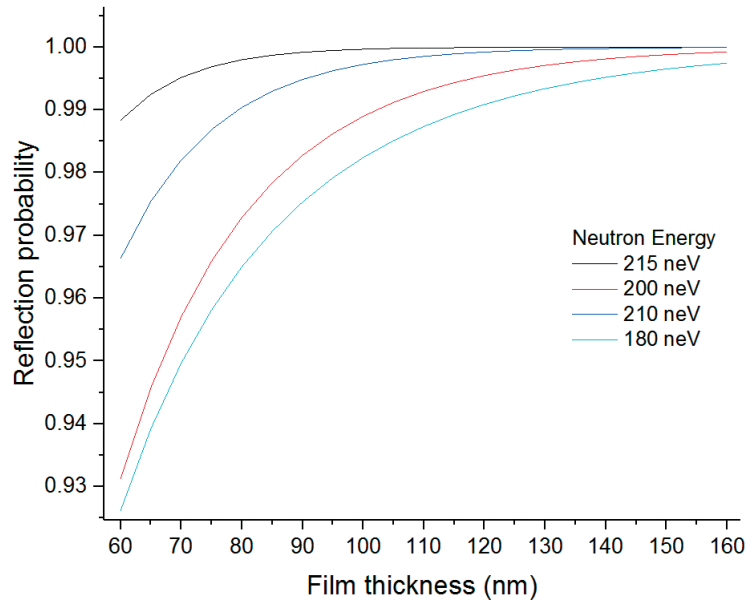
FIGURE A.6: A computation to estimate the effect of thickness of film to the reflection probability of UCN.

that when the film has a thickness above 150 nm, as long as energy of neutrons are below the Fermi potential of the film, the probability of reflection are all close to 100%. So during our coating process, we always target 150 nm as our thickness. Although in reality, there are some compromises we have to contend with about thickness and ratio of sp^3 hybridization structure. More dense carbon atoms and thicker films actually directly relate to more stress within the carbon films and higher potential risk of delamination. So we have to keep a balance between good quality coatings and stability of films for long term usage.

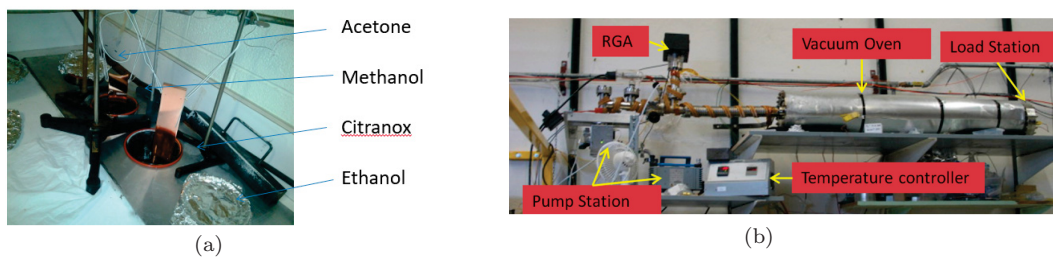FIGURE A.7: Cleaning system for guide coating[25] .

There are several different cleaning processes before actual deposition work. Figure A.7 shows a picture of our cleaning apparatus. All the guides to be coated should go through different chemical baths first with an ultra-sonic cleaning system. The regular cleaning time in each chemical liquid is around 10 minutes. After these processes, guides would be

placed into a chamber to be baked in a high temperature vacuum environment. Typically this baking process is set to be 200 $°C$ for 24 hours and then 350 $°C$ for 24 hours. After these processes, guides are ready to be mounted into the coating chamber and go through the actual deposition process.
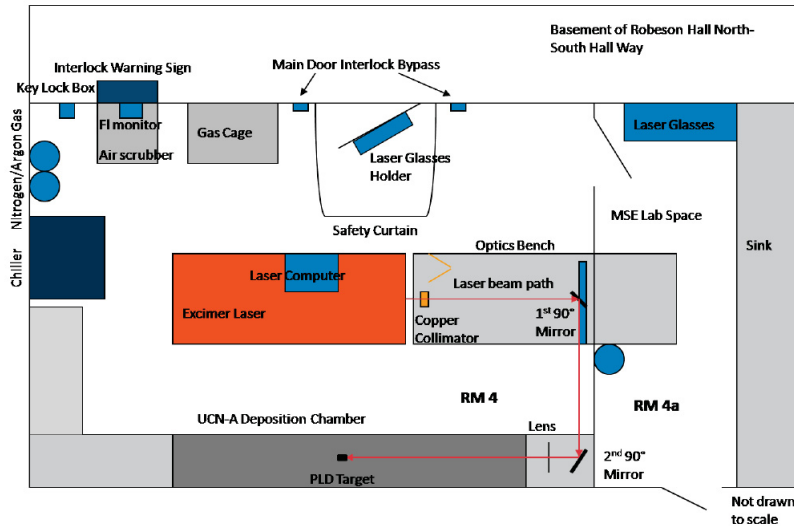

FIGURE A.8: Diagram of the laser, Gas Cage, optics and deposition chamber in the coating area. [25]

Figure A.8 shows a bird's eye view of the room having the apparatus for pulsed laser deposition (PLD) coating work. There are different gas bottles for laser filling and chamber venting in the room. One chiller should be kept running for cooling the laser. The laser beam should be guided by the optics from the output port until it is focused and hits the exact position of the target we want it to be.

The mechanism of sp^3 bond formation can be summarized as a subplantation process. [75] During the deposition of carbon film, the initial film will contain high ratio of sp^2 structure. As the deposition keeps going, high energy carbon ions will penetrate into the surface layer and enter a subsurface interstitial site, where the resulting increased density causes it to take on the metastable sp^3 configuration. Detailed modeling and simulation can be found in Ref[75]. Currently we use the LPX-300 as our laser to create high energy carbon ions ($\sim$ 100 eV). It can create laser pulses at wavelength 248 nm with intensity from 300 mJ to 1 J. The laser is shown in figure A.9.

Figure A.10 shows a diagram explaining how the apparatus is related to actual DLC deposition are organized. The laser beam focused by a lens goes through the port from the left and hits the carbon target located around the middle of the chamber. The energy of carbon ions is estimated by an ion probe located on the middle top of the chamber with

FIGURE A.9: Laser used for DLC deposition.
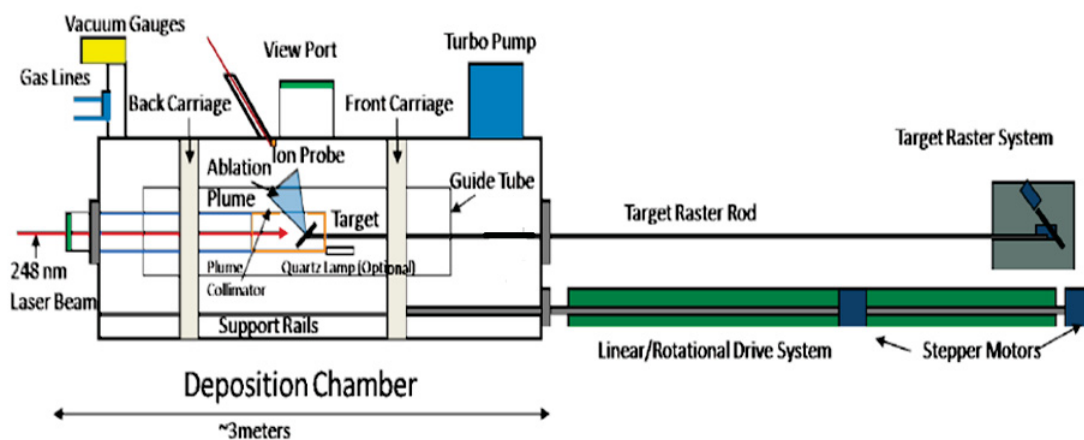
FIGURE A.10: Structure of all the apparatus related to actual deposition process.

a time of flight (TOF) measurement. There are two drive systems running independently during the coating. One drive system controls the movement of the carbon target. It drives the carbon target to move in a small elliptical shape which can avoid the condition that the focused laser beam keep hitting the same point of the target. The other drive system controls the movement of the guide cage. It can drive the cage to move forward or backward with a fixed rotation speed. This allows stable movement of the guide during the coating to form a uniform film.

Figure A.11 shows a CAD diagram of the coating chamber with target and guide being mounted properly. There is a copper tube with around $1 - 3/4''$ diameter pre-mounted in

(a)

(b)

(c)

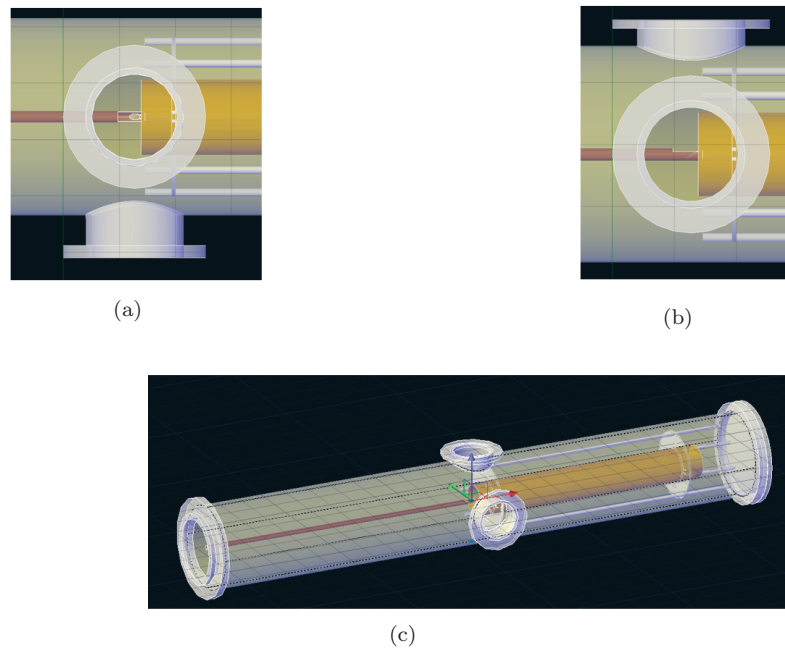FIGURE A.11: A CAD sketch of the DLC coating system. (a) is the view of the chamber from the top window on the chamber. A carbon target can be seen located in the opening of the center tube. (b) is a side view of this structure. The angle of the surface of carbon target is tilted around 30° and can be seen from this view. (c) shows a general view of this coating system. A tube needing to be coated is mounted in a frame which we called the guide cage. It can drive this tube forward or backward with a fixed rotation speed.

the chamber from the input end of the laser beam to the center of the chamber. This thin tube serves different purposes like keeping the carbon dust during the coating process and holding the quartz lamp for EBeam evaporation deposition which will be discussed in the next section. The carbon target should be held inside this tube at the proper position so it faces an opening on the top. When a guide needs to be coated, move it though this area and the carbon ion ablated by the laser beam will be deposited into the inside wall of the guide.

Some examples of the finished guide DLC coating are shown in figure A.12. These figures are picked to show different materials and shapes of guides passing through this DLC deposition process. Figure A.12 (a) shows the coating on the inside wall of a 5 inch diameter copper tube. Figure A.12 (b) shows the coating on a copper plate. Four coated plates will be assembled into a square shaped guide finally. Figure A.12 (c) shows the coating on the inside wall of a $2-3/4''$ quartz tube. These figures also show the structure of the guide cage actually running during the coating.
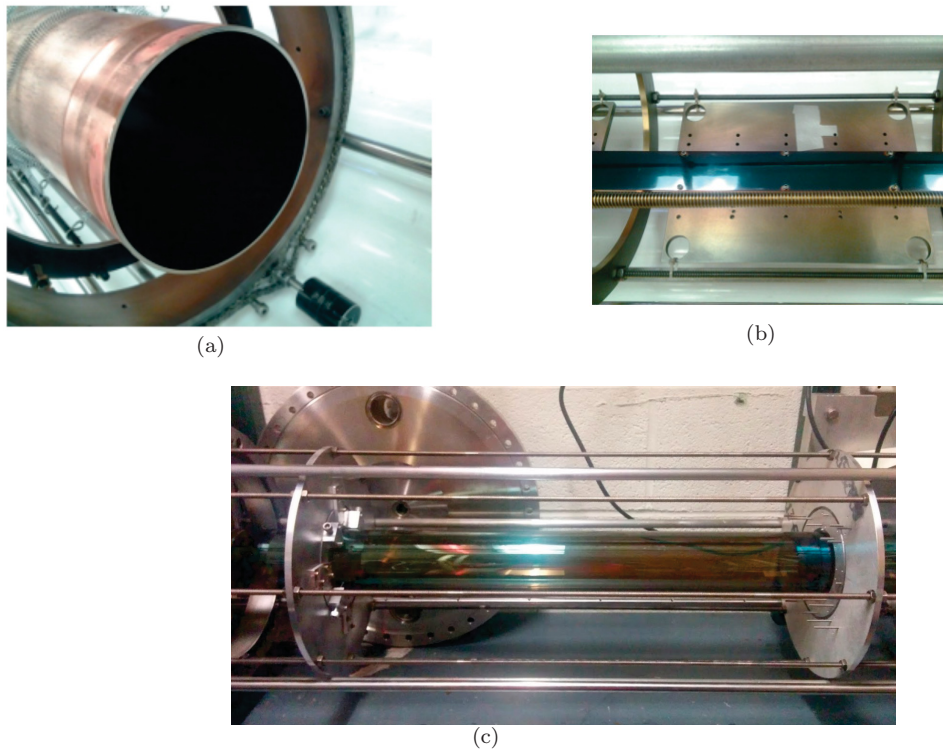
(a)

(b)

(c)

FIGURE A.12: Some picture of coated guides are presented in this figure. Figure (a) is a 5 inch diameter decay trap guide mounted in the SCS region as figure A.2 shows. It is the major detection area for UCNA and UCNB detector. Figure (b) is a piece of plate coated by DLC. There are four pieces of plate coated and assembled to form a rectangular shaped guide. This rectangular guide connects the input port of decay trap to down stream of the AFP as figure A.2 shows. Figure (c) is a 2-3/4" inch quartz guide coated by DLC for the UCN-tau Experiment.

(a)

(b)

FIGURE A.13: Figure (a) is the picture of witness strip wrapped with aluminum foil. Figure (b) is the picture of witness strip after deposition process. There is a clear edge separate the surface coated and uncoated.

To understand the films being coated on these guides, we also put some witness strips with the guide when it is mounted to the guide cage. The example of the witness strip is shown in figure A.13. It is made from a silicon wafer covered by a piece of aluminum foil. As figure A.13 (a) shows, only part of the silicon wafer will be coated during the deposition process. There will be a clear edge because of this to separate the area of coated and uncoated clearly as figure A.13 (b) shows.
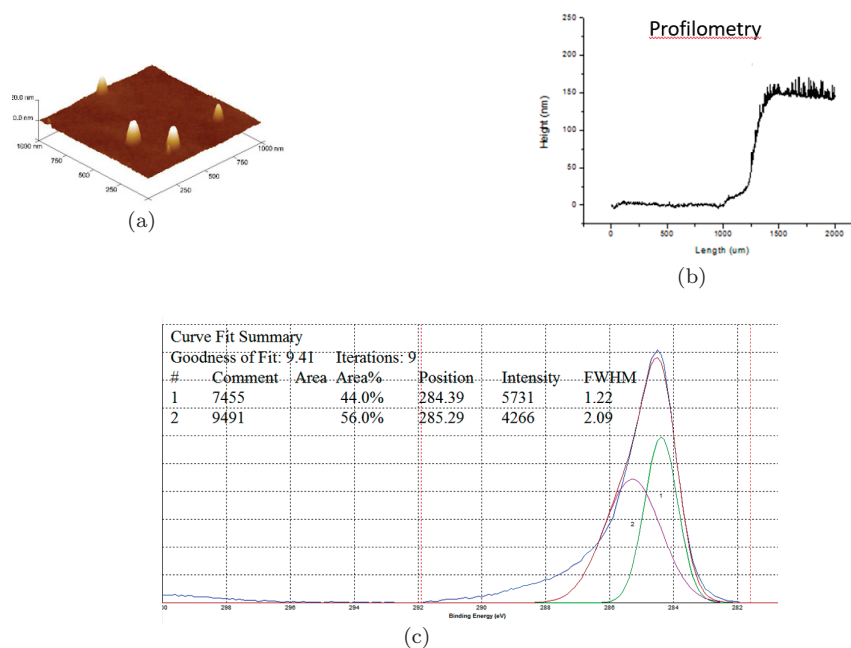

FIGURE A.14: Several different surface analysis work are included in this figure. Figure (a) is the result from an AFM test to define the level of smoothness of the film. Figure (b) is the result from the Profilometry test to identify the thickness of the coating film. Figure (c) is the spectrum analysis from an XPS test to give a roughly estimation of the sp^3 ratio in the carbon film.

Different measurement can be done on these witness strips after the deposition and help us understand the property of the film. Figure A.14 shows some results from surface analysis. Figure A.14 (a) is the AFM analysis we did to check how smooth our DLC film is. As this graph shows, there are some small bumps, but most of the surface is smooth at nm scale. Figure A.14 (b) shows the result of a profilometry test. This is used to measure the thickness of the film. The step shown in this graph is actually the step shown in figure A.13 (b). Because only part of the witness strip has been coated, so as long as we check the region contain the step, we can get the thickness of the coated film directly. Figure A.14 (c) shows an XPS analysis result. This test should tell us how much sp^3 structure is in the carbon film compared to the sp^2 structure. The spectrum has been re-analyzed and fit with two Gaussian curves centered around 285 eV and 284 eV. The Gaussian

curve centered around 285 eV represents the sp^3 bond, the other Gaussian curve centered at 284 eV represents the sp^2 bond. By comparing the area of these two curves, we can extract the sp^3/sp^2 ratio from this PLD run. The figure A.14 (c) specifically shows that around 56% of sp^3 has been generated during the coating.

A.4   Electron Beam Feposition For ^{58}Ni Coating

As explained before, ^{58}Ni is also a good candidate as the material for UCN transportation. The only reason we are not using it for most areas of our experiment is the depolarization property it has. But we actually don't care about the polarization status at the source region. So use guides coated by ^{58}Ni in our source region.

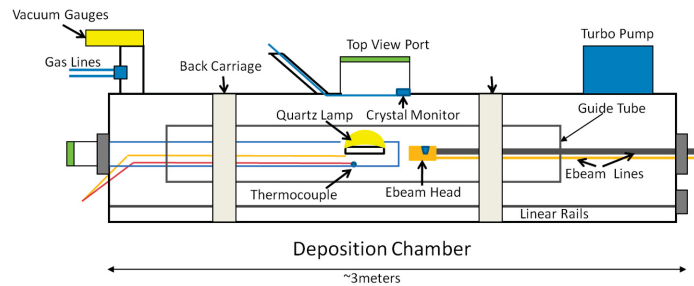FIGURE A.15: Diagram of EBeam coating structure[25].

The ^{58}Ni coating is mostly done in the same chamber as introduced before. But during this coating, we use electron beam instead of laser to evaporate the ^{58}Ni and have it condense onto the surface we need it to be. Figure A.15 shows the structure of EBeam coating system.

FIGURE A.16: Photograph of the quartz lamp installed during EBeam coating[25].

A quartz lamp takes the place where the carbon target was located. Figure A.16 shows the how the quartz lamp looks. This quartz lamp emits wavelengths from the ultraviolet

(UV) range to the near-infrared (NIR) ($\sim$ 240 nm to $\sim$ 2700 nm) with the majority of the light in the visible to NIR range. It is specifically used to heat the surface during the coating to pre-evaporate any contamination of water molecules. The head of the EBeam gun is actually in front of the center tube pre-installed in the chamber. A Crystal Monitor is mounted around top of the head of the EBeam gun. It is used to estimate the current evaporation rate from the crucible containing ^{58}Ni.
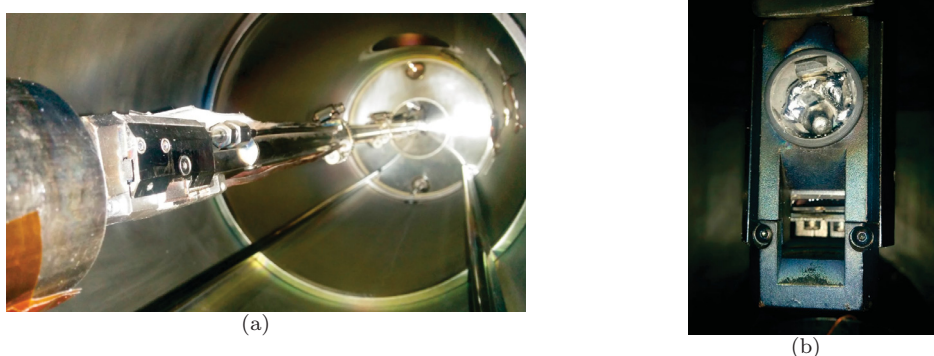

(a)

(b)

FIGURE A.17: Picture (a) is taken to show how the EBeam gun is mounted in the center of the coating chamber. Picture (b) shows the exact shape of the head of EBeam gun with crucible and Ni pills.

Figure A.17 shows how the EBeam gun is mounted in the chamber and how the head of EBeam gun looks with its crucible and ^{58}Ni pills.
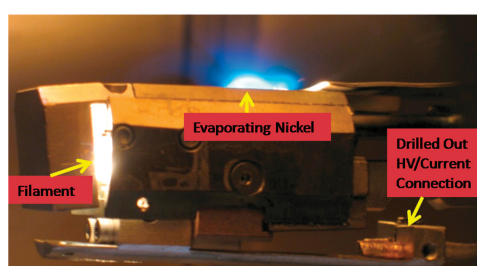

FIGURE A.18: Photograph of the ebeam head, during use, of the tube coating chamber ebeam. The faint blue arc is the magnetically guided electron beam emitted by the filament. Here the vapor density of the evaporating nickel is so high that one can see the photo emission of the nickel atoms via electron recombination or excitation.

Figure A.18 shows a picture from an actual deposition process. The electron beam is generated from the filament in the head and guided by the magnets pre-installed on the head so it can hit and evaporate ^{58}Ni in the crucible.

<div align="center">(a)</div>

<div align="center">(b)</div>

FIGURE A.19: These two pictures were taken 2016. These are components coated with ^{58}Ni and used for the new generation UCN source.

Figure A.19 is some examples of the guide component we coated during 2016 for the new generation of UCN source.

A.5 Summary of Guide Coating at Virginia Tech

In previous sections, we already introduce the importance of guide in UCNs related research and the apparatus at Virginia Tech which can be used for effectively coating the guide good for UCNs transportation. In this section, we summarize all the work we have done in past 6 years and briefly discuss possible improvement of this project in the future.

In the past 6 years, a new set of decay trap guides coated by DLC were made and installed in 2014. Decay trap guides are mainly used by UCNA and UCNB projection in the final detection area. A new set of squared guide was also made around same time. It was constructed by four copper plate with DLC coated and it was mainly used to transport UCNs from AFP to the decay trap. It was also implemented around 2014. Several quartz guides coated by DLC were made around 2014 and 2015. They were backup guides for the AFP running by UCNA, UCNB and UCN-tau. In 2016, the EBeam system was assembled again for ^{58}Ni coating purposes. All the parts need to be assembled as the new version UCN source were coated during this time and the source were installed during the fall of 2016. Although there were many unexpected issues we had to deal with, most guides needed to be done were delivered fortunately.

DLC and ^{58}Ni coated guides have been used for UCNs transportation for many years. However, some new materials start showing better performance and relative coating system might be worth developing. NiP is one of these new materials and already tested by

UCNs group works at LANL. It has high Fermi potential ($\sim$213 neV)[76] and low spin-flip probability ($3.3^{+1.8}_{-5.6} \times 10^{-6}$ per bounce)[77]. Since this material is more stable than DLC films, it should be a good replacement for the DLC guide in the future.